



universität
wien

MASTERARBEIT / MASTER'S THESIS

Titel der Masterarbeit / Title of the Master's Thesis

„Reconstruction of a 3.5-billion-year-old marine environment: Evidence from trace element systematics of the iron formation exposed in the Daitari Greenstone Belt, Singhbhum Craton, India“

verfasst von / submitted by

Sandra Kienle BSc

angestrebter akademischer Grad / in partial fulfilment of the requirements for the degree of
Master of Science (MSc)

Wien, 2024 / Vienna 2024

Studienkennzahl lt. Studienblatt /
degree programme code as it appears on
the student record sheet:

A 066 815

Studienrichtung lt. Studienblatt /
degree programme as it appears on
the student record sheet:

Masterstudium Erdwissenschaften

Betreut von / Supervisor:

Univ.-Prof. Dr. Christian Köberl

Mitbetreut von / Co-Supervisor:

Dr. Sebastian Viehmann

Table of Contents

Abstract	3
Zusammenfassung	4
Acknowledgments	5
List of Figures	6
List of Tables	8
1 Introduction	9
1.1 Evolution of the atmosphere and hydrosphere on Earth through time	9
1.2 Banded Iron Formations (BIFs)	11
1.2.1 Characterization, mineralogy, and worldwide distribution	11
1.2.2 Depositional settings and theories of Fe(II)-oxidation	14
1.3 Geochemistry of Rare Earths and Yttrium (REY)	16
1.3.1 Geochemical behavior of REY	16
1.3.2 REY in Seawater	19
1.3.3 REY geochemistry of marine chemical sediments	23
1.4 Objective of this thesis and geological significance	24
2 Geological Setting	25
2.1 Geology of the Singhbhum Craton	25
2.2 The Daitari Greenstone Belt	28
2.2.1 Geology of the Daitari Greenstone Belt	28
2.2.2 BIFs preserved in the Tomka Formation	29
3 Samples and analytical methods	30
3.1 Samples and preparation	30
3.2 ICP-MS analysis	31
4 Results	32
4.1 Normalization of REY and calculation of REY _{SN} anomalies	32
4.2 Rare earth elements and other trace elements	32

4.3	Data quality	38
5	Discussion	41
5.1	The reliability of the Tomka BIF as geochemical archive for Paleoproterozoic seawater 41	
5.2	The depositional environment of the Tomka BIF	46
5.3	Europium anomalies of Tomka BIF.....	50
5.3.1	Europium evolution curve as a qualitative dating tool	50
5.3.2	Explanations for Eu_{CN} systematics of Tomka BIF	51
5.3.3	The link of Eu_{CN} anomalies in BIFs to the geodynamic evolution of the early Earth ...	53
6	Conclusions	55
	References	57
	Appendix	67

Abstract

Iron- and chert-rich layers of the ~3.5 Ga old Banded Iron Formation (BIF) preserved within the Tomka Formation in the Daitari Greenstone Belt (Singhbhum Craton, India) serve as excellent geochemical archives for the composition of Paleoproterozoic seawater and provide a unique potential to reconstruct ancient marine environments.

Trace element compositions of high pressure-high temperature digestions of individual chert-, Fe- and mixed Fe- and chert-microbands were determined via quadrupole ICP-MS. The samples show very low concentrations of incompatible elements such as Al, Hf, Th, and Zr that are typically associated with detrital aluminosilicates. The Tomka BIF samples also show typical shale-normalized (subscript SN) rare earth element and yttrium REY_{SN} patterns of Archean seawater and with the exception of redox-sensitive Ce and Eu also to modern seawater, i.e., enrichment of heavy to light REY_{SN} (Yb_{SN}/Pr_{SN}: 2.67-20.4), positive La_{SN} (La_{SN}/La*_{SN}: 1.43-3.43) and Gd_{SN} (Gd_{SN}/Gd*_{SN}: 1.12-1.64) anomalies as well as super-chondritic Y/Ho ratios (41.2-66.7). The presence of positive Eu_{SN} (Eu_{SN}/Eu*_{SN}: 1.37-3.17) anomalies indicate REY contributions from high-temperature hydrothermal fluids in seawater of the Tomka depositional environment. The lack of negative Ce_{SN} (Ce_{SN}/Ce*_{SN}: 0.67-1.37) anomalies suggests anoxic atmospheric-hydrospheric conditions during BIF deposition.

Compiled chondrite-normalized (subscript CN) Eu_{CN} data of pure Archean BIFs show that Eu_{CN}/Eu*_{CN} ratios of Precambrian seawater follow a general global evolution curve with BIFs displaying strong positive Eu_{CN} anomalies in the Eoarchean, followed by decreasing Eu_{CN}/Eu*_{CN} ratios until the Neoproterozoic. Eu_{CN} data from seawater archives in the time frame around 3.5 Ga, however, are lacking to date. Eu_{CN}/Eu*_{CN} ratios of the Tomka BIF that fall into this time window do not follow the estimated global seawater Eu_{CN} curve but show significantly lower Eu_{CN}/Eu*_{CN} values. These values may indicate a less pronounced flux of high-temperature hydrothermal REY to the Archean Ocean or at least into the Tomka depositional environment ca. 3.5 Ga ago. The Eu_{CN} systematics might be also linked to upper mantle temperatures and the geodynamic evolution of early Earth with stagnant lid tectonics as a possible prevailing tectonic regime.

Zusammenfassung

Die Tomka Formation im Daitari Grünsteingürtel (Singhbhum Kraton, Indien) enthält eine etwa 3,5 Milliarden Jahre alte gebänderte Eisenformation (BIF), welche sich als exzellentes geochemisches Archiv für die Zusammensetzung von präkambrischem Meerwasser erweist.

Die Spurenelementzusammensetzung wurde mittels Quadrupol-Massenspektrometer ermittelt und bei der Interpretation der Ergebnisse lag ein besonderer Fokus auf den Metallen der Seltenen Erden. Die individuellen Chert-, Fe- und gemischte Lagen der Tomka BIF weisen eine sehr hohe Reinheit auf, d.h. sehr geringe Konzentrationen an inkompatiblen Elementen wie Al, Hf, Th und Zr auf, welche typischerweise mit detritalen Aluminosilikaten assoziiert sind. Des Weiteren zeigen die Proben auch das typische Muster der Seltenerdelemente und Yttrium (REY, rare earth elements and yttrium) von archaischem Meerwasser und Tonstein-normierten (Index SN) REY-Muster, die modernem Meerwasser bis auf redox-sensitive Elemente wie Ce und Eu sehr ähnlich sind. Es zeigt sich eine Anreicherung von schweren zu leichten REY_{SN} (Yb_{SN}/Pr_{SN} : 2,67–20,4), positive La_{SN} (La_{SN}/La^*_{SN} : 1,43–3,43) und Gd_{SN} (Gd_{SN}/Gd^*_{SN} : 1,12–1,64) Anomalien und super-chondritische Y/Ho-Verhältnisse (41,2–66,7). Das Vorhandensein positiver Eu_{SN}-Anomalien (Eu_{SN}/Eu^*_{SN} : 1,37–3,17) weist auf den Einfluss von hydrothermalen hochtemperierten Fluiden im Meerwasser des Ablagerungsumfeldes der Tomka BIF hin. Das Fehlen negativer Ce_{SN}-Anomalien (Ce_{SN}/Ce^*_{SN} : 0,67–1,37) deutet auf anoxische Bedingungen während der BIF-Ablagerung hin.

Eine Zusammenstellung von Chondrit-normierten (Index CN) Eu_{CN}/Eu^{*}_{CN}-Verhältnissen reiner präkambrischer BIFs zeigt eine globale Entwicklungskurve von Meerwasser, welche im Eoarchaikum stark positive Eu_{CN}-Anomalien aufweisen, gefolgt von abnehmenden Eu_{CN}/Eu^{*}_{CN}-Verhältnissen bis ins Neoarchaikum. Allerdings fehlten bisher Eu_{CN}-Daten in der Zeitspanne um 3,5 Ga. Die Eu_{CN}/Eu^{*}_{CN}-Verhältnisse der Tomka Formation, welche in dieses Zeitfenster fallen, folgen nicht der globalen Meerwasser-Eu_{CN}-Kurve, sondern zeigen deutlich niedrigere Eu_{CN}/Eu^{*}_{CN}-Werte. Diese Werte deuten möglicherweise auf einen weniger ausgeprägten Eintrag von hydrothermale hochtemperierten REY in den Archaischen Ozean oder zumindest in das Tomka Ablagerungsmilieu vor etwa 3,5 Ga hin. Die Eu_{CN}-Systematik könnte auch mit der Geotektonik der frühen Erde in Zusammenhang stehen, wobei die „stagnant lid“ Tektonik ein möglicher vorherrschender Zustand gewesen sein könnte.

Acknowledgments

I would like to thank everyone who has supported me during the process of my master's thesis and all those who have contributed to it.

I would like to thank my supervisors Univ.-Prof. Dr. Christian Koeberl and Dr. Sebastian Viehmann, whose continuous support has been essential in the completion of this thesis, and I am thankful for the opportunity to work in this field.

I would especially like to thank Dr. Sebastian Viehmann for his tireless and continuous support throughout the entire process. My thesis would not have been possible without his endless help and his eagerly shared knowledge.

Furthermore, I would like to thank Jaganmoy Jodder (University of Oslo) for supplying the samples and sharing his expertise.

Lastly, I would like to express my thanks to my family and friends, whose constant support encouraged and motivated me during the whole writing process.

List of Figures

Figure 1: The evolution of the oxygen concentration in the atmosphere and the oceans from the Archean to present.....	10
Figure 2: Simplified model of Algoma-type and Superior-type BIF sedimentary deposits ...	12
Figure 3: Global map showing the approximate locations of major BIFs, with deposit size and time of deposition indicated	13
Figure 4: Representative (A) Algoma-type BIF, (B, C) Superior-type BIF and (C) NIF samples	14
Figure 5: REE radii of the M^{3+} ions	18
Figure 6: Comparison of a BIF sample with unnormalized REY content and a BIF sample with PAAS (Post Archean Australian Shale) normalized REY content	19
Figure 7: Comparison of shale-normalized REY abundances of modern shallow and deep seawater from the Atlantic and Pacific Oceans.....	21
Figure 8: Geological map of the Singhbhum Craton focusing on the Archean and Proterozoic geology	26
Figure 9: Stratigraphy of the Archean geology of the Singhbhum Craton	27
Figure 10: Stratigraphic log of the volcano-sedimentary succession of the Daitari greenstone belt.....	29
Figure 11: Graph of Zr vs. Nd concentrations of the Tomka chert-, Fe- and mixed BIF bands, and the shale sample DM71A	36
Figure 12: Representative REY_{SN} patterns of Tomka BIF chert-, Fe- and mixed bands and shale sample DM71A	37
Figure 13: Graph of La_{SN}/La^*_{SN} ratio vs Gd_{SN}/Gd^*_{SN} ratio of Tomka BIF chert-, Fe- and mixed bands as well as the shale DM71A.....	38
Figure 14: Graph of Y/Ho ratio vs. Zr concentration of Meso- and Paleoarchean BIFs	43
Figure 15: Graph of La_{SN}/La^*_{SN} ratio vs Gd_{SN}/Gd^*_{SN} ratio of Tomka BIF samples compared to samples of Witwatersrand BIF, Pietersburg BIF, and Moodies Group BIF	44
Figure 16: Graph of Y/Ho ratio vs. Yb_{SN}/Pr_{SN} ratio of Tomka BIF samples compared to samples of Witwatersrand BIF, Pietersburg BIF, and Moodies Group BIF	45
Figure 17: The REY_{SN} patterns of the eight best preserved (i.e., pure) Tomka BIF samples compared to modern seawater.....	46
Figure 18: REY_{SN} patterns of a representative Tomka BIF samples compared to representative pure BIF samples from the Eoarchean Isua Greenstone Belt, the Mesoarchean	

Pietersburg Greenstone Belt, the Neoproterozoic Temagami Greenstone Belt, the Paleoproterozoic, the Neoproterozoic Urucum BIF, and modern seawater.....	47
Figure 19: Comparison of the REY _{SN} patterns of a Tomka BIF sample and a high-temperature hydrothermal fluid, the alkaline Lake Van in Turkey, a hypersaline brine, river water from Markarfljót River and water from Lake Paranoá in Brasil.	48
Figure 20: The Precambrian Eu _{CN} /Eu* _{CN} evolution curve of pure BIFs (i.e., reliable seawater archives)	51
Figure 21: Time chart of early magmatic, depositional, and structural events in the Singhbhum Craton with focus on the Badampahar Group including the Tomka BIF	53
Figure 22: Schematic evolution of plate tectonics and the lithosphere	54
Figure A1: Samples of Tomka BIF (DM17C, DM17D, DM17E and DM22B)	69
Figure A2: Samples of Tomka BIF (DM22C, DM22D, DM76A and DM90)	70
Figure A3: Samples of Tomka BIF (IND-DGB-Bif2-1 and IND-DGB-Bif2).....	71

List of Tables

Table 1: Compilation of the rare earth elements including yttrium with ionic radii given in eight-fold coordination	17
Table 2: Listing of the individual Tomka BIF sample layers with information on GPS locality	31
Table 3: Trace element concentrations (in ppm) of Tomka BIF and shale sample	33
Table 4: Values of analyzed IFG concentrations (ppm) and published IFG values.....	40
Table A1: Trace element concentrations (in ppm) of Tomka BIF samples, shale sample DM71, and BIF reference material	72

1 Introduction

1.1 Evolution of the atmosphere and hydrosphere on Earth through time

For over half a century, research was done on the evolution of the atmosphere-hydrosphere systems through Earth's history to not only resolve the origins of life but also to improve knowledge about Earth's geological past to tackle the increasing threat of the climate change.

The Hadean started ~4.5 billion years (Ga) ago with the formation of the Earth and ended at 4.0 Ga which roughly coincides with the age of the oldest rocks dated (Bowring & Williams, 1999). This first period in Earth's history is characterized by a lack of a geological rock record and the understanding of pre-Archean continental crust is largely based on Hadean detrital zircons (e.g., Wilde et al., 2001; Watson & Harrison, 2005; Hopkins et al., 2008; Turner et al., 2020). Zircon minerals from the Jack Hills, Australia, have been studied intensely and oxygen isotopic compositions as a geochemical proxy reveal the presence of liquid water on or near Earth's surface already in the Hadean (e.g., Mojzsis et al., 2001; Wilde et al., 2001; Valley et al., 2002). The origin of water, and how it accumulated on Earth's surface is still debated, primarily due to the lack of a rock record. There exist numerous hypotheses on the initial source of water on Earth with some researchers favoring the theory that liquid water was already present during Earth's accretion (e.g., Zolensky, 2005), while others consider extraterrestrial sources responsible for liquid water on Earth (Lowenstein et al., 2014, and references therein).

Holland (2006) divided the last 3.85 Ga of Earth's history into five stages, with the boundaries defined by the time of significant changes in the redox state of the Earth. The first period starts 3.85 Ga ago in the Eoarchean, with the first geological evidence for liquid water found in pillow lavas and sediments from the Isua Greenstone Belt, West Greenland (Nutman et al., 1984; Rosing, 1999). Archean oceans were almost certainly anoxic (but not euxinic) and supposed to be ferruginous (i.e., rich in dissolved iron and poor in sulphate) throughout the Archean (Fig. 1) which may be indicated by the wide occurrence of Banded Iron Formations (BIFs). However, there are possible exceptions of small, oxygenated water masses in shallow ocean areas. The Archean atmosphere was largely anoxic as well and O₂ levels were significantly lower than the 10⁻⁵ present atmospheric level (PAL, e.g., Kasting et al., 2001; Pavlov & Kasting, 2002). The anoxic state of Archean oceans and atmosphere can be validated by large degrees of mass-independent fractionation (MIF) of sulphur isotopes in sulphide minerals (e.g., pyrite, Farquhar et al., 2000). This MIF signal is preserved until 2.45 Ga (e.g., Pavlov & Kasting, 2002; Bekker et al., 2004), which also marks the end of this first stage and roughly the end of the Archean.

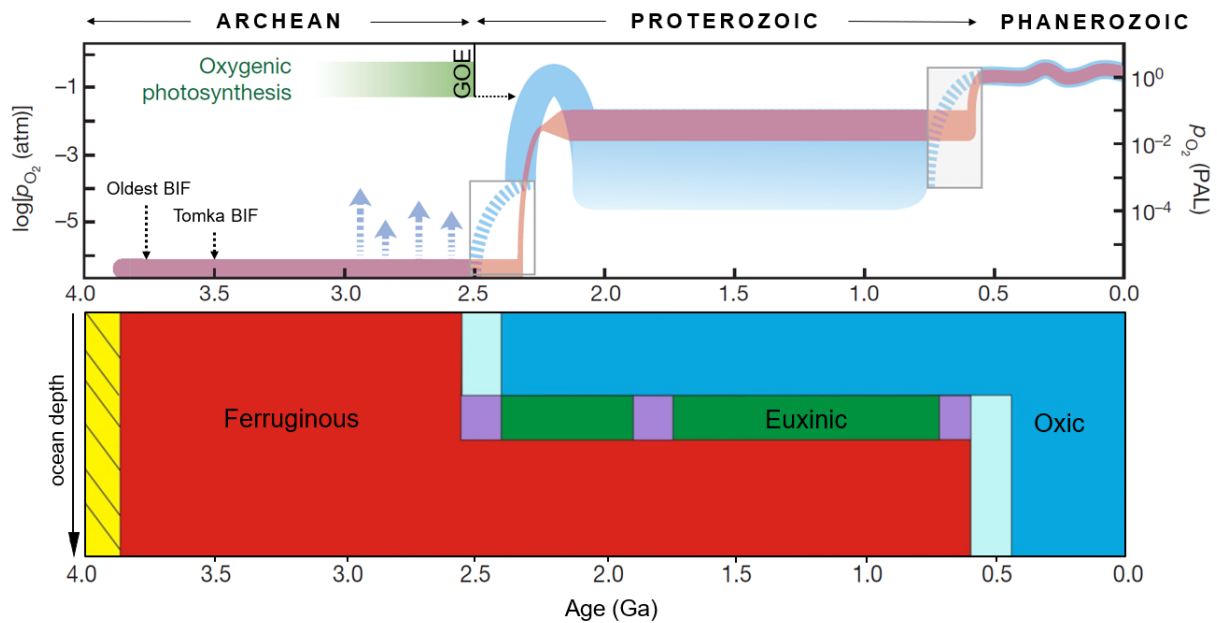


Figure 1: The evolution of the oxygen concentration in the atmosphere (top, modified from Lyons et al., 2014) and the oceans (modified from Lowenstein et al., 2014) from the Archean to present.

During stage 2 (2.45 – 1.85 Ga), including the Early and Middle Paleoproterozoic, atmospheric O_2 levels began to rise significantly and continuously, which can almost certainly be explained by the evolution of photosynthesizing cyanobacteria (Blankenship & Hartman, 1998). This short period in the early Proterozoic between ~2.45 and 2.3 Ga (Lyons et al., 2014) is known as the Great Oxygenation Event (GOE, Holland, 2002) and evidence of this, such as rusty red soil, is found in the rock record. However, the presence of O_2 -synthesizing cyanobacteria has been already reported around 2.7 Ga (Brocks et al., 2003; Summons et al., 1999) and there is evidence that early “whiffs” of oxygen resulted in local oxygen oases that have been reported as far back as 2.95 Ga (Anbar et al., 2007; Bau & Alexander, 2009; Frei et al., 2009; Kendall et al., 2010; Crowe et al., 2013).

Stage 3 (1.85-0.85 Ga) is constrained from the Middle Paleoproterozoic to Early Neoproterozoic, where atmospheric oxygen levels did not change significantly but were lower than present atmospheric conditions. BIFs disappeared completely from the rock record during this period of one billion years. The oceans were oxygenated in the shallower parts, but deeper water masses were still anoxic and ferruginous; some parts, for example, restricted basins, of the ocean even became euxinic (e.g., Holland, 2006; Lyons et al., 2014).

Stage 4 (0.85-0.54 Ga) covers the Early Neoproterozoic until the Late Neoproterozoic and began with another rise of atmospheric oxygen followed by extensive oxygenation of the oceans. This period is characterized by three great major glaciations that led to “Snowball

Earth” conditions and Banded Iron Formations re-appear a last time in the rock record associated with glacial deposits (Kirschvink, 1992; Hoffman et al., 1998). The rise of atmospheric oxygen resulted in the evolution of more complex animals (Ediacaran fauna) and first occurrence of macroscopic, multi-cellular trace fossils (metazoans) in the rock record (e.g., Bengtson & Yue, 1992; Waggoner, 1998).

Stage 5, the Phanerozoic Eon, began 541 million years ago continuing to the present day and is characterized by significant changes in Earth’s atmosphere and hydrosphere. This period yields, in contrast to the Precambrian, a vast rock record leading to a comparably detailed knowledge of this time. The global seawater chemistry witnessed drastic changes as a result of sea level fluctuations, climate changes, changing rates of erosion and weathering of continents and the evolution of marine life which evolved into more complex forms. The level of atmospheric oxygen has also varied significantly over the Phanerozoic, which is largely driven by biotic factors but also by abiotic mechanisms (e.g., Logan et al., 1995; Lyons et al., 2014). O₂ levels peaked during the Permo-Carboniferous (Berner, 2004) due to massive growth of vascular land plants that even triggered the development of giant insects and other arthropod groups (e.g., Graham et al., 1995; Dudley, 1998). This followed a period of a massive decline of the O₂ level reaching a minimum in the early Jurassic until it reached the present value.

1.2 Banded Iron Formations (BIFs)

1.2.1 Characterization, mineralogy, and worldwide distribution

Banded Iron Formations (BIFs) are chemical sediments deposited in marine environments and typically composed of thin-bedded or laminated rocks with commonly alternating Fe-rich and Si-rich layers. These iron formations are globally distributed, and its formation is confined to the Precambrian (e.g., James, 1954; Gross, 1980; Bekker et al., 2013).

BIFs are defined by their unique mineralogy which includes a wide range of Fe-rich and Al-poor minerals (mostly magnetite and hematite) and cryptocrystalline quartz (chert), carbonates and, less commonly, sulfides (e.g., Bekker et al., 2013; Konhauser et al., 2017). Aluminous minerals in iron formations usually indicate contamination with volcanoclastic or siliciclastic detritus (e.g., Pickard, 2003). Based on the mineralogical composition and different bulk compositions, James (1945) defined four facies to classify BIFs: silicate-, carbonate-, oxide- and sulfide-iron-formations. However, a classification that is more widely used in literature is based on the interpreted depositional setting where BIFs are divided into Algoma- and Superior-

type BIFs (Fig. 2, after Gross, 1965). However, these two classifications might be also considered as endmembers with a range of intermediate varieties.

BIFs older than 3.0 Ga appear to be largely of the Algoma-type and typically occur worldwide in volcano-sedimentary sequences of greenstone belts ranging in age from the Eoarchean to the late Paleoproterozoic (e.g., Goodwin, 1973; James, 1983; Huston & Logan, 2004; Isley & Abbott, 1999). The oldest iron formations are found in the Isua Greenstone Belt (3.7-3.8 Ga) in Greenland (e.g., Nutman et al., 1997) and in the Nuvvuagittuq Belt (> 3.8 Ga) in Canada (e.g., O’Neil et al., 2012; Cates et al., 2013). The deposited volume of Algoma-type BIFs is generally rather small, with lateral extends of less than 10 km and thicknesses of 10-100 m (Gross, 1965; Goodwin, 1973; Appel, 1980; Isley & Abbott, 1999). The depositional setting is suggested to be intracratonic rift zones and island arc/back arc basins (Gross, 1983; Veizer, 1983) and the formation is connected to exhalative-hydrothermal processes close to volcanic centers (e.g., Huston & Logan, 2004; Bekker et al., 2010).

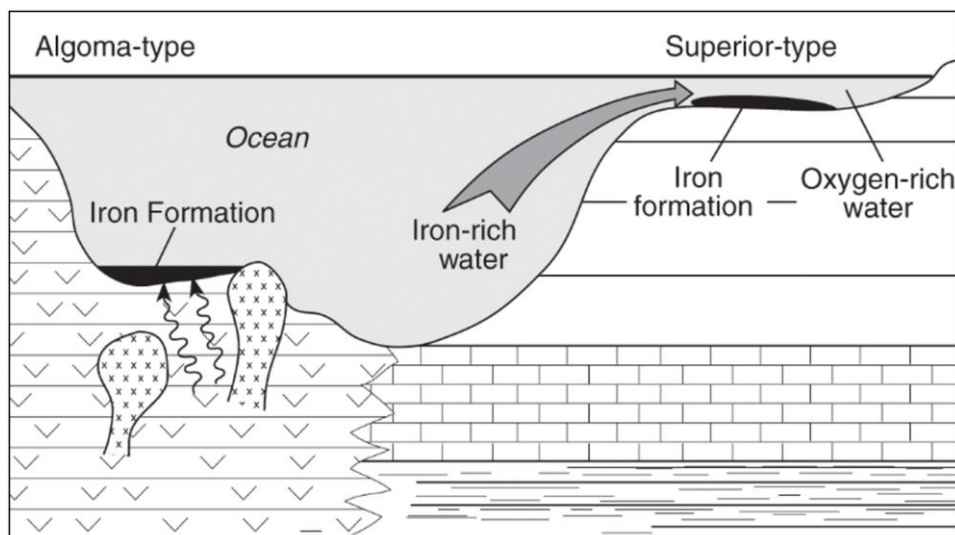


Figure 2: Simplified model of Algoma-type and Superior-type BIF sedimentary deposits (modified from Kesler & Simon, 2015).

Superior-type BIFs mainly have been formed during the Paleoproterozoic on nearshore continental-shelf environments and were presumably deposited during periods of sea transgression generally associated with sedimentary basins and cratonic margins (e.g., Trendall, 1968; Bekker et al., 2013; Aftabi et al., 2021). In contrast to the Algoma-type, Superior-type BIFs are laterally more extensive with prominent representatives in the Transvaal Supergroup (South Africa) and the Hamersley Group (Western Australia), showing lateral extends of over 10^5 m² and thicknesses of several hundred meters (e.g., Klein & Beukes, 1992; Arndt et al., 1991; Pickard, 2003).

After a one-billion-year hiatus BIFs reemerged in the Neoproterozoic and showed the last significant occurrence of iron formations worldwide in the stratigraphic record. The deposition of these Neoproterozoic Iron Formations (NIFs) is presumably linked to extreme climate conditions that led to a widespread glaciation which resulted in a ‘Snowball Earth’ period (Kirschvink, 1992; Hoffman et al., 1998; Isley & Abbott, 1999; Cox et al., 2013). Unlike the extensively documented Archean and Paleoproterozoic BIFs, banding is generally poorly developed or entirely absent. NIFs are often associated with glaciogenic sediment structures as for instance observed in the Rapitan Iron Formation (northern Canada), which is interbedded with tillites and contains occasional dropstones (Kirschvink, 1992; Cox et al., 2013).

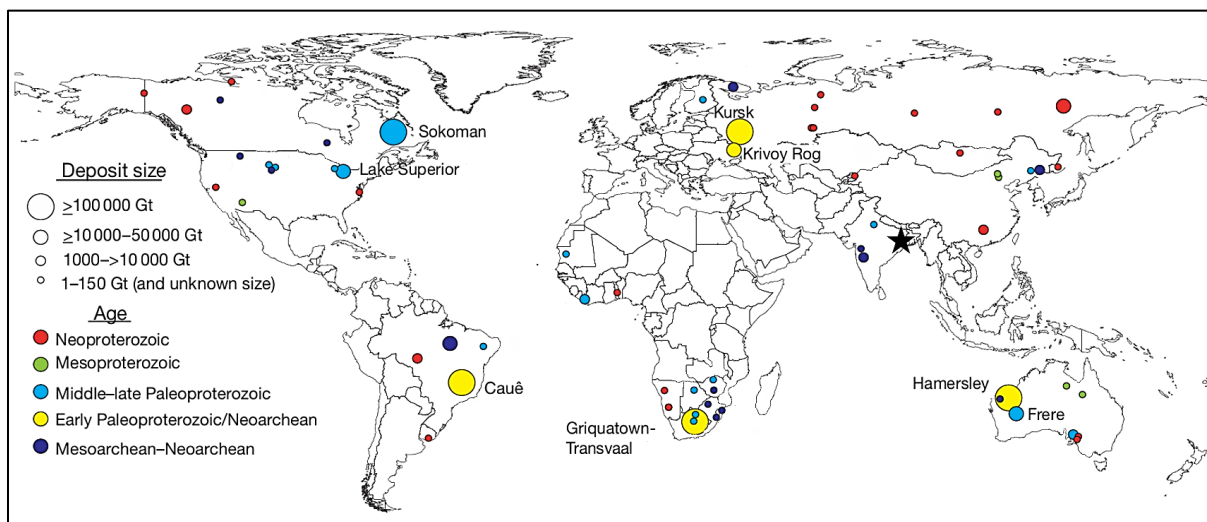


Figure 3: Global map showing the approximate locations of major BIFs, with deposit size and time of deposition indicated. The black star marks the location of the Paleoproterozoic Tomka BIF, which is in the focus of this thesis (modified from Bekker et al., 2014).

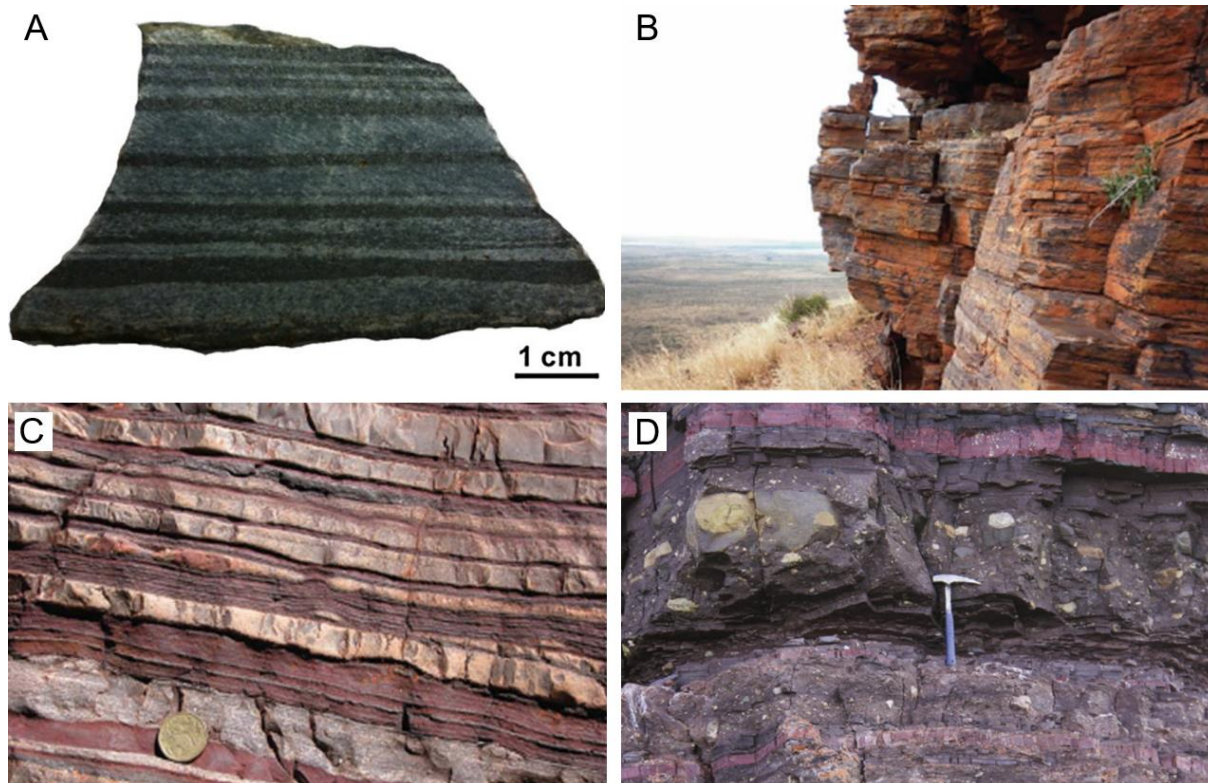


Figure 4: Representative (A) Algoma-type BIF, (B, C) Superior-type BIF and (D) NIF samples.

BIF samples show the typical alternation of Fe-rich and chert layers, e.g., from the (A) the Eoarchean, ca. 3.7 Ga old Isua Greenstone Belt (Greenland, Sun & Li, 2016), (B) the Early Paleoproterozoic, ca 2.47 Ga Kuruman Formation (South Africa, Konhauser et al., 2017), (C) the Early Paleoproterozoic, ca 2.46 Ga Hamersley Group (West Australia, Konhauser et al., 2017) and from the Neoproterozoic Rapitan Iron Formation (Canada, Cox et al., 2013).

1.2.2 Depositional settings and theories of Fe(II)-oxidation

Banded Iron Formations have been studied for many decades due to economic interests as they represent by far the most important iron ore deposits being mined all over the world (e.g., Simonson, 2003). On the other hand, as chemical sediments they also provide valuable insights into the composition of ancient seawater and the evolution of the hydrosphere-atmosphere-lithosphere system (e.g., Bau & Dulski, 1996b). However, the mechanisms of BIF deposition and the source of iron is still controversial and has not yet been finally clarified, also related to the lack of modern analogues.

It has been suggested that iron and other chemical constituents of Precambrian oceans have been supplied by continental sources through rivers and dust (e.g., Miller & O’Nions, 1995; Alexander et al., 2008). However, there is significant evidence that submarine hydrothermal systems are the dominant source of iron in Precambrian seawater, where reduced Fe species may have been transported from the deep ocean by upwelling currents from mid-ocean ridge systems to outer continental shelves. Moreover, all types of iron formations show geochemical

signatures of hydrothermal sources (e.g. Jacobsen & Pimentel-Klose, 1988; Klein & Beukes, 1992; Krapež et al., 2003; Simonson, 2003; Posth et al., 2011). Furthermore, Isley and Abbot (1999) suggested a direct link between mantle plume activity between 3.8 and 1.8 Ga and global deposition of large, economically important BIFs.

It is commonly accepted that the source of iron for BIF deposits is Fe^{2+} that was subsequently altered to Fe^{3+} -(oxyhydr)oxides, which indicates that some kind of oxidizing mechanism was present. Dissolved Fe^{2+} easily oxidizes in the presence of oxygen at neutral pH; however, there must be an anoxic oxidizing mechanism to explain the formation of the vast Archean deposits prior to the rise of oxygen in the atmosphere (e.g., Posth et al., 2011; Bekker et al., 2013; Konhauser et al., 2017).

Both biotic and abiotic models of BIF depositions have been suggested; Cloud (1968) first described a model where cyanobacteria play an important role in iron precipitations which quickly gained wide acceptance. Still, the specific mechanisms of BIF deposition including the oxidation mechanisms of Fe^{2+} remain poorly understood, but the most widely supported models in literature are briefly described below.

Prior to the rise of oxygen in the atmosphere and the development of a protective ozone layer, the Earth's surface was exposed to high levels of ultraviolet (UV) radiation. This led to a BIF depositional model in which this high flux of UV radiation drives an abiotic mechanism of Fe^{2+} oxidation and the precipitation of Fe(oxyhydr)oxides at circumneutral pH as dissolved ferrous iron species can absorb radiation in the 200-400 nm range (Braterman et al., 1983; Cairns-Smith, 1978). However, UV photo-oxidation may have been relatively insignificant, except for iron-rich marine environments with very shallow depths, and not the dominant mechanism for BIF deposition in the Archean (Konhauser et al., 2007).

The classic model for abiotic BIF deposition was first postulated by Cloud (1968), in which upwelling reduced iron-rich waters reached oxygenated shallow waters leading to the precipitation of Fe(oxyhydr)oxides. Under anoxic conditions in the Archean, this O_2 could have been confined to local "oxygen oases" associated with cyanobacterial blooms (Cloud, 1968) where O_2 is assumed to have been produced by planktonic oxygenic photosynthesizers like cyanobacteria. They are considered to be the first primary producers utilizing oxygenic photosynthesis (e.g., Han & Runnegar, 1992; Knoll et al., 2006; Bekker et al., 2013), even though the first confirmed evidence of cyanobacteria occurs in the Neoproterozoic at 2.7 Ga (Summons et al., 1999).

A different model of BIF deposition was proposed by Garrels et al. (1973) and Hartman (1984), suggesting a form of anoxygenic photosynthesis where light, not oxygen, may have coupled the carbon and iron cycles with microbes using Fe^{+2} rather than H_2O as an electron donor and producing Fe^{+3} as metabolic waste instead of O_2 . Since then, studies have validated this theory with the discovery of Fe^{+2} -oxidizing bacteria (e.g., Widdel et al., 1993).

Furthermore, it is likely that BIFs formed in different ways in the Precambrian as the span of deposition was accompanied by many drastic atmospheric changes, going from an early anoxic atmosphere rich in CO_2 and CH_4 to an atmosphere with increasing oxygen content which consequently substantially influenced the seawater chemistry (e.g., Bekker & Kaufman, 2007; Lowenstein et al., 2014; Lyons et al., 2014).

1.3 Geochemistry of Rare Earths and Yttrium (REY)

1.3.1 Geochemical behavior of REY

The Rare Earth Elements (REEs) were first described by the Finnish chemist Johan Gadolin in 1794, who discovered them in a mineral he named “ytterbite”, which was later renamed to Gadolinite. The mineral comprised all the 15 REEs, but it was only after over 100 years that all the different REEs have been discovered due to the difficulty to separate them. REEs are not especially “rare” compared to many other metals in Earth’s crust like copper or tin, but they are never found in very high concentrations and exploitable deposits (e.g., Henderson, 1984).

The REEs are members of the group IIIa in the periodic table including the elements La to Lu (atomic number 57 to 71) and are commonly also described as “lanthanides” or “lanthanoids”. They display a similar (geo-)chemical behavior which arises from their electron configurations resulting in comparable ionic radii and charge (Tab.1). Most REEs typically exist in trivalent oxidation state in natural environments, which is the most stable form. However, redox-sensitive Ce and Eu can occur under specific redox or temperature conditions in tetravalent and divalent oxidation state, respectively (De Baar et al., 1985; Elderfield et al., 1988; Bau, 1996).

Table 1: Compilation of the rare earth elements including yttrium with ionic radii given in eight-fold coordination (after Shannon, 1976).

Element	Symbol	Atomic Number	Ionic Radius [Å]	
Lanthanum	La	57	1.160	
Cerium	Ce	58	1.143 (Ce ⁴⁺ 0.970)	LREY
Praesodymium	Pr	59	1.126	
Neodymium	Nd	60	1.109	
Promethium	Pm	61	-	
Samarium	Sm	62	1.079	
Europium	Eu	63	1.066 (Eu ²⁺ 1.250)	MREY
Gadolinium	Gd	64	1.053	
Terbium	Tb	65	1.040	
Dysprosium	Dy	66	1.027	
Yttrium	Y	39	1.019	
Holmium	Ho	67	1.015	
Erbium	Er	68	1.004	HREY
Thulium	Tm	69	0.994	
Ytterbium	Yb	70	0.985	
Lutetium	Lu	71	0.077	

The REEs exhibit a phenomenon, called “lanthanide contraction”, which describes the steady decrease in the size of the ion with increasing mass number. For each consecutive atom the nuclear charge is more positive by one unit, accompanied by a corresponding increase in the number of electrons present in the 4f orbital. This leads to increasing attraction between ionic core and shell and results in successive reduction of the ion size with increasing mass number (Fig. 5, Goldschmidt, 1925).

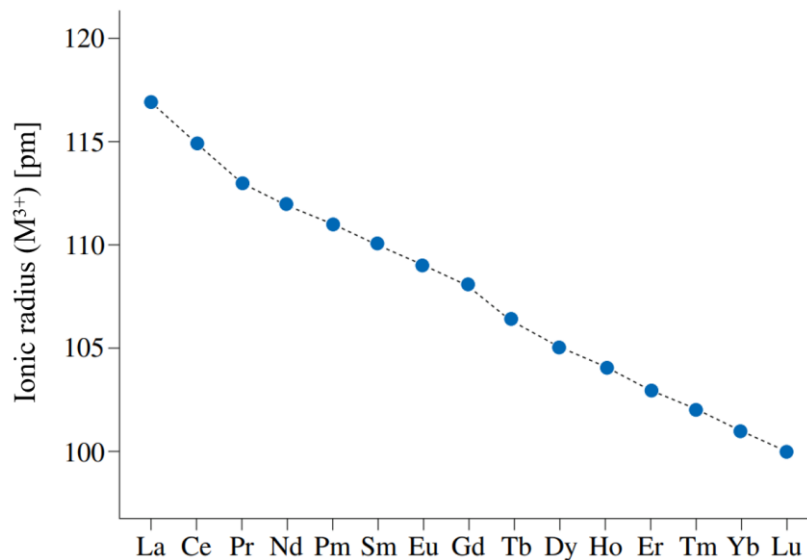


Figure 5: REE radii of the M³⁺ ions (Binnewies et al., 2016).

Yttrium is often included into the REE series and referred to as REE + Y (rare earth elements plus yttrium) or REY (rare earths and yttrium). This is due to the similarity of the atomic radii of Y and heavy REE (HREY, Ho-Lu) and places it between Dy and Ho in the REE series (Tab. 1). A common distinction between REY is made by atomic numbers; those with the lowest atomic numbers are referred to as the light REY (LREY, La-Nd), followed by middle REY (MREY, Sm-Dy) and heavy REY (HREY, Ho-Lu).

The unique chemical properties of the REY make them a very useful tool for tracing geological processes in magmatic, aqueous, or cosmochemical systems, radiometric dating, or geochemical modelling. Contents of REY are commonly represented in normalized form and leads to a flat REY pattern instead of a zigzag pattern (Fig. 6) allowing to overcome the Oddo-Harkins law (element with even atomic number are more abundant than the elements with immediately adjacent uneven atomic numbers). Normalization allows for more meaningful comparison between different samples and to calculate and visualize anomalies (e.g., Sholkovitz et al., 1989; Elderfield et al., 1990; De Baar et al., 1991; Sholkovitz et al., 1994).

Many reference materials that can be used for normalization of abundances exist and may be divided into two main types: chondrite meteorites (subscript CN, i.e., chondrite normalized), representing the REY abundance of the bulk silicate earth, and shales, representing the average composition of the upper continental crust. Shale normalization (subscript SN, i.e., shale normalized), for instance, is used to evaluate detrital components in seawater precipitates and the most common reference material is the “Post Archean Australian Shale” (PAAS), which was initially published by Nance and Taylor (1976) and later updated by Taylor & McLennan (1985) and McLennan (1989).

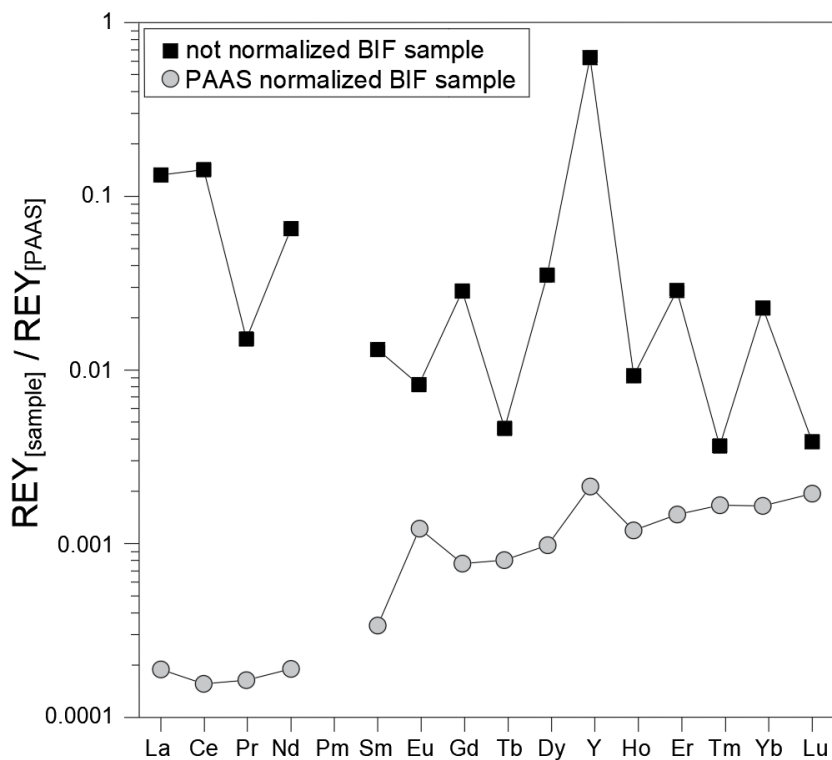


Figure 6: Comparison of a BIF sample with unnormalized REY content (black squares) and a BIF sample with PAAS (Post Archean Australian Shale) normalized REY content (grey circles). Normalization of REY contents result in a smooth instead of a zigzag pattern. PAAS data is from Taylor and McLennan (1985) and McLennan (1989).

1.3.2 REY in Seawater

The rare earth elements and yttrium are considered trace elements in seawater with extremely low concentrations, typically in the parts per trillion (ppt) to parts per billion (ppb) range. Their distribution in seawater is not uniform with different REYs having varied solubilities and their behavior in seawater is primarily governed by redox reactions, adsorption and scavenging onto particulate surfaces and complexation processes (e.g., Elderfield et al., 1988; Sholkovitz, 1992; Bau et al., 1995; Alibo & Nozaki, 1999). Furthermore, the residence time of the REY is typically lower than the mixing time of ocean water masses and that is why REY concentrations may vary locally considerably. The REYs tend to form complex ions with various ligands affecting their mobility and availability and redox processes also strongly influence the behavior of REY in aqueous systems. In seawater the inorganic REY speciation is largely controlled by carbonate complexes (CO_3^{2-}) among other inorganic ligands such as OH^- , SO_4^{2-} , F^- , Cl^- or organic ligands (Cantrell & Byrne, 1987; Lee & Byrne, 1993). Carbonate complexes are highly dependent on ionic size and pH and mainly occur as mono $[\text{REYCO}_3^+]$ complexes and di-carbonate $[\text{REY}(\text{CO}_3)_2^-]$ complexes (Byrne & Sholkovitz, 1996; Ohta & Kawabe, 2000; Luo & Byrne, 2004).

There are various sources of REY in modern and ancient oceans, which plays an important role when evaluating the impact of different sources on the (ancient) ocean chemistry and seawater precipitates. Possible sources that introduce REY into modern oceans include input via aeolian particles and ash (Greaves et al., 1999), continental run-off, i.e., REY input through rivers (e.g., Elderfield et al., 1990; Lawrence & Kamber, 2006), leaching processes of REY via pore waters from seafloor sediments (benthic flows, e.g., Byrne & Sholkovitz, 1996; Haley et al., 2004), black smoker-style high-temperature hydrothermal fluids (e.g., German et al., 1990) and anthropogenic REY that are introduced into the oceans by rivers (Bau & Dulski, 1996a; Merschel et al., 2015). The latter is irrelevant when discussing the sources that contribute to the REY budget of ancient oceans.

Modern seawater from various depths and places exhibits subparallel REY_{SN} patterns that only differ in total concentrations (Fig. 7). The uniformity of REY_{SN} patterns throughout the global oceans are indicative of equilibrium circumstances during the ongoing processes of sorption and desorption between REY on particle surfaces and REY solution complexes (e.g., Sholkovitz et al., 1994).

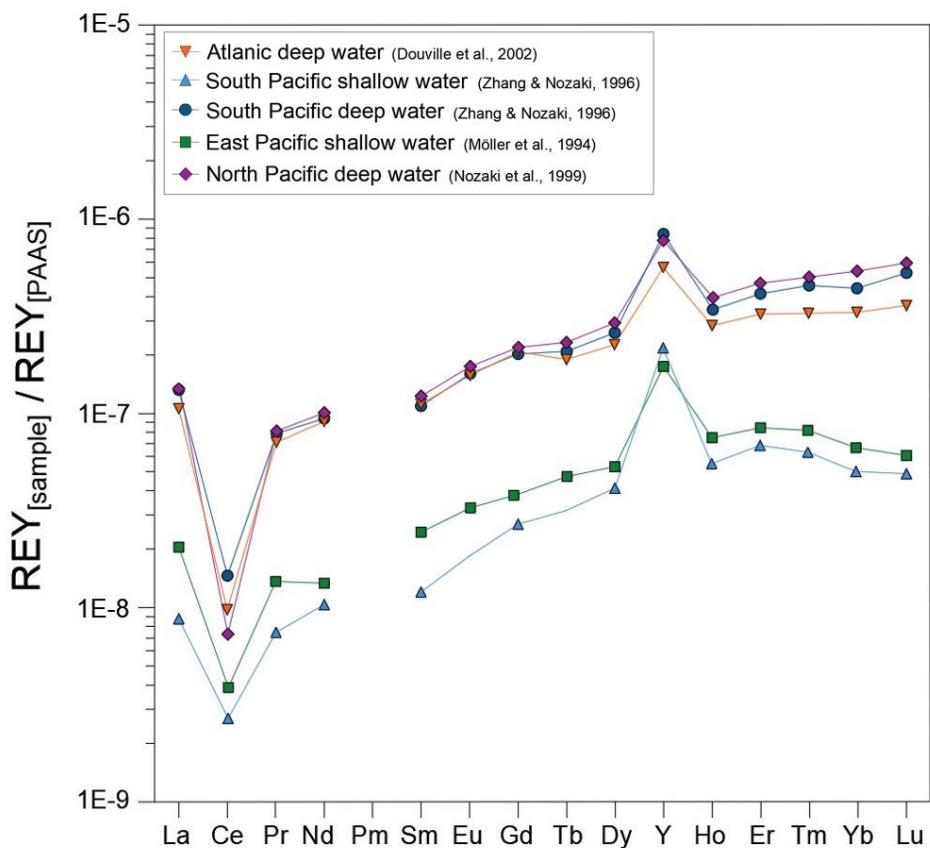


Figure 7: Comparison of shale-normalized REY abundances of modern shallow and deep seawater from the Atlantic and Pacific Oceans. Regardless of its location, modern seawater exhibits parallel REY_{SN} patterns with distinct Ce_{SN} anomalies, HREY_{SN}/LREY_{SN} > 1, and positive La_{SN}, Gd_{SN} and Y_{SN} anomalies.

REY_{SN} patterns reveal the differing behavior of the LREY, MREY, and HREY in seawater, as well as the fractionation processes of the individual REY relative to their neighboring REYs. The typical REY_{SN} patterns of modern seawater show unique features that are (I) an enrichment of HREY_{SN} relative to LREY_{SN}, a (II) strongly negative Ce_{SN} anomaly, (III) positive La_{SN} and Gd_{SN} anomalies, and (IV) a positive Y_{SN} anomaly. In the following these features are explained in more detail:

I. HREY_{SN} enrichment relative to LREY_{SN}

Seawater becomes enriched in HREY because of the competition between REY carbonate complexation and removal of the REY onto particle surfaces. There is a preferential removal of LREYs from particles in surface seawater relative to HREYs, which show a stronger tendency to form complexes with ligands in solution (e.g., Elderfield et al 1988; Erel & Stolper, 1993). As a result, the HREY preferentially remain in solution while the LREY are scavenged onto particulate surfaces.

II. Negative Ce_{SN} anomaly

The most conspicuous feature of the REY_{SN} pattern of modern seawater is a strongly negative Ce_{SN} anomaly. This is due to the redox-sensitive nature of the element where Ce³⁺ is oxidized to the almost insoluble Ce⁴⁺ on particle surfaces such as Mn(IV)- Fe(III)-oxyhydroxides resulting in the removal of Ce from solution and the enrichment of Ce in solid phases. This leaves the residual seawater depleted in Ce (e.g., Alibo & Nozaki, 1999; Slack et al., 2007; Bau & Koschinsky, 2009). Subsequently, Ce_{SN} anomalies are not present in anoxic environments (e.g., Bau & Dulski, 1996b; Alexander et al., 2008), making it an essential tool for assessing the redox conditions of the early Earth (this is discussed in more detail in chapter 5.2).

III. Positive La_{SN} and Gd_{SN} anomalies

Compared to the small positive Gd_{SN} anomalies, positive La_{SN} anomalies are much more pronounced in marine systems, but they remained undetected in the earliest REY studies due to the strong negative anomaly of the neighboring Ce and due to the lack of Pr data. The combined effect of complexation and scavenging is responsible for positive La and Gd anomalies, which may be related to empty (La) and half-filled (Gd) 4f-orbital shells, making these elements more stable in solution relative to their neighboring REY (e.g., De Baar et al., 1991; Lee & Byrne, 1993; Bau et al., 1995). In addition, ad- and desorption processes of the REY onto particulate surfaces also result in fractionation of REY in seawater and consequently to an enrichment of La and Gd in solution.

IV. Positive Y_{SN} anomaly

Yttrium and Ho are considered geochemical twins due to their similar chemical properties, but despite the similarity of their ionic radius, Y and Ho are decoupled in marine systems because of their different electronic configuration (absence of the 4f orbital in Y). This affects the ability of Y to bind onto solid surfaces and, in solution, Y develops more stable carbonate complexes compared to Ho resulting in an enrichment of Y in marine systems (Byrne & Lee, 1993; Sholkovitz et al., 1994; Bau, 1996; Nozaki et al., 1997; Luo & Byrne, 2004). For instance, various studies of sorption processes of REY by Fe- and Mn(oxyhydr)oxides indicate the preferential removal of Ho relative to Y on Fe and Mn particles (e.g., Bau, 1999; Bau & Dulski, 1999; Ohta & Kawabe, 2001). Subsequently, the fractionation process of Y and Ho leads to super-chondritic Y/Ho ratios in modern seawater (cf. Y/Ho_{chondrite} = 26.22, Pack et al., 2007) compared to terrestrial rocks (e.g., Zhang et al., 1994; Bau et al., 1995; Alibo & Nozaki, 1999).

1.3.3 REY geochemistry of marine chemical sediments

The REY compositions of marine chemical sediments are considered to reflect the chemical composition of ancient seawater and pure seawater precipitates may be used as archives of geochemical proxies for ancient seawater at the time of their composition. Therefore, intense studies of REY geochemistry of marine chemical sediments aid to investigate the geochemical evolution of the atmosphere-hydrosphere-lithosphere system of early Earth (e.g., Bau & Möller, 1993; Bau & Dulski, 1996b; Webb & Kamber, 2000; Planavsky et al., 2010).

For many decades, research has been done on abiotic archives such as carbonates, cherts, marine phosphates, or Fe-Mn crusts (e.g., German & Elderfield, 1990; Murray et al., 1992; Bau et al., 1996), but also biogenic substances such as skeletal carbonates (e.g., Sholkovitz & Shen, 1995) and apatites such as fish teeth (e.g., Wright et al., 1987; Toyoda & Tokonami, 1990). However, most geochemical proxies have several drawbacks. In order to evaluate the ancient seawater chemistry, it is necessary that the chemical precipitates, which serve as potential seawater archives, reflect the actual conditions of the ambient seawater. It has to be evaluated if and how syn-depositional processes such as clastic contamination or fractionation processes between chemical sediment and seawater during precipitation and post-depositional processes such as diagenesis or metamorphism have affected the REY geochemistry of the marine chemical precipitates (German & Elderfield, 1990; Bau, 1993; Webb & Kamber, 2000).

Hydrogenetic ferromanganese crusts (Fe-Mn crusts) do not directly reflect the REY chemistry of ambient seawater and are not suitable to evaluate the REY distribution in ancient seawater and the prevailing redox conditions. Especially when Fe-Mn crusts are phosphatized, they might often be affected by diagenetic alterations (Bau et al., 1996). Abiogenic cherts are characterized by rather low REY concentrations and often suffer of considerable detrital contamination (Murray et al., 1992). REY_{SN} patterns of marine phosphates (abiogenic and biogenic) differ from those of modern seawater and show REY concentrations substantially higher relative to ambient seawater. Furthermore, phosphates, such as apatites, may be affected by post-depositional alterations due to pore water interactions during early diagenesis (e.g., German & Elderfield, 1990; Toyoda & Tokonami, 1990). Carbonates (abiogenic and biogenic) mostly can be considered unsuitable seawater REY proxies also due to strong diagenetic alterations. Biogenic carbonates (e.g., skeletal fragments, corals) have very low REY contents and there are inconsistencies of REY fractionation between different taxa and during incorporation into the crystal lattice (Sholkovitz & Shen, 1995). Moreover, all skeletal proxies are limited to the Phanerozoic. However, microbialites such as stromatolites may be reliable geochemical proxies of (shallow) seawater throughout the Phanerozoic, but first occurrences

can be dated back until the Mesoarchean (Webb & Kamber, 2000; Kamber et al., 2004; Bosak et al., 2013). Further advantages of microbialites as geochemical proxies include no fractionation of the REY between seawater and chemical sediment during precipitation, higher REY concentrations with proportional incorporation of the REY chemistry of ambient seawater, and thus they preserve the geochemistry of the fluid from which they precipitated (Webb & Kamber, 2000).

Iron formations are considered to be very useful proxies for the chemical composition of ancient seawater as the precursor minerals, such as Fe(III)-(oxyhydr)oxides, are likely to preserve the chemical signature of the seawater they precipitate of (e.g., Jacobsen & Pimentel-Klose, 1988; Bau & Dulski, 1996b; Bolhar et al., 2004; Konhauser et al., 2017). Their occurrence is confined to the Precambrian, but, in contrast to some other chemical sediments, BIFs show elevated REY concentrations and are thought to withstand significant disturbance during metasomatism or metamorphism (e.g., Bau, 1993; Robbins et al., 2019). Even samples that experienced high metamorphic conditions (e.g., the Eoarchean Isua BIF) show REY_{SN} patterns similar to modern seawater (except for the redox-sensitive elements Ce and Eu; e.g., Appel, 1983; Bolhar et al., 2004; Friend et al., 2008). Furthermore, many BIFs have low concentrations of crustal-sourced elements, such as Al, Zr, Ti, Th, Hf, and Sc, indicating an authigenic origin and the preservation of geochemical signatures uncontaminated by continental detritus. Globally distributed pure BIF samples mimic REY_{SN} features, such as a pronounced HREY_{SN}/LREY_{SN} enrichment, as well as positive La_{SN}, Gd_{SN}, and Y_{SN} anomalies, indicating that similar REY fractionation processes that take place in modern seawater already operated in Precambrian oceans. Moreover, Ce anomalies are commonly used to investigate the redox conditions of ancient seawater. Cerium is highly susceptible to fractionation from other REY; as the oxidation of Ce³⁺ to Ce⁴⁺ under slightly oxidizing conditions greatly reduces the solubility of Ce, it is easily removed from solution onto particulate surfaces such as Mn(IV)-Fe(III)-(oxyhydr)oxides (for more details see Chapter 5.2).

1.4 Objective of this thesis and geological significance

Well-preserved Archean granitoid-greenstone terranes and associated BIFs provide insights into the early period of Earth's history and give significant contributions to understanding geological processes operating at these times (e.g., DeWit & Ashwal, 1997). The oldest BIFs on Earth have been found in metasedimentary successions of the Isua supracrustal belt (3.7-3.8 Ga) in Greenland (e.g., Nutman et al., 1997) and of the Nuvvuagittuq Belt (> 3.8 Ga) in Canada

(e.g., O’Neil et al., 2012; Cates et al., 2013). However, BIFs of these locations suffer from high metamorphic grades, as these rocks have undergone at least amphibolite facies metamorphism.

Rocks of somewhat younger age, but at much better preservation stage are hosted in several cratons in India. Especially the Singhbhum Craton in East India hosts a remarkably well-preserved Archean geological record, with chemical sedimentary successions in the Daitari Greenstone Belt that have only experienced greenschist-facies metamorphic conditions (e.g., Saha, 1994; Mukhopadhyay & Matin, 2020; Hofmann et al., 2022). In the course of this master’s thesis, samples of the ca. 3.5 Ga old Tomka BIF preserved in the Daitari Greenstone Belt are analyzed and characterized. That is slightly younger than the BIFs of the Isua and Nuvvuagittuq Greenstone Belt, but the Tomka BIF only experienced greenschist metamorphic conditions, potentially representing the oldest reliable seawater archive.

The approach of this master’s thesis encompasses trace element analysis via ICP-MS with special attention to REY geochemistry. This is used to reconstruct the Tomka BIF depositional environment, physico-chemical conditions prevailing in the ambient atmosphere-hydrosphere systems, and the sources affecting ancient seawater composition ca. 3.5 Ga ago.

2 Geological Setting

2.1 Geology of the Singhbhum Craton

The ellipsoidal-shaped Singhbhum Craton (East India) extending ~200 km in N-S and ~150 km in E-W direction (Chaudhuri, 2020; Hofmann et al., 2022) consists of different Proterozoic volcano-sedimentary (supracrustal) sequences and Archean greenstone-granitoid rocks ranging in age from 3.5 to 2.5 Ga (Fig. 8, Chaudhuri, 2020; Mukhopadhyay & Matin, 2020). According to many authors (e.g., Sakar & Saha, 1962; Saha, 1994; Olierook et al., 2019; Mukhopadhyay & Matin, 2020), the Archean record is made up by four main units including the Older Metamorphic Group (OMG), the Older Metamorphic Tonalite Gneiss (OMTG), the Singhbhum Granite, and the Iron Ore Group (IOG).

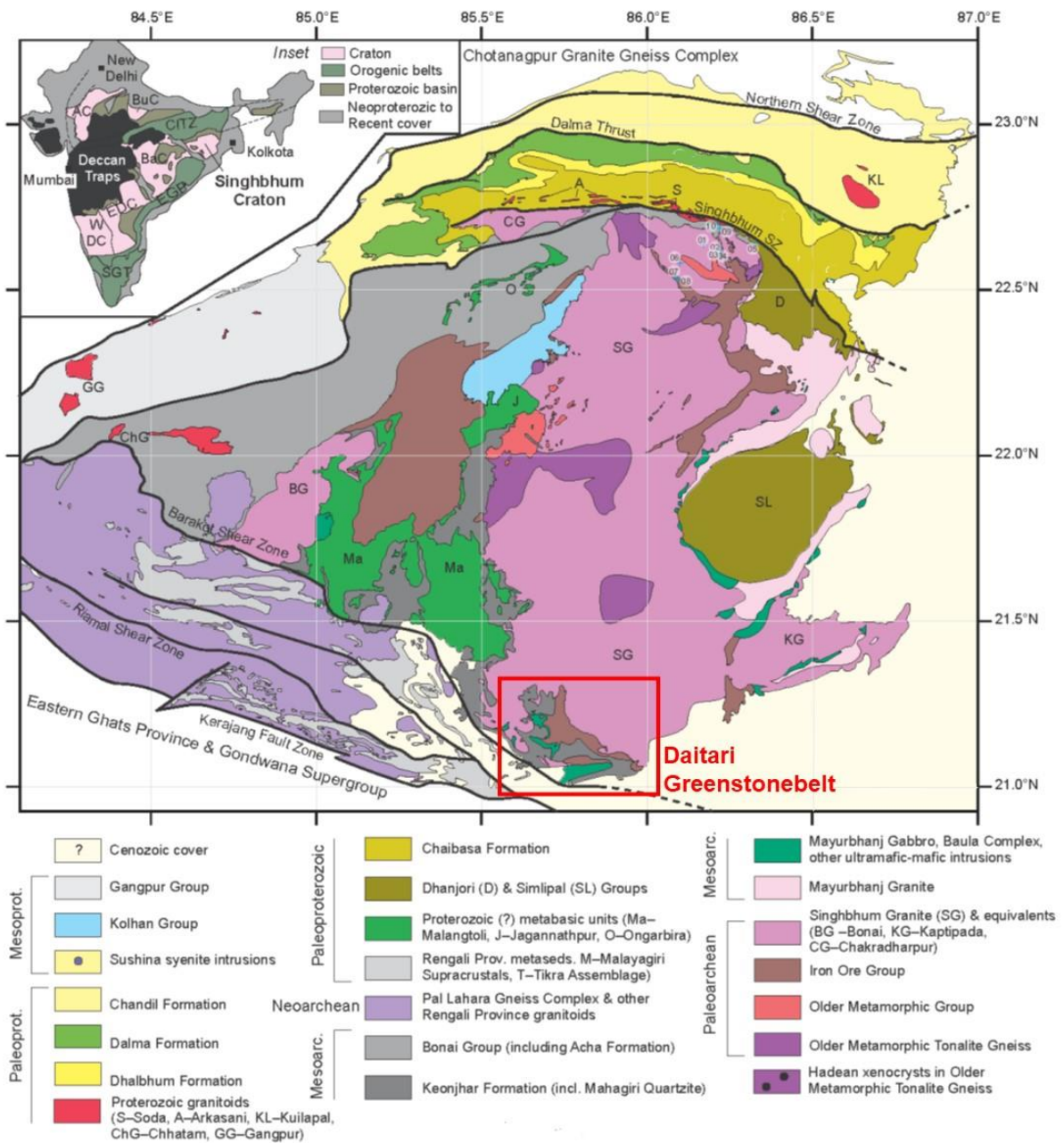


Figure 8: Geological map of the Singhbhum Craton focusing on the Archean and Proterozoic geology (modified from Olierook et al., 2019).

As no differentiation can be made between the OMTG and the Singhbhum Granite, Hofmann et al. (2022) assigned all granitoids of the Singhbhum Craton to the Singhbhum Granitoid Complex (Fig. 9). It includes early, pre-tectonic trondhjemitic-tonalitic gneiss (TTG) plutons (Champua Suite), a suite of granodioritic to granitic rocks (Singhbhum Suite) and late, post-tectonic syenites and K-feldspar granites (Mayurbhanj Suite, Nelson et al., 2014; Dey et al., 2017; Mitra et al., 2019; Olierook et al., 2019; Pandey et al., 2019; Hofmann et al., 2022; Mitra et al., 2022). The Badampahar Group (formerly known as the Eastern and Southern Iron Ore Group) comprises the oldest rocks so far observed in the Singhbhum Craton where felsic rocks

were dated between 3.53 and 3.51 Ga (Fig. 9). It is a typical Paleoproterozoic greenstone assemblage of submarine volcanic rocks and marine chemical sedimentary rocks, and such successions are present in the Daitari, Gorumahisani, and Nausahi greenstone belts (Iyengar & Murthy, 1982; Jena & Behra, 2000).

The suite of supracrustal rocks of the “OMG” that experienced amphibolite facies metamorphism (Acharyya, 1993; Jena & Behra, 2000) can be assigned to medium- to high-grade equivalents of the Badampahar Group greenstones (Hofmann et al., 2022). The Badampahar Group includes important successions of high-grade iron ore deposits associated with BIFs and experienced metamorphic grades not higher than greenschist facies (Mukhopadhyay et al., 2012; Chaudhuri, 2020; Mukhopadhyay & Matin, 2020; Jodder, 2021; Hofmann et al., 2022). The Banded Iron Formation samples studied in this thesis originate from the Daitari Greenstone Belt and are described in more detail below. The granitoid-greenstone terrains of the Singhbhum Craton are non-conformably overlain by the Koira Group (formerly known as the Western Iron Ore Group, Murthy & Acharya, 1975), consisting of intracontinental volcano-sedimentary successions (Fig. 9).

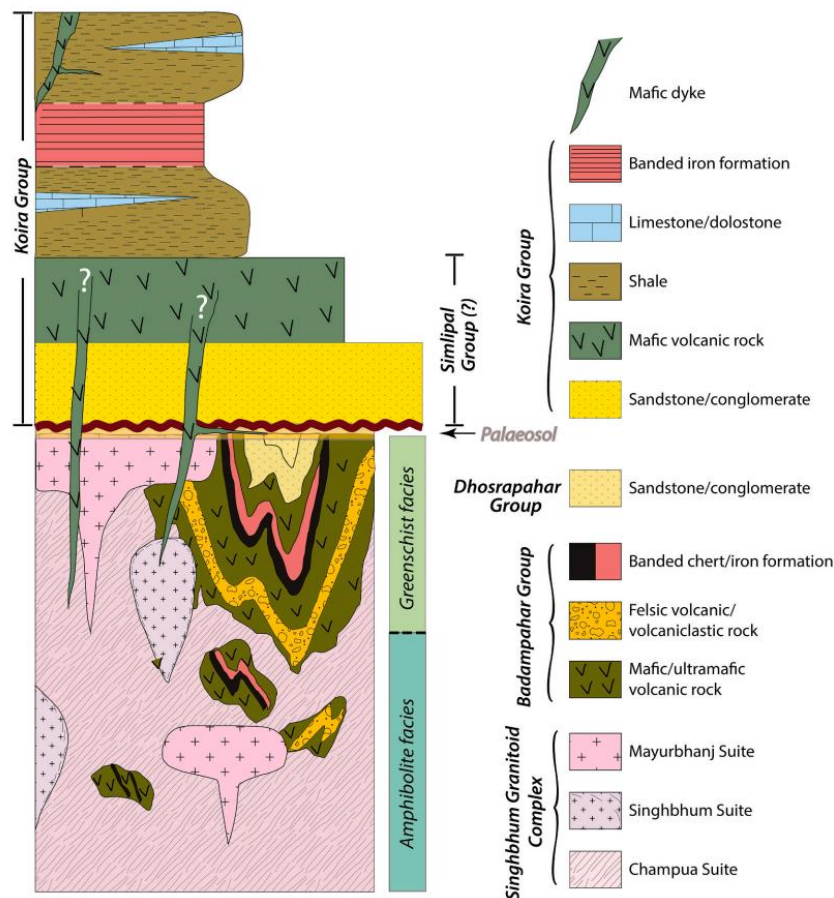


Figure 9: Stratigraphy of the Archean geology of the Singhbhum Craton (from Hofmann et al., 2022).

2.2 The Daitari Greenstone Belt

2.2.1 Geology of the Daitari Greenstone Belt

The Daitari Greenstone Belt (DGB) is located in the southern part of the Singhbhum Craton (Fig. 8) and represents a well-preserved Paleoproterozoic supracrustal succession that ranges from ~3.53 to 3.35 Ga (Jodder, 2021; Hofmann et al., 2022; Jodder et al., 2023). Mukhopadhyay et al. (2008) reported a U–Pb SHRIMP age of 3507 ± 2 Ma where zircon grains from a dacitic lava that directly underlies the here studied Tomka BIF of the DGB had been analyzed. A more recent study reported an age of 3573 ± 63 Ma for mafic-ultramafic rocks and 3507 ± 180 Ma for felsic volcanic rocks of the DGB, respectively (Adhikari et al., 2021). The DGB consists of a ~7 km thick volcano-sedimentary package that shows a greenschist facies metamorphic grade and comprises 3.35 Ga old granitoid intrusions of the Singhbhum Craton. This succession is unconformably overlain by the ≤ 3.0 Ga old Mahagiri Quartzite (Jodder, 2021; Jodder et al., 2023).

The volcano-sedimentary package of the DGB is assigned to the Paleoproterozoic Badampahar Group and can be subdivided into five major lithostratigraphic formations (from oldest to youngest): the Kalisagar, Tapalda, Sindurimundi, Tomka, and Talangi Formations (Fig. 10). The stratigraphically lowest unit is the Kalisagar Formation (~3 km thick) and consists of submarine mafic and ultramafic volcanic successions including pillow basalts and komatiites with thin slate and chert units. This unit is sharply overlain by the ~1.5 km thick Tapalda Formation that is mostly a volcanoclastic succession comprising dacitic to rhyodacitic rocks and minor interbedded chert units. The overlying Sindurimundi Formation (~500 m thick) primarily comprises siliciclastic units of proximal to distal turbidity current deposits with thin chert layers and minor mafic volcanics. The nearly 700 m thick Tomka Formation consists of an extensive chemical sedimentary sequence (BIF) and samples of this formation are a major focus of this thesis. The uppermost Talangi Formation (~1 km thick) consists mostly of mafic volcanics and minor komatiites with thin interbedded cherts indicating a sub-aquatic setting (Jodder, 2021; Jodder et al., 2023).

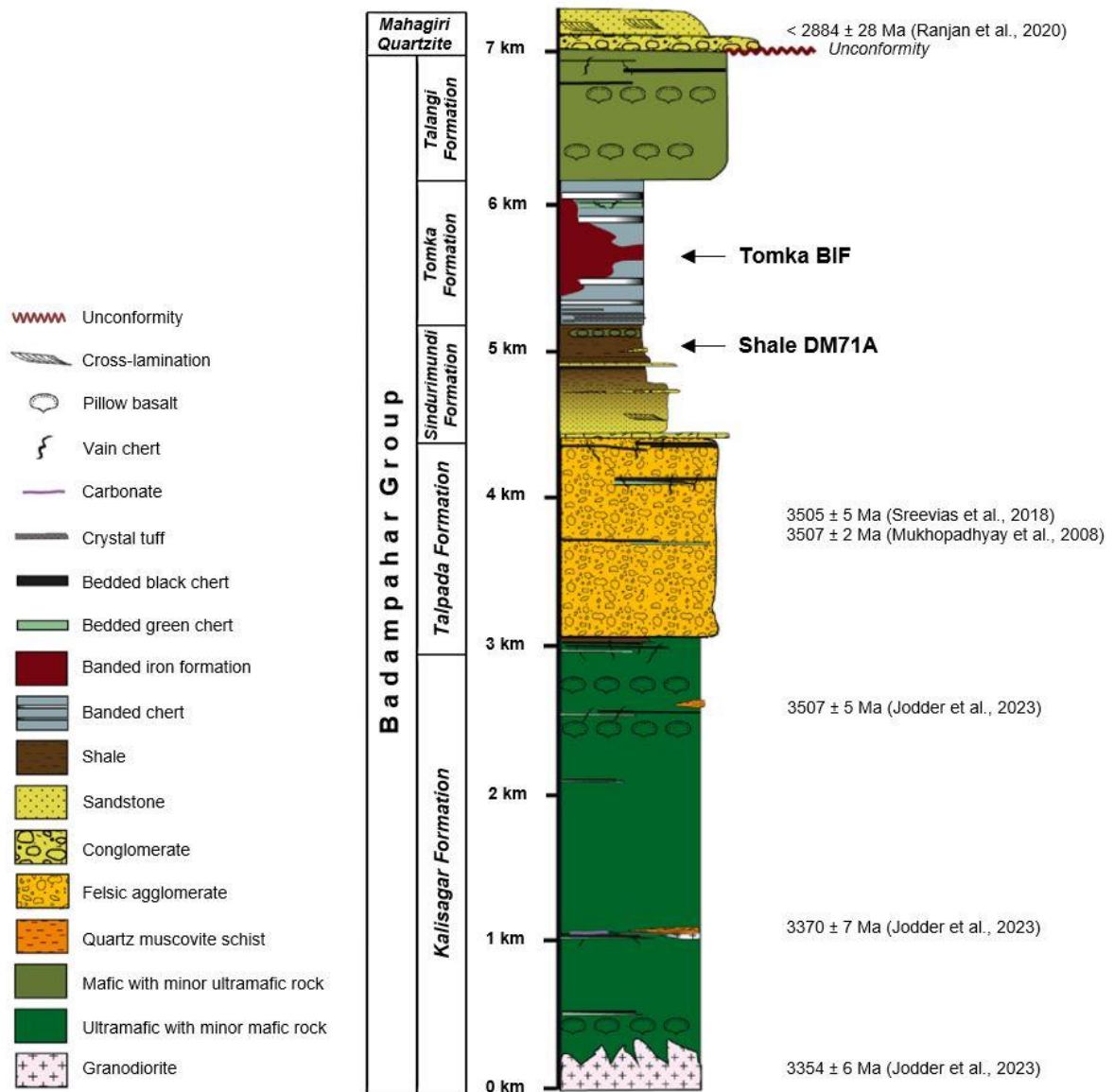


Figure 10: Stratigraphic log of the volcano-sedimentary succession of the Daitari greenstone belt (modified from Jodder, 2021).

2.2.2 BIFs preserved in the Tomka Formation

The Daitari Greenstone Belt hosts a significant iron ore deposit associated with the Banded Iron Formation exposed in the Tomka Formation, which is named after the Tomka mountain range. This BIF is not only of scientific interest, but the high-grade iron ore (60-62% Fe) is also currently being mined by the state-owned Odisha Mining Corporation (OMC). Field observations done by Jodder in 2021 suggest that the base of the Tomka Formation with the underlying Sindurimundi turbidite sequence is widely sharp and conformable. Furthermore, Jodder et al. (2023) suggested a maximum age of deposition of the Sindurimundi Formation to be $3502 \pm 2 \text{ Ma}$. The upper contact of the Tomka Formation with the Talangi Formation is largely unexposed but inferred to be conformable, where the contact between chemical sediments and overlying mafic volcanic rocks can be observed. The stratigraphic unit is

dominantly made up by banded black- and white-cherts with iron formations including lithologies such as green chert, grey chert, and granular chert. The iron formation exposed in the Tomka Formation displays pure orthochemical sedimentary rocks which are, as well as the banded black-and white-chert, resistant to weathering. In the DGB the iron formation that is referred here as banded iron formation (BIF) is represented by banded red- and white-chert. The BIF of the Tomka Formation displays finely laminated, bedded rocks made-up of alternating layers of magnetite or hematite with translucent to white-weathered chert or Fe-rich silicate (Jasper, Jodder, 2021; Jodder et al., 2023).

3 Samples and analytical methods

3.1 Samples and preparation

Eleven different rock samples were used for chemical analysis (Tab. 2). The DM17 sample series, DM22 sample series and samples DM76A, DM71A and DM90 were collected by A. Hofmann and J. Jodder; the IND-DGB-BIF sample series was collected by S. Viehmann in 2020 at the vicinity of OMC iron ore mine. All samples are BIF samples from the Tomka Formation except for DM71A which is a shale from the directly underlying Sindurimundi Formation (Fig.10). All BIF samples show fine lamination (< 1 mm to 1 cm) with grey-metallic Fe-bands and white-greyish or red (Jasper) chert layers (for sample photographs see appendix). Individual BIF layers (chert, Fe-band and mixed bands) were cut by a diamond saw at the Department of Geology, University of Vienna, to get 29 samples in total (9 chert-, 5 Fe- and 15 mixed bands). Subsequently these samples (along with the shale sample DM71A) were dried, crushed, and homogenized in an agate mill (Retsch RM2000 Agate Mill) to produce homogenous sample powders for further analysis.

Table 2: Listing of the individual Tomka BIF sample layers with information on their GPS locality.

Sample	Latitude	Longitude	Sample layer-ID	Layer type
DM17C	21.0945	85.8841	DM17C 1	Chert
			DM17C 2	Chert
			DM17C 3	Fe-band
			DM17C 4	Mixed bands
DM17D	21.0945	85.8841	DM17D 1	Chert
			DM17D 2	Chert
DM17E	21.0945	85.8841	DM17E 1	Chert
			DM17E 2	Chert
			DM17E 3	Chert
DM22B	stream samples*		DM22B 1	Mixed bands
			DM22B 2	Mixed bands
			DM22B 3	Mixed bands
			DM22B 4	Mixed bands
DM22C	stream samples*		DM22C 1	Mixed bands
			DM22C 2	Mixed bands
DM22D	stream samples*		DM22D 1	Fe-band
			DM22D 2	Fe-band
DM76A	21.1306	85.7709	DM76A 1	Chert
			DM76A 2	Chert
DM90	21.1001	85.7925	DM90 1	Fe-band
			DM90 2	Mixed bands
IND-DGB-Bif2-1	21.5634	85.4871	IND-DGB-Bif2-1a	Mixed bands
			IND-DGB-Bif2-1b	Mixed bands
IND-DGB-Bif2	21.5634	85.4871	IND-DGB-Bif2 1	Fe-band
			IND-DGB-Bif2 2	Mixed bands
			IND-DGB-Bif2 3	Mixed bands
			IND-DGB-Bif2 4	Mixed bands
			IND-DGB-Bif2 5	Mixed bands
			IND-DGB-Bif2 6	Mixed bands
DM71A	21.1131	85.7981	DM71A	Shale

*no specific locality

3.2 ICP-MS analysis

Trace element concentrations were determined at the Department of Lithospheric Research at the University of Vienna, following the protocol described in Viehmann et al. (2016). Thirty-two homogenized samples including the BIF reference standard IF-G (from a banded iron formation in the Isua supracrustal belt, west Greenland) and the shale sample DM71A were digested in high pressure-high temperature Picotrace digestion blocks at 180 °C in a mix of 10 ml of suprapure HCl, HNO₃ and HF (3:1:1) for three days to ensure complete sample dissolution. The acid-sample mixture was evaporated to dryness at 120 °C; the residues were

re-dissolved in 5 ml suprapure conc. HCl twice and evaporated again. The samples were eventually re-dissolved in in 0.5 M HNO₃ + trace HF (0.01 M) for ICP-MS analyses. The dilution factor for measuring trace element concentrations was ca. 1:3500 and was carried out using a quadrupole iCap RQ ICP-MS.

4 Results

4.1 Normalization of REY and calculation of REY_{SN} anomalies

REY concentrations are normalized to Post-Archean Australian Shale (PAAS, subscript SN; Taylor & McLennan, 1985; McLennan, 1989) and C1 chondrite (subscript CN; Anders & Grevesse, 1989). Quantifying the magnitude of anomalies in REY distributions is often complex as neighboring REYs themselves may show anomalous behavior in aqueous solutions; this is, for instance, the case with the redox-sensitive elements Ce and Eu, where La and Gd may show positive anomalies in solution. Anomalies of normalized REY abundances are calculated after Bau and Dulski (1996) and Bolhar et al. (2004), avoiding REY that may show anomalous behavior, and are defined as follows:

$$(La/La^*)_{SN} = La_{SN}/(3Pr_{SN}-2Nd_{SN});$$

$$(Ce/Ce^*)_{SN} = Ce_{SN}/(2Pr_{SN}-Nd_{SN});$$

$$(Eu/Eu^*)_{SN} = Eu_{SN}/(0.67Sm_{SN} + 0.33Tb_{SN});$$

$$(Gd/Gd^*)_{SN} = Gd_{SN}/(2Tb_{SN} + Dy_{SN});$$

$$(Eu/Eu^*)_{CN} = Eu_{CN}/(0.67Sm_{CN} + 0.33Tb_{CN}).$$

4.2 Rare earth elements and other trace elements

Trace element concentrations of cherts, Fe-bands and mixed Fe- and chert-bands from the Tomka BIF cover a broad range and include the upper ppt to the lower ppm level (Tab. 3).

Almost immobile trace elements, such as Zr, Th and Hf (e.g. Bau, 1993), are often below the detection limits (Hf, Th) in the Tomka BIF samples and, when measurable, elemental concentrations are very low at < 0.1 ppm and < 0.07 ppm, respectively. Zr concentrations range from 0.13 ppm to 2.84 ppm, with 21 samples having Zr concentrations below 1.0 ppm (Fig. 11). The shale DM71A, on the other hand, shows significant higher concentrations of Zr (116 ppm), Th (5.87 ppm) and Hf (3.18 ppm).

Table 3: Trace element concentrations (in ppm) of Tomka BIF and shale sample (LOQ = limit of quantification).

LOQ	Sample-ID	DMI7E1	DMI7E2	DMI7E3	DM76A1	DM76A2	DMI7C1	DMI7C2	DMI7C3	DMI7C4	DMI7D1	DMI7D2	DM22D1	DM22D2
Type		Chert	Fe-band	Mixed bands	Chert	Chert	Fe-band	Fe-band						
0.0069	Rb	0.018	0.035	0.026	0.085	0.022	0.246	0.110	0.094	0.071	0.037	0.089	0.205	0.209
0.0534	Sr	0.21	0.10	0.33	1.64	0.63	0.17	0.60	1.28	0.32	1.03	0.34	0.87	1.82
0.0304	Y	0.29	0.29	0.47	50.8	19.1	2.89	0.59	1.73	0.59	0.30	0.48	7.55	8.79
0.0871	Zr	0.21	0.36	0.22	1.40	0.36	0.55	0.24	0.21	0.81	0.17	0.23	0.81	1.53
0.0009	Cs	0.001	0.002	0.002	0.006	0.004	0.009	0.010	0.010	0.012	0.007	0.009	0.007	0.009
0.0052	La	0.146	0.068	0.175	11.6	1.88	0.458	0.085	0.422	0.075	0.059	0.066	4.48	13.5
0.0132	Ce	0.33	0.15	0.38	25.4	4.25	0.67	0.13	0.64	0.13	0.10	0.09	2.47	5.81
0.0013	Pr	0.047	0.022	0.060	3.20	0.546	0.069	0.015	0.072	0.015	0.013	0.009	0.412	0.860
0.0044	Nd	0.225	0.107	0.307	13.6	2.32	0.286	0.067	0.330	0.065	0.062	0.043	1.60	2.98
0.0007	Sm	0.056	0.033	0.082	3.96	0.919	0.075	0.019	0.083	0.019	0.018	0.012	0.275	0.422
0.0012	Eu	0.017	0.009	0.023	0.858	0.251	0.044	0.014	0.048	0.013	0.010	0.012	0.146	0.220
0.0007	Gd	0.050	0.037	0.065	5.66	1.95	0.188	0.039	0.133	0.037	0.025	0.029	0.474	0.723
0.0004	Tb	0.006	0.005	0.008	0.997	0.374	0.036	0.006	0.022	0.006	0.004	0.006	0.069	0.094
0.0006	Dy	0.032	0.032	0.051	6.30	2.47	0.268	0.049	0.166	0.047	0.027	0.042	0.494	0.612
0.0008	Ho	0.007	0.007	0.011	1.33	0.523	0.062	0.012	0.042	0.012	0.007	0.009	0.127	0.150
0.0002	Er	0.019	0.021	0.033	4.08	1.53	0.192	0.041	0.131	0.043	0.024	0.030	0.399	0.479
0.0002	Tm	0.003	0.004	0.005	0.582	0.223	0.026	0.006	0.020	0.007	0.004	0.004	0.055	0.067
0.0016	Yb	0.020	0.026	0.035	3.81	1.43	0.154	0.045	0.142	0.047	0.031	0.028	0.352	0.429
0.0003	Lu	0.003	0.004	0.006	0.536	0.199	0.023	0.008	0.023	0.008	0.005	0.004	0.056	0.068
0.0363	Hf	<LOQ	<LOQ	<LOQ	0.06	<LOQ	<LOQ	<LOQ	<LOQ	<LOQ	<LOQ	<LOQ	<LOQ	0.04
0.0047	Th	<LOQ	0.017	0.006	0.042	0.006	0.022	<LOQ	0.008	0.007	<LOQ	<LOQ	0.033	0.076
0.0039	U	0.005	0.005	0.008	0.108	0.037	0.008	<LOQ	0.010	0.005	<LOQ	<LOQ	0.012	0.020
	Y/Ho	41.6	44.6	42.7	38.3	36.5	46.3	47.6	41.2	48.2	43.2	53.5	59.4	58.5
	ΣREY	1.25	0.813	1.71	133	38.0	5.44	1.14	4.00	1.11	0.682	0.864	19.0	35.2
	La _{SN} /La ^{*SN}	1.48	1.43	2.09	1.05	1.01	1.85	2.26	2.26	1.68	1.89	3.01	2.56	3.03
	Ce _{SN} /Ce ^{*SN}	1.06	0.974	1.08	0.980	0.97	1.18	1.29	1.24	1.13	1.03	1.37	0.672	0.68
	Eu _{SN} /Eu ^{*SN}	1.71	1.37	1.56	0.879	0.856	1.67	2.56	2.27	2.47	2.45	2.83	2.16	2.23
	Gd _{SN} /Gd ^{*SN}	1.34	1.25	1.28	0.989	0.955	1.16	1.41	1.28	1.25	1.16	1.12	1.41	1.38
	Yb _{SN} /Pr _{SN}	1.35	3.69	1.82	3.73	8.19	7.02	9.73	6.18	10.1	7.40	9.54	2.67	1.56
	Eu _{CN} /Eu ^{*CN}	0.985	0.826	0.904	0.564	0.587	1.17	1.70	1.47	1.64	1.56	1.64	1.38	1.41

Table 3 (continued)

Sample-ID	DM22B 1	DM22B 2	DM22B 3	DM22B 4	DM22C 1	DM22C 2	DM90 1	DM90 2	IND-DGB-Bif2-1a	IND-DGB-Bif2-1b	IND-DGB-Bif2 1
LOQ	Type	Mixed bands	Mixed bands	Mixed bands	Mixed bands	Fe/Chert	Fe-band	Mixed bands	Mixed bands	Mixed bands	Mixed bands
0.0069	Rb	0.626	1.12	1.41	0.073	0.191	0.182	0.029	0.140	0.057	0.035
0.0534	Sr	0.49	0.40	0.86	0.29	0.29	2.59	0.17	0.51	0.60	0.23
0.0304	Y	2.02	6.73	16.7	1.30	6.24	7.47	10.1	5.05	31.9	20.3
0.0871	Zr	0.42	0.89	2.01	0.27	0.20	1.11	0.27	1.30	2.84	0.49
0.0009	Cs	0.014	0.018	0.022	0.005	0.008	0.038	0.008	0.136	0.114	0.064
0.0052	La	0.782	0.958	3.56	2.26	1.32	5.07	0.753	0.410	1.84	1.70
0.0132	Ce	0.75	1.20	4.71	2.60	1.41	6.29	0.87	0.56	2.27	2.22
0.0013	Pr	0.094	0.182	0.567	0.269	0.152	0.786	0.104	0.069	0.281	0.291
0.0044	Nd	0.417	0.821	2.51	1.13	0.644	3.36	0.431	0.324	1.33	1.45
0.0007	Sm	0.089	0.229	0.622	0.203	0.130	0.667	0.112	0.113	0.510	0.489
0.0012	Eu	0.066	0.142	0.419	0.074	0.082	0.316	0.106	0.088	0.435	0.385
0.0007	Gd	0.142	0.379	1.11	0.171	0.283	0.748	0.427	0.297	1.49	1.13
0.0004	Tb	0.020	0.066	0.178	0.016	0.046	0.086	0.076	0.056	0.283	0.188
0.0006	Dy	0.134	0.492	1.27	0.091	0.354	0.539	0.576	0.415	2.31	1.38
0.0008	Ho	0.032	0.128	0.318	0.023	0.094	0.130	0.155	0.102	0.620	0.359
0.0002	Er	0.103	0.375	1.00	0.075	0.286	0.412	0.492	0.334	1.96	1.15
0.0002	Tm	0.014	0.054	0.139	0.010	0.037	0.057	0.067	0.051	0.286	0.153
0.0016	Yb	0.087	0.365	0.858	0.073	0.227	0.359	0.427	0.346	1.83	1.00
0.0003	Lu	0.015	0.056	0.141	0.013	0.038	0.062	0.071	0.059	0.300	0.168
0.0363	Hf	<LOQ	<LOQ	0.05	<LOQ	<LOQ	<LOQ	<LOQ	<LOQ	0.07	<LOQ
0.0047	Th	0.010	0.024	0.089	0.011	0.006	0.036	0.009	0.034	0.103	0.020
0.0039	U	0.008	0.015	0.024	0.008	0.007	0.039	0.013	0.020	0.040	0.025
	Y/Ho	63.0	62.9	52.4	56.0	66.7	57.4	65.1	49.4	51.4	56.4
	ΣREY	4.77	14.8	34.1	8.30	11.3	26.3	14.7	8.28	47.6	32.3
	La _{SN} /La* _{SN}	2.74	1.85	2.08	2.39	2.56	1.92	1.97	2.44	2.84	3.34
	Ce _{SN} /Ce* _{SN}	1.04	0.894	1.08	1.19	1.16	1.00	1.00	1.14	1.17	1.21
	Eu _{SN} /Eu* _{SN}	3.17	2.69	2.57	2.18	2.13	2.50	2.12	2.15	2.20	2.56
	Gd _{SN} /Gd* _{SN}	1.31	1.14	1.27	1.64	1.38	1.49	1.24	1.13	1.34	1.27
	Yb _{SN} /Pr _{SN}	2.90	4.79	4.73	0.855	4.68	1.43	12.8	15.6	20.4	10.8
	Eu _{CN} /Eu* _{CN}	2.00	1.73	1.68	1.23	1.43	1.48	1.56	1.52	1.58	1.74

Table 3 (continued)

Sample-ID	IND-DGB-Bif2 2	IND-DGB-Bif2 3	IND-DGB-Bif2 4	IND-DGB-Bif2 5	IND-DGB-Bif2 6	DM71A	
LOQ	Type	Mixed bands	Mixed bands	Mixed bands	Mixed bands	Mixed bands	Shale
0.0069	Rb	0.077	0.328	0.328	0.276	0.044	85.4
0.0534	Sr	0.32	1.28	1.31	0.62	0.20	28.1
0.0304	Y	8.43	21.5	27.3	3.02	0.99	11.0
0.0871	Zr	0.49	2.08	1.69	0.59	0.13	116
0.0009	Cs	0.118	0.137	0.137	0.133	0.105	<LOQ
0.0052	La	0.593	1.71	2.44	0.521	0.204	16.5
0.0132	Ce	0.76	2.22	3.11	0.44	0.14	32.8
0.0013	Pr	0.103	0.260	0.385	0.057	0.019	3.70
0.0044	Nd	0.507	1.26	1.76	0.246	0.081	13.3
0.0007	Sm	0.170	0.413	0.529	0.077	0.024	2.75
0.0012	Eu	0.136	0.317	0.383	0.051	0.017	0.783
0.0007	Gd	0.413	1.10	1.41	0.160	0.048	2.58
0.0004	Tb	0.069	0.205	0.268	0.028	0.008	0.365
0.0006	Dy	0.548	1.65	2.05	0.220	0.063	2.05
0.0008	Ho	0.147	0.422	0.526	0.057	0.017	0.419
0.0002	Er	0.479	1.40	1.63	0.193	0.057	1.33
0.0002	Tm	0.068	0.194	0.212	0.029	0.007	0.200
0.0016	Yb	0.439	1.26	1.27	0.187	0.056	1.41
0.0003	Lu	0.076	0.203	0.204	0.030	0.009	0.212
0.0363	Hf	<LOQ	0.05	<LOQ	<LOQ	<LOQ	3.18
0.0047	Th	0.012	0.067	0.061	0.012	<LOQ	5.87
0.0039	U	0.018	0.020	0.021	0.006	<LOQ	1.37
	Y/Ho	57.4	51.0	51.9	52.6	58.5	26.3
	∑REY	12.9	34.2	43.5	5.31	1.73	89.4
	La _{SN} /La* _{SN}	2.98	3.19	2.39	2.87	3.43	0.913
	Ce _{SN} /Ce* _{SN}	1.12	1.29	1.11	0.987	0.930	0.923
	Eu _{SN} /Eu* _{SN}	2.51	2.13	1.98	2.21	2.47	1.49
	Gd _{SN} /Gd* _{SN}	1.43	1.33	1.19	1.42	1.35	1.09
	Yb _{SN} /Pr _{SN}	13.3	15.2	10.4	10.4	9.47	1.19
	Eu _{CN} /Eu* _{CN}	1.72	1.50	1.40	1.49	1.65	0.883

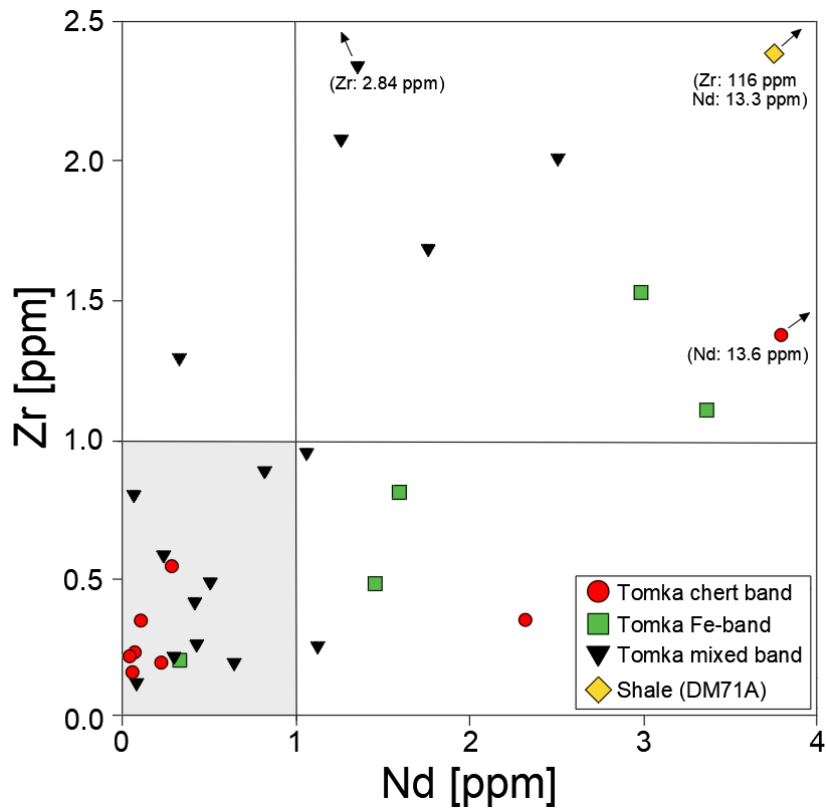


Figure 11: Graph of Zr vs. Nd concentrations of the Tomka chert-, Fe- and mixed BIF bands, and the shale sample DM71A. Most Tomka BIF samples have very low concentrations of the immobile trace elements (such as Zr) relative to clastic sediments.

The BIF samples have $\sum\text{REY}$ concentrations of < 47.0 ppm except for one outlier (DM76A 1) with a $\sum\text{REY}$ concentration of 133 ppm. In contrast, the shale sample has a $\sum\text{REY}$ concentration of 89.4 ppm. The individual cherts, Fe-bands and mixed bands of the Tomka BIF samples have predominantly sub-parallel REY_{SN} patterns, the patterns of sample DM76A 1, DM76A 2 and the shale sample DM71A are rather flat (Fig.12).

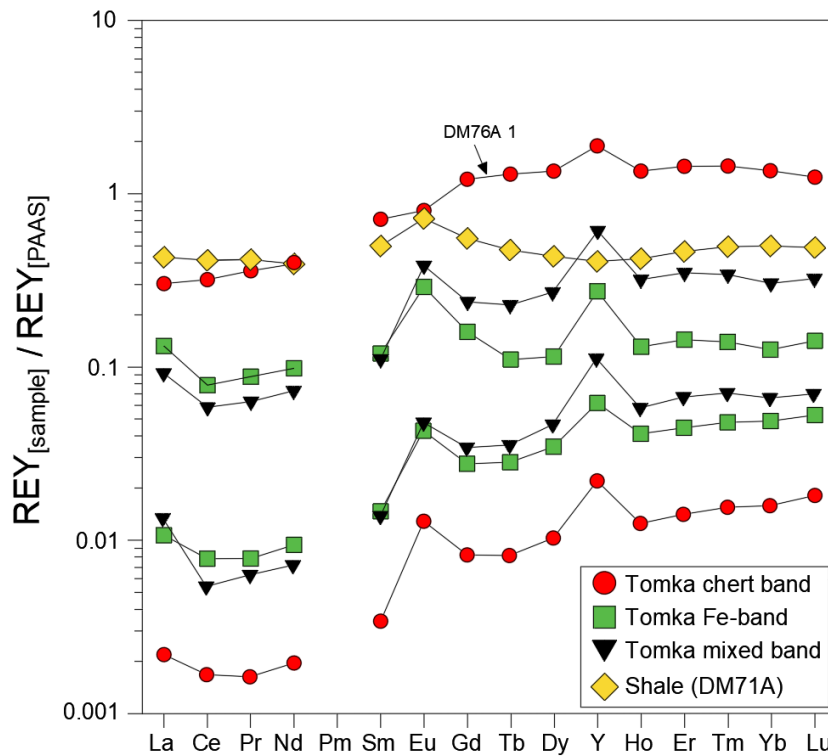


Figure 12: Representative REY_{SN} patterns of Tomka BIF chert-, Fe- and mixed bands and shale sample DM71A.

Common features of modern seawater are an enrichment of $HREY_{SN}$ relative to $LREY_{SN}$, as well as Y_{SN} anomalies, and were quantified using Yb_{SN}/Pr_{SN} ratios and Y/Ho ratios, respectively. Yb_{SN}/Pr_{SN} ratios range from 0.86 to 20.4 with 22 samples displaying ratios > 3.0 . Due to the close similarity between Y and Ho resulting in coherent geochemical behavior, an anomalous behavior of Y can be identified using Y/Ho ratios (e.g., Bau & Dulski, 1996b; Bolhar et al., 2004), which can be observed in all Tomka BIFs. The samples have superchondritic Y/Ho ratios ($Y/Ho_{chondrite} = 26.22$, Pack et al., 2007) and range from 36.5 to 66.7. The shale DM71A displays a Yb_{SN}/Pr_{SN} ratio of 1.19 and a rather chondritic Y/Ho ratio of 26.3. The REY_{SN} patterns of all BIF samples exhibit positive La_{SN} , small positive Gd_{SN} and positive Eu_{SN} anomalies. Positive La_{SN} anomalies are strongly developed, and with La_{SN}/La^*_{SN} ratios between 1.43 and 3.43, only two samples (DM76A 1 and DM76A 2) show rather minor to non-existent La_{SN} anomalies with ratios of 1.01 and 1.05, respectively (Fig. 13). BIF samples are largely characterized by small positive Gd_{SN} anomalies with calculated Gd_{SN}/Gd^*_{SN} ratios between 0.96 and 1.64 with 21 samples showing ratios > 1.2 . The shale sample shows insignificant positive La_{SN} and Gd_{SN} anomalies with 0.91 and 1.09, respectively. Furthermore, Tomka BIFs show throughout positive Eu_{SN} anomalies with Eu_{SN}/Eu^*_{SN} ratios ranging between 1.27 and 3.17 (exception: samples DM76A 1 and DM76A 2 with $Eu_{SN}/Eu^*_{SN} = 0.86$ and 0.88, respectively). When BIFs are normalized to C1 chondrite to erase normalization artifacts related

to shale normalization, positive Eu anomalies are also observed with $\text{Eu}_{\text{CN}}/\text{Eu}^*_{\text{CN}}$ ratios between 1.17 and 2.0 except for five samples < 1.0 . Shale sample DM71A exhibits small positive $\text{Eu}_{\text{SN}}/\text{Eu}^*_{\text{SN}}$ but no anomalous $\text{Eu}_{\text{CN}}/\text{Eu}^*_{\text{CN}}$ ratios with 1.49 and 0.88, respectively. Small positive Ce_{SN} anomalies can be observed in the Tomka BIF samples ($\text{Ce}_{\text{SN}}/\text{Ce}^*_{\text{SN}}$: 0.672-1.37) and in the shale sample (0.913).

No significant differences in REY_{SN} patterns and REY anomalies between individual cherts, Fe-bands and mixed bands can be observed. That is why no differentiation is made between both sample types in the following discussion.

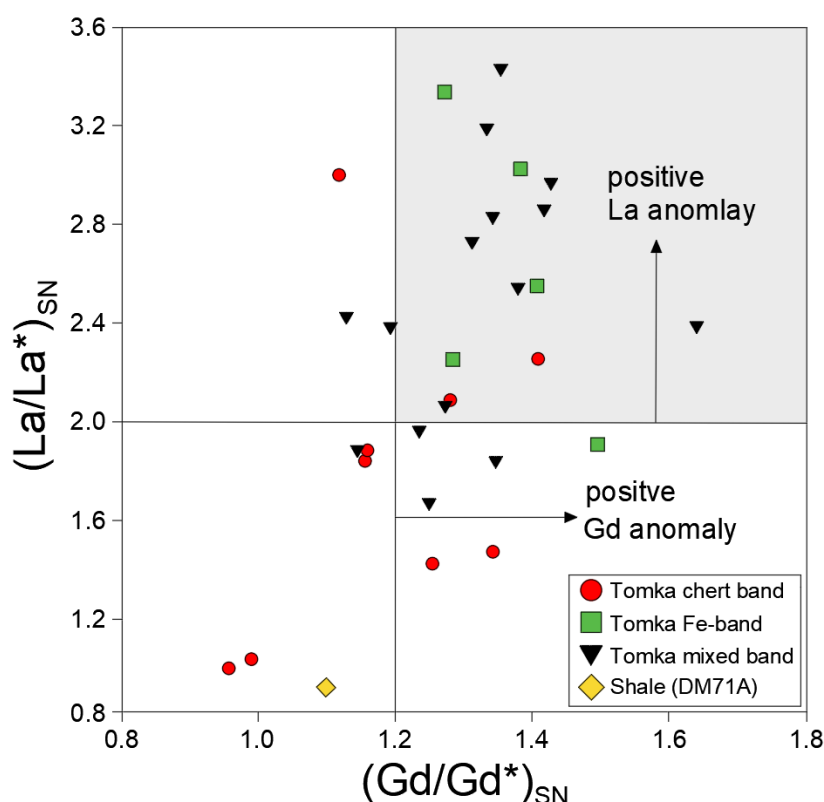


Figure 13: Graph of $\text{La}_{\text{SN}}/\text{La}^*_{\text{SN}}$ ratio vs $\text{Gd}_{\text{SN}}/\text{Gd}^*_{\text{SN}}$ ratio of Tomka BIF chert-, Fe- and mixed bands as well as the shale DM71A. Positive La_{SN} and Gd_{SN} anomalies (grey box) are characteristics of both, modern and Archean seawater. Most Tomka BIF samples plot in the grey box and can be considered as pure chemical sediments.

4.3 Data quality

The sample digestion procedure included the preparation and analysis of a procedural blank solution and a measured acid blank to determine the limit of quantification (LOQ) of each measured element (Tab. 4). Only element concentrations exceeding the LOQ are listed, otherwise the data are unusable for a further discussion.

The sample digestion process also included two analyses of the BIF reference standard IF-G (IF-G 1 + IF-G 2, Tab. 4) to calculate the relative standard deviation (% RSD). For most elements the RSD is < 5 % and exceeds 10 % only a few times; elements with RSDs of > 10 % are not considered for a further discussion (a complete data set can be found in the appendix).

The results of IF-G 1 and IF-G 2 mostly agree with published values from Dulski (2001), Bolhar et al. (2004) and Sampaio and Enzweiler (2015). When comparing element concentrations of REY, concentrations of LREY (average % RSD: 1.07) of IF-G 1 and IF-G 2 are slightly higher than for the listed reference values. For MREY (average % RSD: 1.14) and HREY (average % RSD: 1.48) our measured values of the BIF reference standard and the published values agree very well.

Table 4: Values of analyzed IF-G concentrations (ppm) and published IF-G values.

	LOQ	IF-G 1	% RSD		IF-G 2	Published Values		
			IF-G 1	IF-G 2		IF-G 2	[1]	[2]
Li	0.0178	0.23	3.83	0.22	2.18			
Be	0.0028	6.14	4.49	5.74	1.39			
Ti	0.274	39.3	7.47	38.1	4.48			
Co	0.0086	3.98	2.73	4.12	2.06			30.0
Ni	1.04	28.3	2.14	28.7	1.38			24
Rb	0.0069	0.312	2.59	0.314	1.99	0.5		
Sr	0.0534	3.75	2.84	3.76	2.34	4	3.61	2.90
Y	0.0304	10.1	3.12	9.96	1.54	9.1	9.14	9.3
Zr	0.0871	0.98	3.27	0.971	2.44	1.0	0.563	1.8
Nb	0.0111	0.077	4.01	0.077	3.21		0.0989	0.113
Mo	0.0252	0.39	2.60	0.342	2.55			
Cd	0.0099	0.038	6.41	0.039	3.39			0.034
Cs	0.00091	0.060	1.63	0.060	1.73	0.059		
La	0.0052	3.16	0.848	3.48	1.23	2.7	2.71	2.6
Ce	0.0132	4.65	0.961	5.14	0.841	4.0	3.9	3.8
Pr	0.0013	0.485	1.75	0.536	0.704	0.45	0.430	0.42
Nd	0.0044	1.94	1.75	2.12	0.439	1.75	1.73	1.8
Sm	0.00075	0.420	0.961	0.435	1.70	0.39	0.399	0.4
Eu	0.0012	0.375	1.28	0.387	0.808	0.37	0.362	0.38
Gd	0.00074	0.711	0.927	0.740	0.979	0.71	0.667	0.71
Tb	0.0004	0.116	1.03	0.118	0.803	0.111	0.112	0.115
Dy	0.00061	0.839	1.62	0.855	1.25	0.81	0.791	0.85
Ho	0.00082	0.210	0.982	0.209	1.25	0.203	0.207	0.215
Er	0.00022	0.661	0.674	0.661	2.46	0.64	0.619	0.68
Tm	0.00023	0.091	1.10	0.091	2.23	0.091	0.0923	0.094
Yb	0.0015	0.600	1.69	0.604	1.47	0.58	0.580	0.61
Lu	0.00027	0.094	1.58	0.094	1.39	0.091	0.0904	0.097
Hf	0.0363	0.027	3.59	0.026	3.36	0.023	0.0182	0.028
W	0.0026	0.601	1.92	0.591	1.17			243
Pb	0.222	6.00	1.53	7.14	1.86	2.5	2.52	2.50
Th	0.0047	0.035	12.0	0.041	5.62	0.05	0.0434	
U	0.0039	0.011	12.1	0.011	9.91	0.021	0.0213	0.022

*LOQ: limit of quantification

[1] Dulski (2001)

[2] Bolhar (2004)

[3] Sampaio & Enzweiler (2015)

5 Discussion

5.1 The reliability of the Tomka BIF as geochemical archive for Paleoproterozoic seawater

Pure marine Precambrian chemical sediments closely reflect the REY_{SN} distribution of modern seawater (except for Ce and Eu) and show pronounced seawater-like features, such as positive La_{SN} and Gd_{SN} anomalies, super chondritic Y/Ho ratios (i.e. positive Y_{SN} anomalies) and enrichment of heavy REY_{SN} relative to light REY_{SN} (e.g., Bau et al., 1995; Bau & Dulski, 1996b; Bolhar et al., 2004; Alexander et al., 2008; Viehmann et al., 2015). Furthermore, seawater features in BIFs decrease with increasing detritus contamination, i.e., clastic sediments that were co-sedimented with the chemical sediments (Viehmann et al., 2015). To determine pure and reliable Tomka BIF samples that represent Paleoproterozoic seawater composition, each individual sample has to be screened for impact of detrital contamination and post-depositional alteration processes.

Almost immobile elements, such as Al, Zr, Hf, and Th that are clearly associated with detrital aluminosilicates, are effective tools to evaluate the potential impact of detrital components in BIFs and other chemical sediments to resolve the origin and the behavior of chemical elements in seawater during Earth's history (e.g., Bau, 1993). For 24 of the Tomka BIF samples, the Hf and Th concentrations are below the limit of detection or concentrations are extremely low (0.005-0.088 ppm). Zirconium concentrations are slightly higher (0.13-2.84 ppm) but overall, the whole sample set of individual BIF layers can largely be described as pure, and samples with the lowest Zr concentrations are the best representatives of the Tomka seawater environment. The analyzed shale sample DM71A, on the other hand, represents the most likely detrital aluminosilicate endmember, with a Zr concentration of 116 ppm.

The usefulness of the analyzed Tomka BIF as unique geochemical archive of Archean seawater can be highlighted when compared (Fig. 14) Zr concentrations (indicator for detritus content) versus Y/Ho ratios (indicator for seawater-like REY_{SN} features) of REY_{SN} systematics from the Tomka BIF relative to Mesoarchean BIFs from the Witwatersrand Supergroup (~2.90 Ga, Viehmann et al., 2015) and Pietersburg Greenstone Belt (~2.95 Ga, Alexander et al., 2009), as well as from the Paleoproterozoic Moodies Group (~3.22 Ga, Bonnand et al., 2020) preserved in the Barberton Greenstone Belt. Other Archean BIFs have significantly elevated Zr concentrations (e.g., Moodies Group BIF up to 18.5 ppm) relative to the Tomka BIF samples (< 2.84 ppm) which also show higher super-chondritic Y/Ho ratios. The fractionation process of Y and its geochemical twin Ho is a result of particle surface complexation processes that

leads to an enrichment of Y in the seawater (e.g., Zhang et al., 1994; Bau et al., 1995), which can be observed in all samples compared here. However, the Y/Ho ratios of the Tomka BIF samples show generally higher values (41.2-66.7) than the Algoma-type Pietersburg BIF (29.5-63.5) and the detritus-contaminated Witwatersrand (29.3-36.8) and Moodies Group BIFs (20.5-41.4). The latter partly show even near-chondritic Y/Ho ratios that can be explained by the fact that the Moodies Group BIF was mostly deposited in shallow-marine settings and influenced by continental freshwater (low Y/Ho ratios, e.g., Tepe & Bau 2016), which can also result in higher detritus contamination and explains why the samples have partially higher Zr concentrations (Bonnand et al., 2020). Compared to the Algoma-type Pietersburg BIF, the Superior-type Witwatersrand BIF was also deposited in a rather shallow-water environment that was dominated by terrigenous REY input, explaining the significant detrital contamination of the samples (Viehmann et al., 2015). The Pietersburg BIF, on the other hand, was deposited in a deep-water environment partially contaminated with detrital aluminosilicates which sources include lithologies of the simatic basement (Alexander et al., 2009). Furthermore, shale sample DM71A also has a chondritic Y/Ho ratio (26.3) that can be expected, as with increasing detrital contamination (increasing Zr concentration), Y/Ho ratios (among other typical seawater-like REY_{SN} signatures) in the BIFs decrease towards a chondritic ratio of ~27 (Pack et al., 2007). Consequently, pure BIF samples representing the Paleoproterozoic seawater endmember have the lowest immobile element concentrations and highest seawater-like features such as positive Y_{SN}, Gd_{SN}, La_{SN} anomalies as well as HREY_{SN}/LREY_{SN} enrichment.

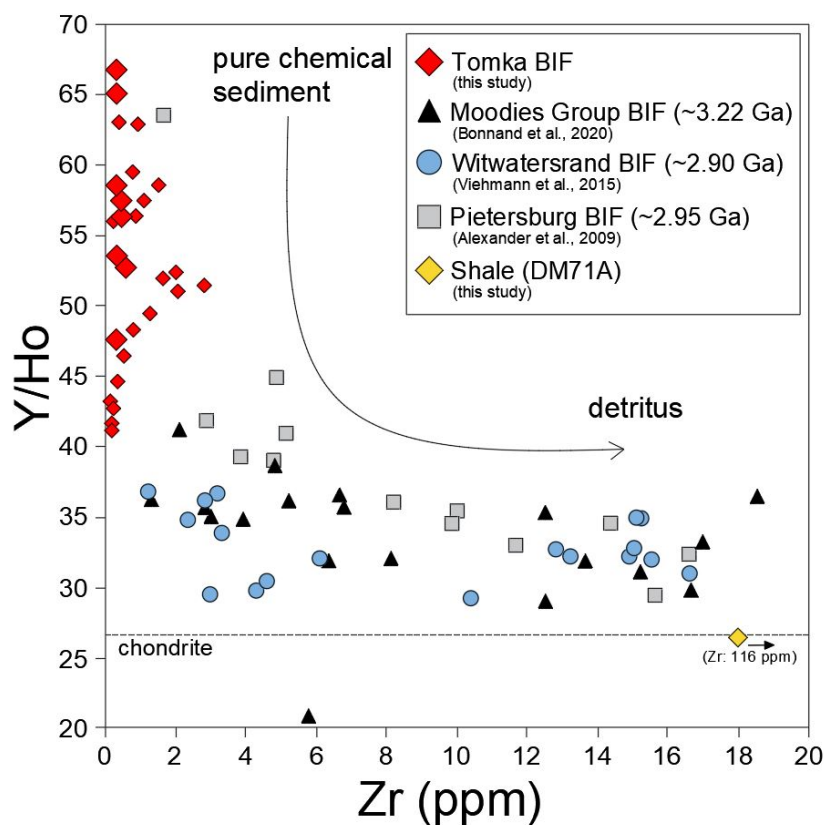


Figure 14: Graph of Y/Ho ratio vs. Zr concentration of Meso- and Paleoproterozoic BIFs. Pure chemical sediments have super-chondritic Y/Ho ratios and low concentrations of immobile elements. The Y/Ho ratios decrease towards chondritic ratios as Zr concentrations increase, indicating increasing detrital contamination.

Monitoring for the best geochemical archives representing Paleoproterozoic seawater of the Tomka BIF samples results in sample selection with the highest Y_{SN} , La_{SN} , Gd_{SN} , and $HREY_{SN}/LREY_{SN}$ enrichments (Figs. 15, 16). Only samples passing this filter process are considered as pure seawater endmembers. To emphasize the usefulness of the Tomka BIF as Paleoproterozoic seawater archives, again, the Archean Witwatersrand BIF, Pietersburg BIF, and Moodies Group BIF are used for comparison.

Positive La_{SN} and small positive Gd_{SN} anomalies in seawater are a result of surface complexation effects and ad- and desorption processes that lead to the fractionation of La and Gd in the ocean (e.g., Lee & Byrne, 1993; Bau, 1999). Especially the La_{SN} anomalies of Tomka BIF samples (< 3.43) are more prominent compared to Witwatersrand BIFs (< 1.36), Pietersburg BIF (< 2.26) and Moodies Group BIF (< 1.66) samples (Fig. 15).

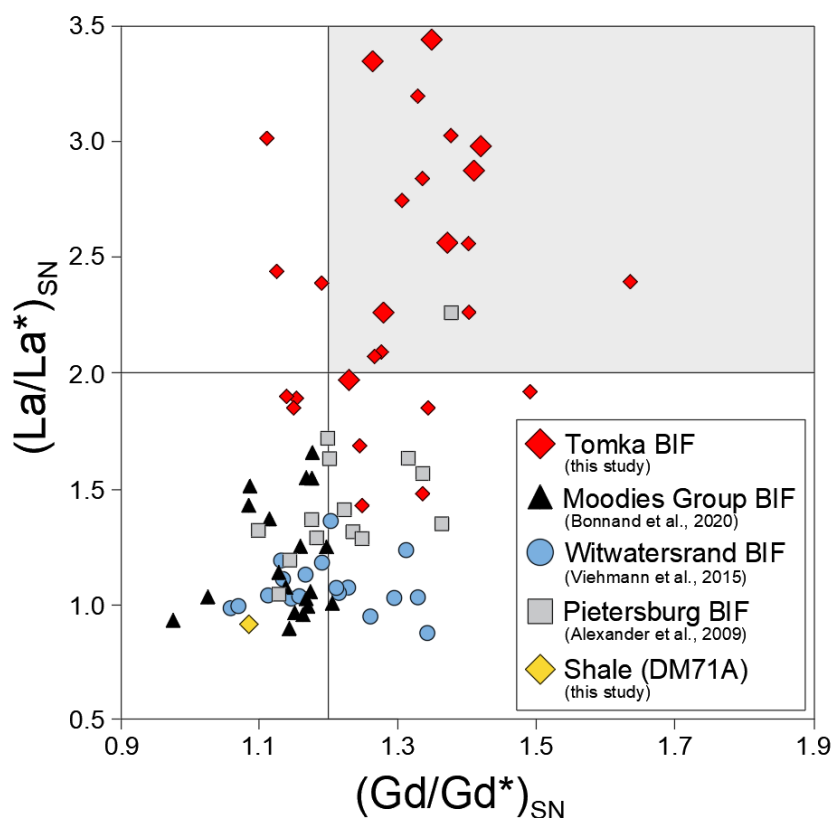


Figure 15: Graph of La_{SN}/La^*_{SN} ratio vs Gd_{SN}/Gd^*_{SN} ratio of Tomka BIF samples compared to samples of Witwatersrand BIF, Pietersburg BIF, and Moodies Group BIF. Positive La_{SN} and Gd_{SN} anomalies (grey box) can be observed in both, modern and Archean seawater. BIF samples plotting in the grey box are considered pure chemical sediments.

The reason for $HREY_{SN}$ enrichment relative to $LREY_{SN}$ in seawater includes preferred partitioning of the light REY onto particle surfaces. This is quantified by using Yb/Pr_{SN} ratios (Fig. 16) where, again, Tomka BIF samples show significantly higher ratios (< 20.4), in contrast to the Witwatersrand BIF (< 3.18), Pietersburg BIF (< 4.24), and Barberton BIF (< 1.88) samples that all plot within the same range. Note that the shale sample shows insignificant La_{SN} and Gd_{SN} anomalies and no pronounced enrichment of $HREY_{SN}$ relative to $LREY_{SN}$ with a rather flat REY_{SN} pattern (Fig. 16).

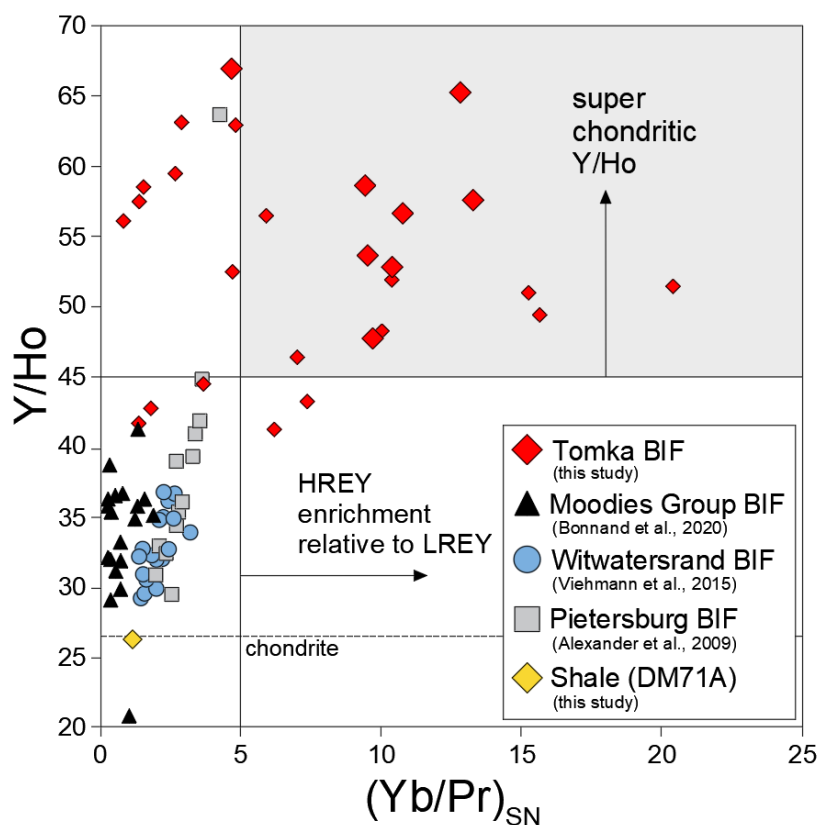


Figure 16: Graph of Y/Ho ratio vs. Yb_{SN}/Pr_{SN} ratio of Tomka BIF samples compared to samples of Witwatersrand BIF, Pietersburg BIF, and Moodies Group BIF. Pure chemical sediments (grey box) show super-chondritic Y/Ho ratio and strong enrichment of $HREY_{SN}$ relative to $LREY_{SN}$. The chondritic Y/Ho ratio was published in Pack et al. (2007).

The comparison with these Meso- and Paleoproterozoic BIFs clearly support the reliability of Tomka BIF samples as archives for ancient seawater with only little or insignificant detrital contamination and pronounced seawater-like features. Ultimately, the eight best-preserved Tomka BIF samples passing the monitoring process of the most pronounced seawater-like features, i.e., serve as the best geochemical archive of the composition of Paleoproterozoic seawater are considered as the Paleoproterozoic seawater endmember that most closely represents the water composition from which the Tomka BIF precipitated (Fig. 17).

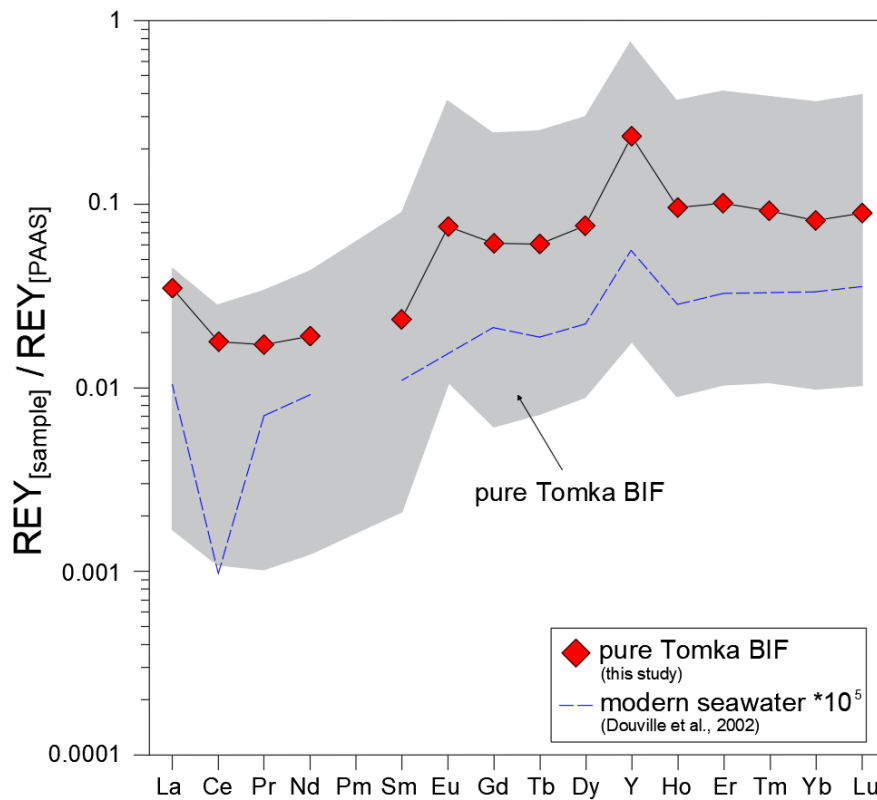


Figure 17: The REY_{SN} patterns of the eight best preserved (i.e., pure) Tomka BIF samples compared to modern seawater.

5.2 The depositional environment of the Tomka BIF

The REY_{SN} patterns of the most reliable seawater endmembers of the Tomka BIFs are consistent and sub-parallel (with the exception of redox-sensitive Ce and Eu) to representative pure BIF samples from the Eoarchean Isua Greenstone Belt (Friend et al., 2008), the Mesoarchean Pietersburg Greenstone Belt (Alexander et al., 2009), the Neoproterozoic Kuruman BIF (Bau & Dulski, 1996b), the Neoproterozoic Urucum BIF (Viehmann et al., 2016), and modern seawater (Fig. 18).

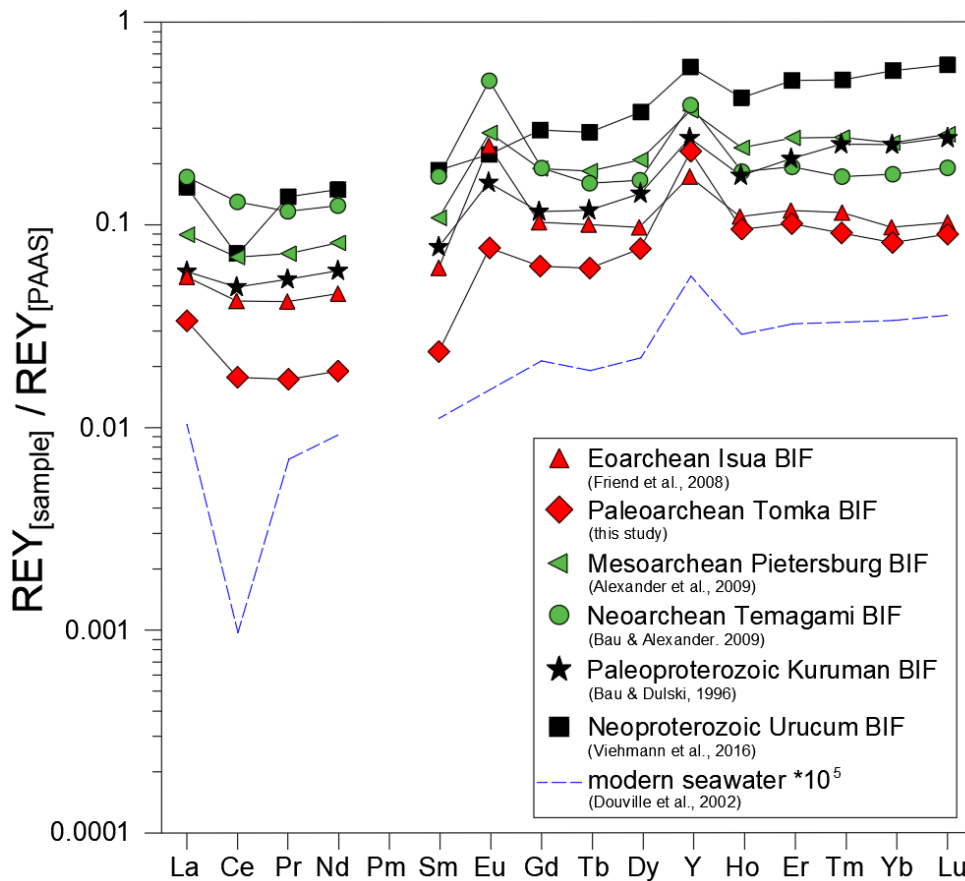


Figure 18: REY_{SN} patterns of a representative Tomka BIF sample compared to representative pure BIF samples from the Eoarchean Isua Greenstone Belt, the Mesoarchean Pietersburg Greenstone Belt, the Neoarchean Temagami Greenstone Belt, the Paleoproterozoic Kuruman BIF, the Neoproterozoic Urucum BIF, and modern seawater.

Chemical sediments such as BIFs incorporate the REY composition of the ambient fluids they precipitated from (e.g., Bau & Dulski, 1996b). The similarity of REY_{SN} patterns of the Tomka BIF compared to REY_{SN} patterns of modern seawater provide evidence that the Tomka BIF precipitated in an environment connected to the open ocean (Fig. 19). It is not very likely that other fluids, besides a high-temperature hydrothermal input reflected by positive Eu_{SN} anomalies, such as river water or alkaline systems, significantly dominated the seawater chemistry in the Tomka depositional environment. The REY_{SN} patterns of one representative Tomka BIF sample differ from those of a high-temperature hydrothermal fluid (Bau & Dulski, 1999), the alkaline (partly evaporitic) Lake Van in Turkey (Möller & Bau, 1993), a hypersaline brine (Censi et al., 2017), river water from Markarfljót River in Iceland (Tepe & Bau, 2016) and freshwater from Lake Paranoá in Brasil (Fig. 19, Merschel et al., 2015). No similarities of the REY_{SN} patterns can be observed between the Tomka BIF sample and the alkaline Lake Van that shows a strong Ce_{SN} anomaly and an even stronger HREY_{SN} to LREY_{SN} increase. This is a result of higher order carbonate-complexation leading to more pronounced LREY_{SN}/HREY_{SN}

fractionation in the alkaline lake in contrast to seawater (Möller & Bau, 1993). The hypersaline brine fluid (slight enrichment of HREY_{SN} relative to LREY_{SN}), the river water (depletion of the LREY_{SN} and HREY_{SN} relative to the MREY_{SN}), and the water of Lake Paranoá (positive Ce_{SN} anomaly, depletion of LREY_{SN} relative to HREY_{SN} and anthropogenic Gd_{SN} anomaly) show a rather flat REY_{SN} pattern and do not have the typical REY_{SN} pattern of the Tomka BIF.

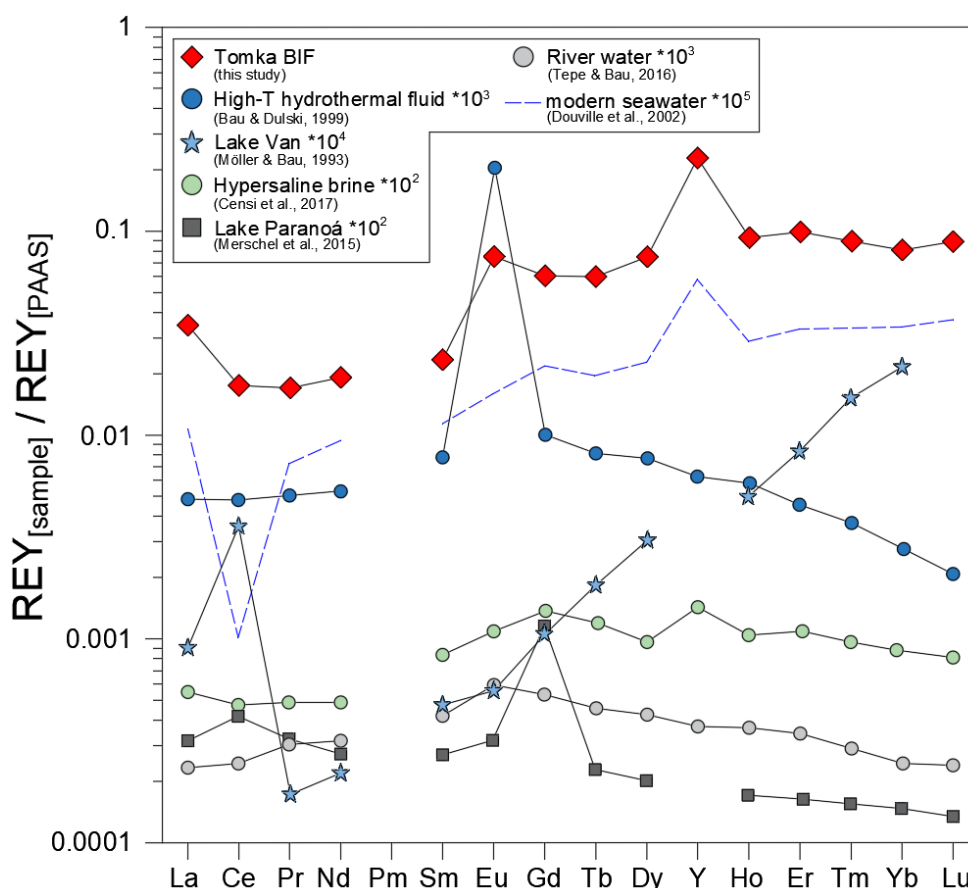


Figure 19: Comparison of the REY_{SN} patterns of a Tomka BIF sample and a high-temperature hydrothermal fluid, the alkaline (partly evaporitic) Lake Van in Turkey, a hypersaline brine, river water from Markarfljót River in Iceland, water from Lake Paranoá in Brasil and modern seawater.

Cerium and Eu show considerable changes in the REY_{SN} signatures of marine chemical sediments, reflecting the redox-sensitive nature of these elements throughout Earth's history (Fig. 18). The absence of significant negative Ce_{SN} anomalies in the Tomka BIF samples, such as most Archean and early Paleoproterozoic BIFs, indicates reducing seawater conditions with respect to the $\text{Ce}^{3+}/\text{Ce}^{4+}$ redox couple (Bau & Dulski, 1996b; Alexander et al., 2008; Planavsky et al., 2010; Viehmann et al., 2015). In general, oxygenated modern marine environments show a strongly negative Ce_{SN} anomaly, as the oxidation of Ce^{3+} to Ce^{4+} on particle surfaces such as of Mn(IV)- Fe(III)-oxyhydroxides, clay particles and organic matter substantially reduces Ce

solubility resulting in the lack of Ce desorption processes from these surfaces (Slack et al., 2007; Bau & Koschinsky, 2009; and references therein). This leads to the characteristic negative Ce_{SN} anomaly in the REY_{SN} patterns of modern seawater, as this process leaves the residual seawater depleted in Ce (Bau & Koschinsky, 2009). This suggests that the ambient atmosphere-hydrosphere system in the Tomka depositional area was – similar to most of the other Archean and early Paleoproterozoic marine environments – relatively anoxic, or at least below the Eh of the Ce^{4+}/Ce^{3+} redox couple and does not show evidence for a local trace of oxygen (Anbar et al., 2007) as was observed, for example, in the 2.9 Ga old Steep Rock environment (Fralick & Riding, 2015). Furthermore, higher atmospheric-hydrospheric oxygen levels, for example, explain the negative Ce_{SN} anomaly of the Neoproterozoic Urucum BIF (Fig. 18) that were deposited in an oxic marine environment and consequently the similarity to REY_{SN} patterns with well-oxidized modern seawater.

Moreover, most Archean BIFs are characterized by strong positive Eu_{SN} and Eu_{CN} anomalies (Fig. 18), indicating that these marine chemical sediments precipitated from seawater that was influenced by > 200 °C hydrothermal fluids (Fig. 19, e.g., Bau, 1991; Danielson et al., 1992; Bau & Dulski, 1996b; Konhauser et al., 2017). In hydrothermal systems, Europium³⁺ is readily reduced to Eu^{2+} which is more stable under these hot, slightly acidic, and reducing conditions above 200-250°C. Furthermore, the REY^{3+} are preferentially incorporated into alteration minerals (e.g., chlorite) relative to Eu^{2+} resulting in an excessive amount of Eu^{2+} in hydrothermal fluids. However, Eu^{2+} is immediately oxidized to Eu^{3+} in close vicinity to the hydrothermal vent site, as the Eu^{3+}/Eu^{2+} redox potential is highly temperature dependent (Bau, 1991; Bau & Dulski, 1999; Douville et al., 1999; Viehmann, et al., 2015). This is in strong contrast to modern seawater showing no Eu_{SN} and Eu_{CN} anomalies and marine chemical sediments deposited in the Proterozoic showing less-pronounced anomalies relative to marine chemical sediments in the Archean (Viehmann et al., 2015). This is because modern seawater is oxic and at black smoker sites the hydrothermal fluids are oxidized immediately and hydrothermal REY are immediately adsorbed onto at surfaces of Mn(IV)- Fe(III)-oxyhydroxides and removed from the aquatic system. Consequently, today these hydrothermal systems rather act as a sink of Eu and other REY (German et al., 1990) than as a source. In the Archan, on the other hand, the seawater was largely anoxic and ferruginous, not allowing iron minerals and other phases to oxidize and scavenge the REYs on their surfaces, resulting in a long transport of these elements even in shallow-water environments. Thus, in contrast to modern oceans, hydrothermal fluids represent an important source of REY and other trace elements into Archean seawater (Viehmann et al., 2015).

All samples of the Tomka BIF have positive Eu_{SN} and Eu_{CN} anomalies, corroborating that the marine environment when the chemical sediment was deposited was anoxic and affected from black-smoker-type high-temperature hydrothermal REY contributions.

5.3 Europium anomalies of Tomka BIF

5.3.1 Europium evolution curve as a qualitative dating tool

The presence or absence of Eu anomalies in chondrite-normalized (subscript CN) REY patterns of BIFs has been used as indirect dating tool to distinguish between Archean and Post-Archean marine chemical sediments. Positive Eu_{CN} anomalies are typically developed in Archean BIFs but only episodically observed throughout the Proterozoic (e.g., Dymek & Klein, 1988; Danielson et al., 1992; Viehmann et al., 2015; Konhauser et al., 2017). Positive Eu_{CN} anomalies indicate a strong contribution of high-temperature hydrothermal REY (with an anomalous enrichment of Eu) to the Archean seawater and a rather long residence time of REY including Eu. This was only possible because of the anoxic state of the Archean seawater, because even under slightly more oxic conditions, the REY would be scavenged and removed by Fe(III)-oxyhydroxides in close proximity to the hydrothermal systems as observed in modern seawater close to black smoker sites (e.g., German et al., 1990; Bau & Dulski, 1999). A diagram of Eu_{CN}/Eu^*_{CN} ratios vs depositional age (Fig. 20) shows 750 samples of predominantly pure BIFs, i.e. reliable archives of ambient seawater at the time of their deposition. The Eu_{CN}/Eu^*_{CN} evolution curve starts in the Eoarchean (~3.8 Ga) with BIFs from the Nuvvuagittuq (e.g., Mloszewska et al., 2012) and Isua Greenstone Belt (e.g., Appel, 1983) showing Eu_{CN}/Eu^*_{CN} ratios up to 2.75 followed by a decrease until the Neoarchean. A significant rise of positive Eu_{CN} anomalies occurs between ~2.7 to 2.6 Ga with BIFs of the Kushtagi schist belt showing Eu_{CN}/Eu^*_{CN} ratios up to 4.56 (Khan et al., 1996). This peak vanishes from 2.5 Ga and from this point in time positive Eu_{CN} anomalies in marine chemical sediments do not exist in the Proterozoic, with two exceptions around 2.2 and 1.9 Ga. In the rock record, BIFs re-appear a last time in the Neoproterozoic, when the occurrence is related to “Snowball Earth” (see chapter 1.2.1) conditions, with Eu_{CN}/Eu^*_{CN} ratios only reaching top ratios of 1.00 in the BIF of Arroyo del Soldado Group 570 Ma ago (Frei et al., 2009b), suggesting that contributions of high-temperature hydrothermal systems were insignificant for the marine chemistry in the Neoproterozoic.

Paleoarchean Eu_{CN} data from BIFs in the time frame around 3.5 Ga, however, are lacking to date and the Tomka BIFs studied here indicate a unique time window to better understand Eu

systematics on early Earth. The $\text{Eu}_{\text{CN}}/\text{Eu}^*_{\text{CN}}$ ratios of the Tomka BIF do not follow the estimated global seawater Eu curve by Viehmann et al. (2015), but show only $\text{Eu}_{\text{CN}}/\text{Eu}^*_{\text{CN}}$ ratios up to 2.00, i.e., significantly lower ratios than expected from the published curve. The average of $\text{Eu}_{\text{CN}}/\text{Eu}^*_{\text{CN}}$ ratio of pure Tomka BIF samples is 1.55.

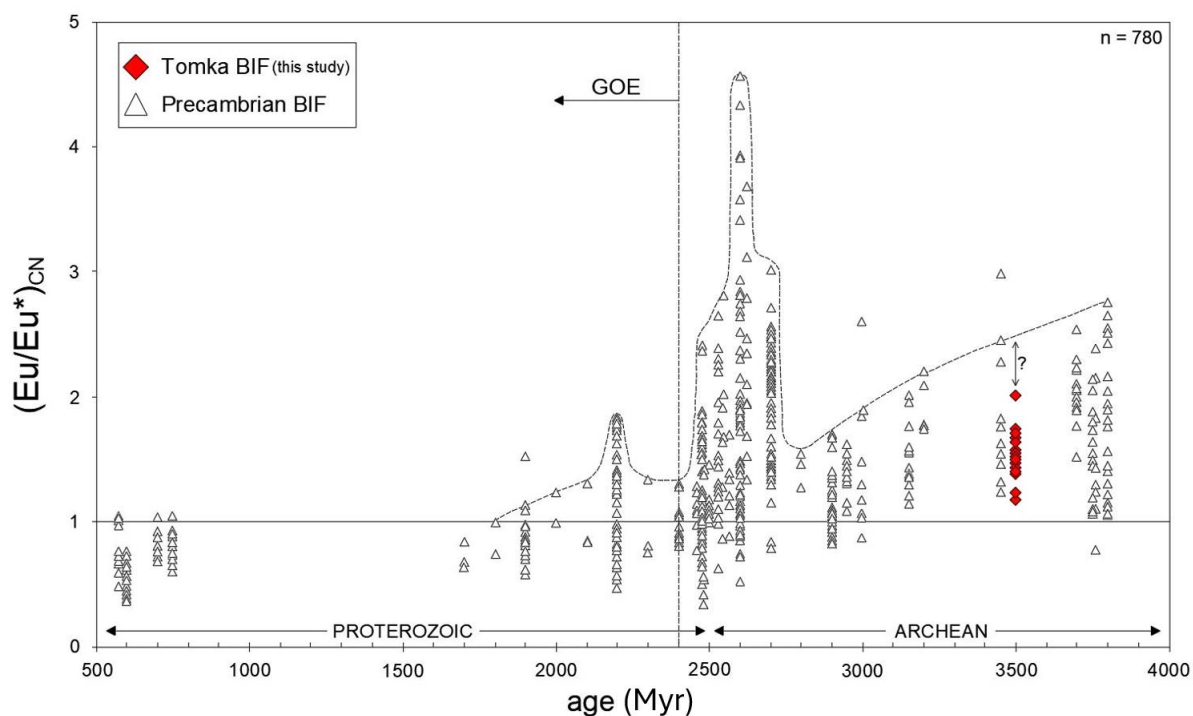


Figure 20: The Precambrian $\text{Eu}_{\text{CN}}/\text{Eu}^*_{\text{CN}}$ evolution curve of pure BIFs (i.e., reliable seawater archives). Eu_{CN} anomalies are strongly pronounced in the Eoarchean followed by a decline until the Neoarchean and a distinct peak at around ~2.7 Ga, which vanished until 2.5 Ga and the GOE. In the Proterozoic, positive Eu_{CN} anomalies are only episodically observed at 2.2 and 1.9 Ga (modified from Viehmann et al., 2015). GOE: Great Oxidation Event.

5.3.2 Explanations for Eu_{CN} systematics of Tomka BIF

The reason for increased $\text{Eu}_{\text{CN}}/\text{Eu}^*_{\text{CN}}$ ratios of Archean BIFs is a strong contribution of black smoker-type high-temperature hydrothermal REY to seawater from which the chemical sediments precipitated. It generally appears that the influence of hydrothermal REY was more pronounced in the Eoarchean and Neoarchean relative to the Meso- and Paleoarchean based on the $\text{Eu}_{\text{CN}}/\text{Eu}^*_{\text{CN}}$ seawater curve. The values of Eu_{CN} anomalies of Tomka BIF samples are distinctly lower and do not follow the $\text{Eu}_{\text{CN}}/\text{Eu}^*_{\text{CN}}$ seawater evolution curve which might indicate a less pronounced flux of high-temperature hydrothermal REY to the Tomka seawater environment compared to other Archean environments. A reason for that might include a lower upper mantle temperature and comparably less magmatic activity underneath the Singhbhum Craton around 3.5 Ga.

Subsequently, it could be deduced that the $\text{Eu}_{\text{CN}}/\text{Eu}^*_{\text{CN}}$ ratios of the oldest BIFs (e.g., from the Isua Greenstone Belt) reflect hotter upper mantle conditions corroborating estimated mantle temperatures from Herzberg et al. (2010) and consequently increased high-temperature hydrothermal REY input into Eoarchean seawater. The following steady decrease of the $\text{Eu}_{\text{CN}}/\text{Eu}^*_{\text{CN}}$ ratios in the Paleo- and Mesoarchean might indicate a general cooling of the mantle with weaker high-temperature hydrothermal fluxes and possibly a thicker lithosphere with less pathways for mantle-derived fluids into ancient seawater (cf. Korenaga, 2006; Bedard et al., 2018). Furthermore, previous studies (e.g., Isley & Abbott, 1999; Bekker et al., 2010) proposed a connection between enhanced BIF deposition and (ultra)mafic igneous activity. In the ocean intense mafic mantle plume events erupt great volumes of Fe-rich tholeiitic basalts. This process is associated with increased heat flow and leads to the formation of oceanic crust which results in elevated high-temperature hydrothermal activity associated with a higher flux of elements, such as Fe and REY (e.g., Isley & Abbott, 1999; Bekker et al., 2010; Lowenstein et al., 2014; Viehmann et al., 2015). Thus, there might be a correlation between periods of intense mantle plume volcanism and sedimentation of BIFs. To connect this with the lower $\text{Eu}_{\text{CN}}/\text{Eu}^*_{\text{CN}}$ ratios of Tomka BIF, it could be concluded that there was no or little mantle plume volcanism with less spreading ridges in the proximal surrounding area and, consequently, a less pronounced high-temperature hydrothermal activity ca. 3.5 Ga ago. However, low mantle temperatures are contradicted by the appearance of komatiitic basalts in the stratigraphy of the Daitari Greenstone Belt (Fig. 10). Both the Kalisagar Formation, the stratigraphically lowest unit of the volcano-sedimentary package of the DGB, and the Talangi Formation directly overlying the Tomka Formation comprise komatiitic basalts providing evidence for magmatic rocks that were formed under high mantle temperatures. Komatiites are rare igneous rocks mainly of Archean age whose origin is controversial, but they might be attributed to mantle plume activities with temperature far hotter than magmas erupting today (e.g., Arndt et al., 2008). Moreover, Isley and Abbot (1999) described four proxies of mantle plume activity including the presence of komatiites. However, it is debatable if the Tomka BIF was deposited in an episode of no or very little submarine igneous activity. In the Singhbhum Craton, successions like the DGB are referred to as the Badampahar Group (e.g., Iyengar & Murthy, 1982; Jena & Behra, 1998; Hofmann et al., 2022), which is a typical Paleoarchean greenstone assemblage of submarine volcanic rocks and chemical and silicified sedimentary rocks (Fig. 10). As described in Hofmann et al. (2022) the early phase of the Singhbhum Craton, which also includes the deposition of marine chemical sediments, was marked by mafic/ultramafic submarine volcanism and TTG plutonism forming proto-cratonic crust (Fig. 21). However, the abundance

of komatiitic basalts in the stratigraphy of the DGB does not necessarily mean that these rocks were formed in the upper mantle as a high temperature is an important feature of the formation of komatiites. The source of Archean komatiites is unclear, but deep mantle plumes might transport hot, buoyant material upwards rising from deeper in the mantle – perhaps even from the core-mantle boundary (Arndt et al., 2008). A scenario including a hot deeper mantle reflected by the appearance of komatiites, and a cooler upper mantle with reduced high-temperature hydrothermal influence reflected by less pronounced $\text{Eu}_{\text{CN}}/\text{Eu}^*_{\text{CN}}$ ratios in the BIF in the Tomka depositional environment around 3.5 Ga, could be possible.

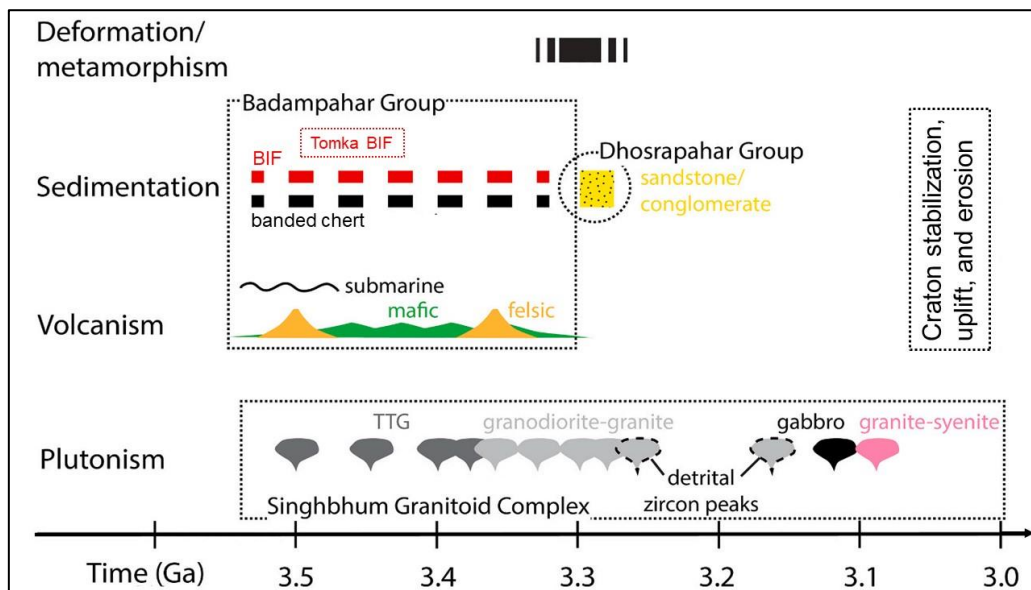


Figure 21: Time chart of early magmatic, depositional, and structural events in the Singhbhum Craton with focus on the Badampahar Group including the Tomka BIF (modified from Hofmann et al., 2022).

5.3.3 The link of Eu_{CN} anomalies in BIFs to the geodynamic evolution of the early Earth

There has been no general agreement to the suggestion that early Earth started with stagnant lid convection and mafic crust with a later onset of global plate tectonics in the Mid-Archean followed by formation of felsic continental crust (e.g., O'Neill et al., 2007; Shirey & Richardson, 2011; Dhuime et al., 2012; Van Hunen & Moyen, 2012; Piper, 2013; Debaille et al., 2013; Moore & Webb, 2013; O'Neill & Debaille, 2014; Tang et al., 2016; Cawood et al., 2018; Smit et al., 2019). However, the early Archean tectonic setting is a very controversial issue with some authors favoring the onset of plate tectonics already in the Hadean (e.g., Hopkins et al., 2008; Rosas & Korenaga, 2018; Hyung et al., 2020), while others prefer the onset of modern-style plate tectonics as late as the Neoproterozoic (e.g., Stern, 2005).

In contrast to early Earth, modern plate tectonics is defined by division of the lithosphere into rigid plate mosaics, which are in relative motion with respect to each other, with an underlying convecting mantle (Moresi & Solomatov, 1998; Tackley, 1998). Plate motion is driven by potential energy at sites of seafloor spreading and by slab pull forces at sites of subduction of oceanic lithosphere (Cawood et al., 2006; Stern, 2005).

The pre-plate tectonic regime, on the other hand, is characterized by rather poor mobility with a fixed or only episodically mobile lithosphere, no convergence and long-term plutonism, which could be described with a global stagnant lid regime or single-lid regime (Korenaga, 2006, 2013; Cawood et al, 2018). Based on numerical modelling it was suggested that a “real” subduction (sinking of older and cooler oceanic crust into the mantle) was not possible as the high mantle potential temperature, in combination with smaller convection cells (Fig. 22), would inhibit the formation of a mantle keel in the Paleoarchean (> 2.3 Ga, Trucotte and Schubert, 2002; Johnson et al., 2014, 2017; Cawood et al., 2018; Mitra et al., 2022). Furthermore, prior to 3.2 Ga the pre-plate tectonic regime involved magmatism associated with TTGs and greenstone belts.

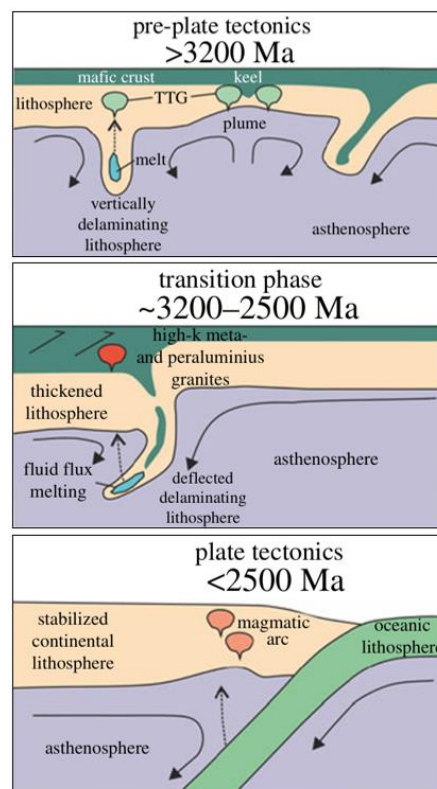


Figure 22: Schematic evolution of plate tectonics and the lithosphere. Early Earth (> 3.2 Ga) involves a non-plate tectonic regime including magmatism associated with TTGs and greenstone belts. Plate tectonics is believed to have been established after 2.5 Ga and is associated with large proportions of mantle convection. Between these two tectonic regimes is a transitional phase that includes the stabilization of the lithosphere and the differentiation into continental and oceanic type (Cawood et al. 2018).

Applying this model to the Tomka BIF around 3.5 Ga, the decreased high-temperature hydrothermal flux into the Tomka marine environment could be explained with a thick Paleoproterozoic (oceanic) lithosphere, that was too buoyant to subduct (e.g., Davies 1992), and the absence of modern-style subduction zones limited the formation of spreading ridges and led to reduced high-temperature hydrothermal venting into seawater and the BIF depositional environment.

However, if this relationship between $\text{Eu}_{\text{CN}}/\text{Eu}^*_{\text{CN}}$ anomalies in BIFs and this geodynamic model is viable is still questionable. Capitanio et al. (2019), for instance, argument against a stagnant lid regime in the Archean as this geodynamic model may have only existed for a short period (< 500 Ma) in the Hadean; a lid-and plate tectonic regime may have been established quite rapidly in Earth's history. This might be corroborated by zircons indicating crust-forming tectonic processes as old as 4.4 Ga (e.g., Harrison et al., 2005).

In conclusion, the Tomka BIF data cannot be unambiguously assigned to a specific geodynamic model; however, with additional data of BIFs of similar age there is a great chance that Eu_{CN} anomalies can be linked to early geodynamic processes in further studies. Furthermore, because of the limited rock record in the early Archean, BIFs could provide another angle on geotectonic models of the Precambrian and could possibly be used as a unique archive to indirectly estimate mantle temperatures and processes related to it from a seawater perspective.

6 Conclusions

The Datari Greenstone Belt in the Singhbhum Craton hosts the ca. 3.5-3.3 Ga Banded Iron Formation preserved within the Tomka Formation (Jodder et al. 2023), representing one of the oldest reliable geochemical archives of ancient seawater. Trace element concentrations of individual chert-, Fe- and mixed Fe- and chert-microbands show shale-normalized REY signatures (with the exception of redox sensitive elements) similar to modern seawater. The Tomka BIF samples show typical seawater-like REY_{SN} characteristics of Archean seawater such as a lack of Ce_{SN} anomalies, depletion of LREY_{SN} relative to HREY_{SN} , positive La_{SN} , Gd_{SN} and Eu_{SN} anomalies and super-chondritic Y/Ho ratios. The lack of Ce_{SN} anomalies indicate anoxic conditions at the time of the BIF deposition and the presence of Eu_{SN} and Eu_{CN} anomalies reveal the influence of REY to ambient seawater from high-temperature hydrothermal systems. In addition, it is not very likely that other fluids, besides a high-temperature hydrothermal input, such as river water or alkaline systems, significantly

influenced the seawater chemistry of the Tomka depositional environment. The Tomka BIF samples show little detrital contamination with low contents of almost immobile elements such as Al, Hf, Th, and Zr. The comparison of typical seawater-like REY_{SN} characteristics of Tomka BIF samples with BIF samples of the Paleoarchean Moodies Group (~3.22 Ga) and Mesoarchean Witwatersrand Supergroup (~2.90 Ga) and Pietersburg Greenstone Belt (~2.95 Ga) confirms the reliability as an excellent archive of Archean seawater.

Especially Archean BIF samples are characterized by positive Eu_{CN} anomalies and REY data of pure BIFs show strong positive Eu_{CN}/Eu*_{CN} ratios in the Eoarchean, followed by decreasing ratios until the Neoarchean (Viehmann et al., 2015). However, Eu data of the Tomka BIF samples do not follow the global seawater Eu curve, but show significantly lower Eu_{CN}/Eu*_{CN} values than expected. This might indicate a general cooling of the mantle with less pronounced fluxes of high-temperature hydrothermal REY to the Daitari ocean ca. 3.5 Ga ago. Furthermore, it could be concluded that there was no or little mantle plume volcanism with less spreading ridges in the proximal surrounding of the Tomka BIF depositional environment. However, this could be contradicted by the presence of komatiitic basalts in the stratigraphy of the Daitari Greenstone Belt, but it does not necessarily mean that komatiites were formed in the upper mantle. A scenario with cooler upper mantle temperatures and reduced high-temperature hydrothermal fluxes reflected by the lower Eu_{CN}/Eu*_{CN} ratios of Tomka BIF samples and a hot deep mantle reflected by komatiitic basalts could be possible.

We also tried to link Eu_{CN} anomalies in the Tomka BIF to the geodynamic evolution of early Earth where stagnant lid tectonics might be a possible regime prior to modern plate tectonics. A thicker lithosphere, which was too buoyant to subduct, and the absence of subduction zones leading to reduced high-temperature hydrothermal fluxes in the Tomka depositional environment could be a possible scenario ca. 3.5 Ga.

References

- Acharyya, S. K. (1993). Greenstones from Singhbhum craton, their Archean character, oceanic crustal affinity and tectonics. *Proceedings of the National Academy Sciences of India, Section. A.*, 63, 211–222.
- Adhikari, A., Mukherjee, S., & Vadlamani, R. (2021). A plume - mantle interaction model for the petrogenesis of komatiite - komatiitic basalt - basalt - basaltic andesite volcanism from the Paleoproterozoic (3.57–3.31 Ga) Iron Ore Group greenstone belts, Singhbhum craton, India: Constraints from trace element geochemistry and Sm–Nd geochronology. *Lithos*, 398–399, 106315.
- Aftabi, A., Atapour, H., Mohseni, S., & Babaki, A. (2021). Geochemical discrimination among different types of banded iron formations (BIFs): A comparative review. *Ore Geology Reviews*, 136, 104244.
- Alexander, B. W., Bau, M., & Andersson, P. (2009). Neodymium isotopes in Archean seawater and implications for the marine Nd cycle in Earth's early oceans. *Earth and Planetary Science Letters*, 283(1–4), 144–155.
- Alexander, B. W., Bau, M., Andersson, P., & Dulski, P. (2008). Continentally-derived solutes in shallow Archean seawater: Rare earth element and Nd isotope evidence in iron formation from the 2.9 Ga Pongola Supergroup, South Africa. *Geochimica et Cosmochimica Acta*, 72(2), 378–394.
- Alibo, D. S., & Nozaki, Y. (1999). Rare earth elements in seawater: Particle association, shale-normalization, and Ce oxidation. *Geochimica et Cosmochimica Acta*, 63(3–4), 363–372.
- Anbar, A. D., Duan, Y., Lyons, T. W., Arnold, G. L., Kendall, B., Creaser, R. A., Kaufman, A. J., Gordon, G. W., Scott, C., & Garvin, J. (2007). A whiff of oxygen before the Great Oxidation Event? *Science*, 317(5846), 1903–1906.
- Anders, E., & Grevesse, N. (1989). Abundances of the elements: Meteoritic and solar. *Geochimica et Cosmochimica Acta*, 53(1), 197–214.
- Anhaeusser, C. R. (2014). Archean greenstone belts and associated granitic rocks; a review. *Journal of African Earth Sciences*, 100, 684–732.
- Appel, P. W. U. (1983). Rare earth elements in the early Archean Isua iron-formation, West Greenland. *Precambrian Research*, 20(2–4), 243–258.
- Appel, P. W. U. (1980). On the early Archean Isua iron-formation, West Greenland. *Precambrian Research*, 11, 73–87.
- Arndt, N. T., Nelson, D. R., Compston, W., Trendall, A. F., & Thorne, A. M. (1991). The age of the Fortescue Group, Hamersley Basin, Western Australia, from ion microprobe zircon U-Pb results. *Australian Journal of Earth Sciences*, 38(3), 261–281.
- Arndt, N., Leshner, C. M. & Barnes, S. J. (2008). *Komatiite*. Cambridge: Cambridge University Press.
- Bau, M. (1991). Rare-earth element mobility during hydrothermal and metamorphic fluid-rock interaction and the significance of the oxidation state of europium. *Chemical Geology*, 93(3), 219–230.
- Bau, M. (1993). Effects of syn- and post-depositional processes on the rare-earth element distribution in Precambrian iron-formations. *European Journal of Mineralogy*, 5(2), 257–268.
- Bau, M. (1996). Controls on the fractionation of isovalent trace elements in magmatic and aqueous systems; evidence from Y/Ho, Zr/Hf, and lanthanide tetrad effect. *Contributions to Mineralogy and Petrology*, 123(3), 323–333.
- Bau, M. (1999). Scavenging of dissolved yttrium and rare earths by precipitating iron oxyhydroxide; experimental evidence for Ce oxidation, Y-Ho fractionation, and lanthanide tetrad effect. *Geochimica et Cosmochimica Acta*, 63(1), 67–77.
- Bau, M., & Alexander, B. W. (2009). Distribution of high field strength elements (Y, Zr, REE, Hf, Ta, Th, U) in adjacent magnetite and chert bands and in reference standards FeR-3 and FeR-4 from the Temagami iron-formation, Canada, and the redox level of the Neoproterozoic ocean. *Precambrian Research*, 174(3–4), 337–346.
- Bau, M., & Dulski, P. (1996a). Anthropogenic origin of positive gadolinium anomalies in river waters. *Earth and Planetary Science Letters*, 143(1–4), 245–255.

- Bau, M., & Dulski, P. (1996b). Distribution of yttrium and rare-earth elements in the Penge and Kuruman iron-formations, Transvaal Supergroup, South Africa. *Precambrian Research*, 79, 37–55.
- Bau, M., & Dulski, P. (1999). Comparing yttrium and rare earths in hydrothermal fluids from the Mid-Atlantic Ridge: implications for Y and REE behaviour during near-vent mixing and for the Y/Ho ratio of Proterozoic seawater. *Chemical Geology*, 155(1-2), 77-90.
- Bau, M., Dulski, P., & Möller, P. (1995). Yttrium and Holmium in South-Pacific Seawater: Vertical Distribution and Possible Fractionation Mechanisms. *Chemie der Erde - Geochemistry*, 55, 1–15.
- Bau, M., & Koschinsky, A. (2009). Oxidative scavenging of cerium on hydrous Fe oxide; Evidence from the distribution of rare earth elements and yttrium between Fe oxides and Mn oxides in hydrogenetic ferromanganese crusts. *Geochemical Journal*, 43(1), 37-47.
- Bau, M., Koschinsky, A., Dulski, P., & Hein, J. R. (1996). Comparison of the partitioning behaviours of yttrium, rare earth elements, and titanium between hydrogenetic marine ferromanganese crusts and seawater. *Geochimica et Cosmochimica Acta*, 60(10), 1709–1725.
- Bau, M., & Möller, P. (1993). Rare earth element systematics of the chemically precipitated component in early precambrian iron formations and the evolution of the terrestrial atmosphere-hydrosphere-lithosphere system. *Geochimica et Cosmochimica Acta*, 57(10), 2239–2249.
- Bedard, J. H., Roberts, N. M. W., & O'Neill, C. (2018). Stagnant lids and mantle overturns; implications for Archaean tectonics, magmagenesis, crustal growth, mantle evolution, and the start of plate tectonics. *Geoscience Frontiers*, 9(1), 19–49.
- Bekker, A., Holland, H. D., Wang, P.-L., Rumble, D., Stein, H. J., Hannah, J. L., Coetzee, L. L., & Beukes, N. J. (2004). Dating the rise of atmospheric oxygen. *Nature*, 427(6970), 117–120.
- Bekker, A., & Kaufman, A. J. (2007). Oxidative forcing of global climate change: A biogeochemical record across the oldest Paleoproterozoic ice age in North America. *Earth and Planetary Science Letters*, 258(3–4), 486–499.
- Bekker, A., Planavsky, N. J., Krapež, B., Rasmussen, B., Hofmann, A., Slack, J. F., Rouxel, O. J., & Konhauser, K. O. (2013). Iron Formations: Their Origins and Implications for Ancient Seawater Chemistry. In H. Holland and K. Turekian (Ed.), *Treatise on Geochemistry* (Vol. 9), pp. 561-628. Netherlands: Elsevier.
- Bekker, A., Slack, J. F., Planavsky, N., Krapež, B., Hofmann, A., Konhauser, K. O., & Rouxel, O. J. (2010). Iron Formation: The Sedimentary Product of a Complex Interplay among Mantle, Tectonic, Oceanic, and Biospheric Processes. *Economic Geology*, 105(3), 467-509.
- Bengtson, S., & Yue, Z. (1992). Predatorial borings in late Precambrian mineralized exoskeletons. *Science*, 257(5068), 367–369.
- Berner, R. A. (2004). A model for calcium, magnesium and sulfate in seawater over Phanerozoic time. *American Journal of Science*, 304(5), 438–453.
- Binnewies, M., Finze, M., Jäckel, M., Schmidt, P., Willner, H., & Rayner-Canham, G. (2016). *Allgemeine und Anorganische Chemie* (3rd ed.). Springer Berlin Heidelberg.
- Blankenship, R. E., & Hartman, H. (1998). The origin and evolution of oxygenic photosynthesis. *Trends in Biochemical Sciences* (Amsterdam. Regular Ed.), 23(3), 94–97.
- Bolhar, R., Kamber, B. S., Moorbath, S., Fedo, C. M., & Whitehouse, M. J. (2004). Characterisation of early Archaean chemical sediments by trace element signatures. *Earth and Planetary Science Letters*, 222(1), 43–60.
- Bonnand, P., Lalonde, S. V., Boyet, M., Heubeck, C., Homann, M., Nonnotte, P., Foster, I., Konhauser, K. O., & Köhler, I. (2020). Post-depositional REE mobility in a Paleoproterozoic banded iron formation revealed by La-Ce geochronology: A cautionary tale for signals of ancient oxygenation. *Earth and Planetary Science Letters*, 547, 116452.
- Bosak, T., Knoll, A. H., & Petroff, A. P. (2013). The meaning of stromatolites. *Annual Review of Earth and Planetary Sciences*, 41(1), 21–44.
- Bowring, S. A., & Williams, I. S. (1999). Priscoan (4.00-4.03 Ga) orthogneisses from northwestern Canada. *Contributions to Mineralogy and Petrology*, 134(1), 3–16.

- Braterman, P. S., Cairns-Smith, A. G., & Sloper, R. W. (1983). Photo-oxidation of hydrated Fe²⁺-significance for banded iron formations. *Nature*, 303(5913), 163–164.
- Brocks, J. J., Buick, R., Logan, G. A., & Summons, R. E. (2003). Composition and syngeneity of molecular fossils from the 2.78 to 2.45-billion-year-old Mount Bruce Supergroup, Pilbara Craton, Western Australia. *Geochimica et Cosmochimica Acta*, 67(22), 4389–4319.
- Byrne, R. H., & Lee, J. H. (1993). Comparative yttrium and rare earth element chemistries in seawater. *Marine Chemistry*, 44(2), 121–130.
- Byrne, R. H., & Sholkovitz, E. R. (1996). Marine chemistry and geochemistry of the lanthanides. In K. A. Gschneidner, Jr. and L. Eyring (Ed.), *The Handbook on the Physics and Chemistry of Rare Earths*, pp. 497–593. Netherlands: Elsevier.
- Cairns-Smith, A. G. (1978). Precambrian solution photochemistry, inverse segregation, and banded iron formations. *Nature*, 276(5690), 807–808.
- Cantrell, K. J., & Byrne, R. H. (1987). Rare earth element complexation by carbonate and oxalate ions. *Geochimica et Cosmochimica Acta*, 51(3), 597–605.
- Capitanio, F. A., Nebel, O., Cawood, P. A., Weinberg, R. F., & Clos, F. (2019). Lithosphere differentiation in the early Earth controls Archean tectonics. *Earth and Planetary Science Letters*, 525, 115755.
- Cates, N. L., Ziegler, K., Schmitt, A. K., & Mojzsis, S. J. (2013). Reduced, reused and recycled: Detrital zircons define a maximum age for the Eoarchean (ca. 3750–3780Ma) Nuvvuagittuq Supracrustal Belt, Québec (Canada). *Earth and Planetary Science Letters*, 362, 283–293.
- Cawood, P. A., Hawkesworth, C. J., Pisarevsky, S. A., Dhuime, B., Capitanio, F. A., & Nebel, O. (2018). Geological archive of the onset of plate tectonics. *Philosophical Transactions of the Royal Society A: Mathematical, Physical and Engineering Sciences*, 376(2132), 20170405.
- Cawood, P. A., Kröner, A., & Pisarevsky, S. (2006). Precambrian plate tectonics; criteria and evidence. *GSA Today*, 16(7), 4–11.
- Censi, P., Inguaggiato, C., Chiavetta, S., Schembri, C., Sposito, F., Censi, V., & Zuddas, P. (2017). The behaviour of zirconium, hafnium and rare earth elements during the crystallisation of halite and other salt minerals. *Chemical Geology*, 453, 80–91.
- Chaudhuri, T. (2020). A review of Hadean to Neoproterozoic crust generation in the Singhbhum Craton, India and possible connection with Pilbara Craton, Australia; the geochronological perspective. *Earth-Science Reviews*, 202, 103085.
- Cloud, P. (1968). Atmospheric and hydrospheric evolution on the primitive Earth. *Science*, 160, 729–736.
- Cox, G. M., Halverson, G. P., Minarik, W. G., Le Heron, D. P., Macdonald, F. A., Bellefroid, E. J., & Strauss, J. V. (2013). Neoproterozoic iron formation; an evaluation of its temporal, environmental and tectonic significance. *Chemical Geology*, 362, 232–249.
- Crowe, S. A., Dossing, L. N., Beukes, N. J., Bau, M., Kruger, S. J., Frei, R., & Canfield, D. E. (2013). Atmospheric oxygenation three billion years ago. *Nature*, 501(7468), 535–538.
- Danielson, A., Möller, P., & Dulski, P. (1992). The europium anomalies in banded iron formations and the thermal history of the oceanic crust. *Chemical Geology*, 97(1), 89–100.
- Dauphas, N., Cates, N. L., Mojzsis, S. J., & Busigny, V. (2007). Identification of chemical sedimentary protoliths using iron isotopes in the > 3750 Ma Nuvvuagittuq supracrustal belt, Canada. *Earth and Planetary Science Letters*, 254(3–4), 358–376.
- De Baar, H. J. W., Brewer, P. G., & Bacon, M. P. (1985). Anomalies in rare earth distributions in seawater: Gd and Tb. *Geochimica et Cosmochimica Acta*, 49(9), 1961–1969.
- De Baar, H. J. W., Schijf, J., & Byrne, R. H. (1991). Solution chemistry of the rare earth elements in seawater. *European Journal of Solid State Inorganic Chemistry*, 28, 357–373.
- Debaille, V., O'Neill, C., Brandon, A. D., Haenecour, P., Yin, Q. Z., Mattielli, N., & Treiman, A. H. (2013). Stagnant-lid tectonics in early Earth revealed by ¹⁴²Nd variations in late Archean rocks. *Earth and Planetary Science Letters*, 373, 83–92.

- DeWit, M., & Ashwal, L. D. (1997). *Greenstone belts* (1st ed.). Oxford: Clarendon Press.
- Dey, S., Topno, A., Liu, Y., & Zong, K. (2017). Generation and evolution of Palaeoarchean continental crust in the central part of the Singhbhum Craton, eastern India. *Precambrian Research*, 298, 268–291.
- Dhuime, B., Hawkesworth, C. J., Cawood, P. A., & Storey, C. D. (2012). A change in the geodynamics of continental growth 3 billion years ago. *Science*, 335(6074), 1334–1336.
- Douville, E., Bienvenu, P., Charlou, J. L., Donval, J. P., Fouquet, Y., Appriou, P., & Gamo, T. (1999). Yttrium and rare earth elements in fluids from various deep-sea hydrothermal systems. *Geochimica et Cosmochimica Acta*, 63(5), 627–643.
- Douville, E., Charlou, J. L., Oelkers, E. H., Bienvenu, P., Colon, C. F. J., Donval, J. P., Fouquet, Y., Prieur, D., & Appriou, P. (2002). The rainbow vent fluids (36°14'N, MAR): the influence of ultramafic rocks and phase separation on trace metal content in Mid-Atlantic Ridge hydrothermal fluids. *Chemical Geology*, 184(1-2), 37–48.
- Dudley, R. (1998). Atmospheric oxygen, giant Paleozoic insects and the evolution of aerial locomotor performance. *Journal of Experimental Biology*, 201(8), 1043–1050.
- Dulski, P. (2001). Reference materials for geochemical studies: New analytical data by ICP-MS and critical discussion of reference values. *Geostandards Newsletter*, 25(1), 87–125.
- Dymek, R. F., & Klein, C. (1988). Chemistry, petrology and origin of banded iron-formation lithologies from the 3800 MA isua supracrustal belt, West Greenland. *Precambrian Research*, 39(4), 247–302.
- Elderfield, H., Charnock, H., Lovelock, J. E., Liss, P. S., & Whitfield, M. (1988). The oceanic chemistry of the rare-earth elements. *Philosophical Transactions of the Royal Society of London. Series A: Mathematical and Physical Sciences*, 325(1583), 105–126.
- Elderfield, H., Upstill-Goddard, R., & Sholkovitz, E. R. (1990). The rare earth elements in rivers, estuaries, and coastal seas and their significance to the composition of ocean waters. *Geochimica et Cosmochimica Acta*, 54(4), 971–991.
- Erel, Y., & Stolper, E. M. (1993). Modeling of rare-earth element partitioning between particles and solution in aquatic environments. *Geochimica et Cosmochimica Acta*, 57(3), 513–518.
- Farquhar, J., Bao, H., & Thiemens, M. (2000). Atmospheric influence of Earth's earliest sulfur cycle. *Science*, 289(5480), 756–758.
- Fralick, P., & Riding, R. (2015). Steep Rock Lake; sedimentology and geochemistry of an Archean carbonate platform. *Earth-Science Reviews*, 151, 132–175.
- Frei, R., Gaucher, C., Poulton, S. W., & Canfield, D. E. (2009). Fluctuations in Precambrian atmospheric oxygenation recorded by chromium isotopes. *Nature*, 461(7261), 250–253.
- Friend, C. R. L., Nutman, A. P., Bennett, V. C., & Norman, M. D. (2008). Seawater-like trace element signatures (REE + Y) of Eoarchean chemical sedimentary rocks from southern West Greenland, and their corruption during high-grade metamorphism. *Contributions to Mineralogy and Petrology*, 155(2), 229–246.
- Garrels, R. M., Perry, E. A., & Mackenzie, F. T. (1973). Genesis of Precambrian Iron-Formations and the Development of Atmospheric Oxygen. *Economic Geology*, 68(7), 1173–1179.
- German, C. R., & Elderfield, H. (1990). Application of the Ce anomaly as a paleoredox indicator; The ground rules. *Paleoceanography*, 5(5), 823–833.
- German, C. R., Klinkhammer, G. P., Edmond, J. M., Mura, A., & Elderfield, H. (1990). Hydrothermal scavenging of rare-earth elements in the ocean. *Nature*, 345(6275), 516–518.
- Goldschmidt, V. M. (1925). *Geochemische Verteilungsgesetze der Elemente. Part V, Isomorphie und Polymorphie der Sesquioxide: die Lanthaniden-Kontraktion und ihre Konsequenzen*. Ja. Dybwad, Oslo.
- Goodwin, A. (1973). Archean iron-formations and tectonic basins of Canadian Shield. *Economic Geology*, 68, 915–933.
- Graham, J. B., Dudley, R., Aguilar, N. M., & Gans, C. (1995). Implications of the late Palaeozoic oxygen pulse for physiology and evolution. *Nature*, 375(6527), 117–120.

- Greaves, M. J., Elderfield, H., & Sholkovitz, E. R. (1999). Aeolian sources of rare earth elements to the Western Pacific Ocean. *Marine Chemistry*, 68(1–2), 31–38.
- Gross, G. A. (1965). Geology of iron deposits in Canada, general geology and evaluation of iron deposits. Geological Survey of Canada, Economic Geology Report, 22, 181.
- Gross, G. A. (1980). A classification of iron-formation based on depositional environments. *Canadian Mineralogist*, 18, 215–222.
- Gross, G. A. (1983). Tectonic systems and the deposition of iron-formation. *Precambrian Research*, 20, 171–187.
- Haley, B. A., Klinkhammer, G. P., & McManus, J. (2004). Rare earth elements in pore waters of marine sediments. *Geochimica et Cosmochimica Acta*, 68(6), 1265–1279.
- Han, T.-M., & Runnegar, B. (1992). Megascopic eukaryotic algae from the 2.1-billion-year-old Negaunee Iron-Formation, Michigan. *Science*, 257(5067), 232–235.
- Harrison, T. M., Blichert-Toft, J., Mueller, W., Albarede, F., Holden, P., & Mojzsis, S. J. (2005). Heterogeneous Hadean hafnium; evidence of continental crust at 4.4 to 4.5 Ga. *Science*, 310(5756), 1947–1950.
- Hartman, H. (1984). The evolution of photosynthesis and microbial mats: a speculation on the banded iron formations. In Y. Cohen, R. W. Castenholz, & H. O. Halvorson (Eds.), *Microbial Mats: Stromatolites*, pp. 449–453. Alan R. Liss.
- Henderson, P. (1984). *Rare earth element geochemistry*. Amsterdam: Elsevier.
- Herzberg, C., Condie, K., & Korenaga, J. (2010). Thermal history of the Earth and its petrological expression. *Earth and Planetary Science Letters*, 292(1–2), 79–88.
- Hoffman, P., Kaufman, A., Halverson, G., & Schrag, D. (1998). A Neoproterozoic Snowball Earth. *Science* 281, 1342–1346.
- Hofmann, A., Jodder, J., Xie, H., Bolhar, R., Whitehouse, M., & Elburg, M. (2022). The Archaean geological history of the Singhbhum Craton, India – a proposal for a consistent framework of craton evolution. *Earth-Science Reviews*, 228, 103994.
- Holland, H. D. (2002). Volcanic gases, black smokers, and the Great Oxidation Event. *Geochimica et Cosmochimica Acta*, 66(21), 3811–3826.
- Holland, H. D. (2006). The oxygenation of the atmosphere and oceans. *Philosophical Transactions of the Royal Society of London. Series B. Biological Sciences*, 361(1470), 903–915.
- Hopkins, M., Harrison, T. M., & Manning, C. E. (2008). Low heat flow inferred from >4 Gyr zircons suggests Hadean plate boundary interactions. *Nature*, 456(7221), 493–496.
- Huston, D. L., & Logan, G. A. (2004). Barite, BIFs and bugs: Evidence for the evolution of the Earth's early hydrosphere. *Earth and Planetary Science Letters*, 220(1–2), 41–55.
- Hyung, E., Jacobsen, S. B., & Canfield, D. E. (2020). The 142 Nd/ 144 Nd variations in mantle-derived rocks provide constraints on the stirring rate of the mantle from the Hadean to the present. *Proceedings of the National Academy of Sciences - PNAS*, 117(26), 14738–14744.
- Isley, A. E., & Abbott, D. H. (1999). Plume-related mafic volcanism and the deposition of banded iron formation. *Journal of Geophysical Research: Solid Earth*, 104, 15461–15477.
- Iyengar, S. V. P., & Murthy, Y. G. K. (1982). The evolution of the Archaean-Proterozoic crust in parts of Bihar and Orissa, eastern India. *Records of the Geological Survey of India*, 112, 1–5.
- Jacobsen, S. B., & Pimentel-Klose, M. R. (1988). A Nd isotopic study of the Hamersley and Michipicoten banded iron formations: the source of REE and Fe in Archean oceans. *Earth and Planetary Science Letters*, 87(1–2), 29–44.
- James, H. L. (1954). Sedimentary facies of iron-formation. *Economic Geology*, 49, 235–293.
- James, H. L. (1983). Distribution of Banded Iron-Formation in Space and Time. In A. F. Trendall & R. C. Morris (Eds.), *Iron-Formation Facts and Problems*, pp. 471–490. Amsterdam: Elsevier.

- Jena, B. K., & Behra, U. K. (2000). The oldest supracrustal belt from Singhbhum Craton and its possible correlation. *Precambrian Crust in Eastern and Central India. Proc. UNESCO-IUGS-IGCO*, 368, 106–121.
- Jodder, J. (2021). The geology of the Daitari greenstone belt, Singhbhum Craton, India - Insights into early life 3.5 Ga ago. Doctoral Dissertation, University of Johannesburg, South Africa.
- Jodder, J., Hofmann, A., Xie, H., Elburg, M. A., & Wilson, A. (2023). Geochronology of the Daitari Greenstone Belt, Singhbhum Craton, India. *Precambrian Research*, 388, 106997.
- Kamber, B. S., Bolhar, R., & Webb, G. E. (2004). Geochemistry of late Archaean stromatolites from Zimbabwe; evidence for microbial life in restricted epicontinental seas. *Precambrian Research*, 132(4), 370–399.
- Kasting, J. F., Pavlov, A. A., & Siefert, J. L. (2001). A coupled ecosystem-climate model for predicting the methane concentrations in the Archean atmosphere. *Origins of Life and Evolution of Biospheres*, 31(3), 271–285.
- Kendall, B., Reinhard, C. T., Lyons, T. W., Kaufman, A. J., Poulton, S. W., & Anbar, A. D. (2010). Pervasive oxygenation along late Archaean ocean margins. *Nature Geoscience*, 3(9), 647–652.
- Kesler, S. E., & Simon, A. F. (2015). *Mineral resources, economics and the environment* (2nd ed.). Cambridge: Cambridge University Press.
- Khan, R. M. K., Das Sharma, S., Patil, D. J., & Naqvi, S. M. (1996). Trace, rare-earth element, and oxygen isotopic systematics for the genesis of banded iron-formations; evidence from Kushtagi schist belt, Archaean Dharwar Craton, India. *Geochimica et Cosmochimica Acta*, 60(17), 3285–3294.
- Kirschvink, J. L. (1992). Late Proterozoic low-latitude global glaciation: The snowball Earth. In J. W. Schopf & C. Klein (Eds.), *The Proterozoic Biosphere: A Multidisciplinary Study*, pp. 51–52. Cambridge: Cambridge University Press.
- Klein, C., & Beukes, N. J. (1992). Time Distribution, Stratigraphy, and Sedimentologic Setting, and Geochemistry of Precambrian Iron-Formations. In J. W. Schopf & C. Klein (Eds.), *The Proterozoic Biosphere: A Multidisciplinary Study*, pp. 139–146. Cambridge: Cambridge University Press.
- Knoll, A. H., Javaux, E. J., Hewitt, D., & Cohen, P. (2006). Eukaryotic organisms in Proterozoic oceans. *Philosophical Transactions of the Royal Society B: Biological Sciences*, 361(1470), 1023–1038.
- Konhauser, K. O., Amskold, L., Lalonde, S. V., Posth, N. R., Kappler, A., & Anbar, A. (2007). Decoupling photochemical Fe(II) oxidation from shallow-water BIF deposition. *Earth and Planetary Science Letters*, 258(1–2), 87–100.
- Konhauser, K. O., Planavsky, N. J., Hardisty, D. S., Robbins, L. J., Warchola, T. J., Haugaard, R., Lalonde, S. V., Partin, C. A., Oonk, P. B. H., Tsikos, H., Lyons, T. W., Bekker, A., & Johnson, C. M. (2017). Iron formations: A global record of Neoproterozoic to Palaeoproterozoic environmental history. *Earth-Science Reviews*, 172, 140–177.
- Korenaga, J. (2006). Archean geodynamics and the thermal evolution of Earth. In K. Benn, J.-C. Mareschal & K.C. Condie (Eds.), *Archean Geodynamics and Environments*, pp. 7-32. American Geophysical Union, Washington, DC.
- Korenaga, J. (2013). Initiation and evolution of plate tectonics on Earth: Theories and observations. *Annual Review of Earth and Planetary Sciences*, 41, 117–151.
- Krapež, B., Barley, M. E., & Pickard, A. L. (2003). Hydrothermal and resedimented origins of the precursor sediments to banded iron formation: Sedimentological evidence from the Early Palaeoproterozoic Brockman Supersequence of Western Australia. *Sedimentology*, 50(5), 979–1011.
- Lawrence, M. G., & Kamber, B. S. (2006). The behaviour of the rare earth elements during estuarine mixing—revisited. *Marine Chemistry*, 100(1), 147-161.
- Lee, J. H., & Byrne, R. H. (1993). Complexation of trivalent rare earth elements (Ce, Eu, Gd, Tb, Yb) by carbonate ions. *Geochimica et Cosmochimica Acta*, 57(2), 295–302.
- Logan, G. A., Hayes, J. M., Hieshima, G. B., & Summons, R. E. (1995). Terminal Proterozoic reorganization of biogeochemical cycles. *Nature*, 376(6535), 53–56.

- Lowenstein, T. K., Kendall, B., & Anbar, A. D. (2014). The Geologic History of Seawater. *Treatise on Geochemistry* (2nd ed.), pp. 569–622. Elsevier Ltd.
- Luo, Y.-R., & Byrne, R. H. (2004). Carbonate complexation of yttrium and the rare earth elements in natural waters. *Geochimica et Cosmochimica Acta*, 68(4), 691–699.
- Lyons, T. W., Reinhard, C. T., & Planavsky, N. J. (2014). The rise of oxygen in Earth's early ocean and atmosphere. *Nature* 506(7488), 307–315.
- McLennan, S. M. (1989). Rare earth elements in sedimentary rocks: influence of provenance and sedimentary processes. In B. R. Lipin & G. A. McKay (Eds.), *Geochemistry and Mineralogy of Rare Earth Elements*, pp. 169–200. Germany: De Gruyter.
- Merschel, G., Bau, M., Baldewein, L., Dantas, E. L., Walde, D., & Bühn, B. (2015). Tracing and tracking wastewater-derived substances in freshwater lakes and reservoirs: Anthropogenic gadolinium and geogenic REEs in Lake Paranoá, Brasília. *Comptes Rendus. Geoscience*, 347(5–6), 284–293.
- Miller, R. G., & O'Nions, R. K. (1995). Source of Precambrian chemical and elastic sediments. *Nature*, 314(6009), 325–330.
- Mitra, A., Dey, S., Das, P., Zong, K., Liu, Y., Mitra, A., & Gond, A. K. (2022). Time-space evolution of an ancient continent, a window to changing crustal architecture: Insights from granitoids of Singhbhum Craton, eastern India. *Earth Science Reviews*, 234, 104183.
- Mitra, A., Dey, S., Zong, K., Liu, Y., & Mitra, A. (2019). Building the core of a Paleoproterozoic continent. *Precambrian Research*, 335, 105436.
- Mloszewski, A. M., Pecoits, E., Cates, N. L., Mojzsis, S. J., O'Neil, J., Robbins, L. J., & Konhauser, K. O. (2012). The composition of Earth's oldest iron formations; the Nuvvuagittuq supracrustal belt (Quebec, Canada). *Earth and Planetary Science Letters*, 317–318, 331–342.
- Mojzsis, S. J., Harrison, T. M., & Pidgeon, R. T. (2001). Oxygen-isotope evidence from ancient zircons for liquid water at the Earth's surface 4,300 Myr ago. *Nature*, 409(6817), 178–181.
- Möller, P., & Bau, M. (1993). Rare-earth patterns with positive cerium anomaly in alkaline waters from Lake Van, Turkey. In *Earth and Planetary Science Letters*, 117(3-4), 671-676.
- Möller, P., Dulski, P., & Bau, M. (1994). Rare-earth element adsorption in a seawater profile above the East Pacific Rise. *Chemie der Erde*, 54, 129–149.
- Moore, W. B., & Webb, A. A. G. (2013). Heat-pipe earth. *Nature*, 501(7468), 501–505.
- Moresi, L., & Solomatov, V. (1998). Mantle convection with a brittle lithosphere: thoughts on the global tectonic styles of the Earth and Venus. *Geophysical Journal International*, 133(3), 669–682.
- Mukhopadhyay, D., & Matin, A. (2020). The architecture and evolution of the Singhbhum Craton. *Episodes*, 43(1), 19–50.
- Mukhopadhyay, J., Ghosh, G., Zimmermann, U., Guha, S., & Mukherjee, T. (2012). A 3.51 Ga bimodal volcanics-BIF-ultramafic succession from Singhbhum Craton: Implications for Palaeoproterozoic geodynamic processes from the oldest greenstone succession of the Indian subcontinent. *Geological Journal*, 47(2–3), 284–311.
- Murray, R. W., Jones, D. L., & Buchholtz-ten Brink, M. R. (1992). Diagenetic formation of bedded chert; evidence from chemistry of the chert-shale couplet. *Geology*, 20(3), 271–274.
- Murthy, V. N., & Acharya, S. (1975). Lithostratigraphy of the Precambrian rocks around Koira, Sundergarh district, Orissa. *Journal of Geological Society of India*, 16, 55–68.
- Nance, W. B., & Taylor, S. R. (1976). Rare earth element patterns and crustal evolution—I. Australian post-Archean sedimentary rocks. *Geochimica et Cosmochimica Acta*, 40(12), 1539–1551.
- Nelson, D. R., Bhattacharya, H. N., Thern, E. R., & Altermann, W. (2014). Geochemical and ion microprobe U/Pb zircon constraints on the Archean evolution of Singhbhum Craton, eastern India. *Precambrian Research*, 255, 412–432.
- Nozaki, Y., Alibo, D. S., Amakawa, H., Gamo, T., & Hasumoto, H. (1999). Dissolved rare earth elements and hydrography in the Sulu Sea. *Geochimica et Cosmochimica Acta*, 63(15), 2171–2181.

- Nozaki, Y., Zhang, J., & Amakawa, H. (1997). The fractionation between Y and Ho in the marine environment. *Earth and Planetary Science Letters*, 148(1–2), 329–340.
- Nutman, A. P., Allaart, J. H., Bridgwater, D., Dimroth, E., & Rosing, M. (1984). Stratigraphic and geochemical evidence for the depositional environment of the early Archaean Isua supracrustal belt, southern West Greenland. *Precambrian Research*, 25(4), 365–396.
- Nutman, A. P., Bennett, V. C., Friend, C. R. L., & Rosing, M. T. (1997). 3710 and > 3790 Ma volcanic sequences in the Isua (Greenland) supracrustal belt; structural and Nd isotope implications. *Chemical Geology*, 141(3), 271–287.
- Nutman, A. P., Friend, C. R. L., Barker, S. L. L., & McGregor, V. R. (2004). Inventory and assessment of Palaeoarchaeoan gneiss terrains and detrital zircons in southern West Greenland. *Precambrian Research*, 135(4), 281–314.
- Ohta, A., & Kawabe, I. (2000). Rare earth element partitioning between Fe oxyhydroxide precipitates and aqueous NaCl solutions doped with NaHCO₃: Determinations of rare earth element complexation constants with carbonate ions. *Geochemical Journal*, 34(6), 439–454.
- Ohta, A., & Kawabe, I. (2001). REE(III) adsorption onto Mn dioxide (δ -MnO₂) and Fe oxyhydroxide: Ce(III) oxidation by δ -MnO₂. *Geochimica et Cosmochimica Acta*, 65(5), 695–703.
- Olierook, H. K. H., Clark, C., Reddy, S. M., Mazumder, R., Jourdan, F., & Evans, N. J. (2019). Evolution of the Singhbhum Craton and supracrustal provinces from age, isotopic and chemical constraints. *Earth-Science Reviews*, 193, 237–259.
- O’Neil, J., Carlson, R. W., Paquette, J. L., & Francis, D. (2012). Formation age and metamorphic history of the Nuvvuagittuq Greenstone Belt. *Precambrian Research*, 220–221, 23–44.
- O’Neill, C., Lenardic, A., Moresi, L., Torsvik, T. H., & Lee, C. T. A. (2007). Episodic Precambrian subduction. *Earth and Planetary Science Letters*, 262(3–4), 552–562.
- Pack, A., Russell, S. S., Shelley, J. M. G., & van Zuilen, M. (2007). Geo- and cosmochemistry of the twin elements yttrium and holmium. *Geochimica et Cosmochimica Acta*, 71(18), 4592–4608.
- Pandey, O. P., Mezger, K., Ranjan, S., Upadhyay, D., Villa, I. M., Naegler, T. F., & Vollstaedt, H. (2019). Genesis of the Singhbhum Craton, eastern India; implications for Archean crust-mantle evolution of the Earth. *Chemical Geology*, 512, 85–106.
- Pavlov, A. A., & Kasting, J. F. (2002). Mass-independent fractionation of sulfur isotopes in Archean sediments; strong evidence for an anoxic Archean atmosphere. *Astrobiology*, 2(1), 27–41.
- Pickard, A. L. (2003). SHRIMP U-Pb zircon ages for the Palaeoproterozoic Kuruman Iron Formation, Northern Cape Province, South Africa: Evidence for simultaneous BIF deposition on Kaapvaal and Pilbara Cratons. *Precambrian Research*, 125(3–4), 275–315.
- Piper, J. D. A. (2013). A planetary perspective on Earth evolution: Lid Tectonics before Plate Tectonics. *Tectonophysics*, 589, 44–56.
- Planavsky, N., Bekker, A., Rouxel, O. J., Kamber, B., Hofmann, A., Knudsen, A., & Lyons, T. W. (2010). Rare earth element and yttrium compositions of Archean and Paleoproterozoic Fe formations revisited: New perspectives on the significance and mechanisms of deposition. *Geochimica et Cosmochimica Acta*, 74(22), 6387–6405.
- Posth, N. R., Konhauser, K. O., & Kappler, A. (2011). Banded Iron Formations. In V. Thiel & J. Reitner (Eds.), *Encyclopedia of Geobiology*, pp. 92–101. Germany: Springer
- Robbins, L. J., Funk, S. P., Flynn, S. L., Warchola, T. J., Li, Z., Lalonde, S. V., Rostron, B. J., Smith, A. J. B., Beukes, N. J., de Kock, M. O., Heaman, L. M., Alessi, D. S., & Konhauser, K. O. (2019). Hydrogeological constraints on the formation of Palaeoproterozoic banded iron formations. *Nature Geoscience*, 12(7), 558–563.
- Rosas, J. C., & Korenaga, J. (2018). Rapid crustal growth and efficient crustal recycling in the early Earth: Implications for Hadean and Archean geodynamics. *Earth and Planetary Science Letters*, 494, 42–49.
- Rosing, M. T. (1999). ¹³C-depleted carbon microparticles in >3700-Ma sea-floor sedimentary rocks from West Greenland. *Science*, 283(5402), 674–676.

- Saha, A. K. (1994). Crustal evolution of Singhbhum-North Orissa, Eastern India. *Memoir of Geological Society of India*, 27, 341.
- Sakar, S. N., & Saha, A. K. (1962). A revision of the Precambrian stratigraphy and tectonics of Singhbhum and adjacent region. *Q. J. Geol. Min. Metall. Soc. India*, 34, 97–136.
- Sampaio, G. M. S., & Enzweiler, J. (2015). New ICP-MS results for trace elements in five iron-formation reference materials. *Geostandards and Geoanalytical Research*, 39(1), 105–119.
- Shannon, R. D. (1976). Revised effective ionic radii and systematic studies of interatomic distances in halides and chalcogenides. *Acta Crystallographica Section A*, 32(5), 751–161.
- Shirey, S. B., & Richardson, S. H. (2011). Start of the Wilson cycle at 3 Ga shown by diamonds from subcontinental mantle. *Science*, 333, 434–436.
- Sholkovitz, E. R. (1992). Chemical evolution of rare earth elements: fractionation between colloidal and solution phases of filtered river water. *Earth and Planetary Science Letters*, 114(1), 77–84.
- Sholkovitz, E. R., Landing, W. M., & Lewis, B. L. (1994). Ocean particle chemistry: The fractionation of rare earth elements between suspended particles and seawater. *Geochimica et Cosmochimica Acta*, 58(6), 1567–1579.
- Sholkovitz, E. R., Piegras, D. J., & Jacobsen, S. B. (1989). The pore water chemistry of rare earth elements in Buzzards Bay sediments. *Geochimica et Cosmochimica Acta*, 53(11), 2847–2856.
- Sholkovitz, E. R., & Shen, G. T. (1995). The incorporation of rare earth elements in modern coral. *Geochimica et Cosmochimica Acta*, 59(13), 2749–2756.
- Simonson, B. M. (2003). Origin and evolution of large Precambrian iron formations. In Chan, M.A., and Archer, A.W. (Eds.), *Extreme depositional environments: Mega and members in geologic time: Boulder Colorado*, Geological Society of American Special Paper 370, pp. 231–244.
- Slack, J. F., Grenne, T., Bekker, A., Rouxel, O. J., & Lindberg, P. A. (2007). Suboxic deep seawater in the late Paleoproterozoic: Evidence from hematitic chert and iron formation related to seafloor-hydrothermal sulfide deposits, central Arizona, USA. *Earth and Planetary Science Letters*, 255(1–2), 243–256.
- Smit, K. V., Shirey, S. B., Hauri, E. H., & Stern, R. A. (2019). Sulfur isotopes in diamonds reveal differences in continent construction. *Science*, 364, 383–385.
- Stern, R. J. (2005). Evidence from ophiolites, blueschists, and ultrahigh-pressure metamorphic terranes that the modern episode of subduction tectonics began in Neoproterozoic time. *Geology*, 33(7), 557–560.
- Summons, R. E., Jahnke, L. L., Hope, J. M., & Logan, G. A. (1999). 2-methylhopanoids as biomarkers for cyanobacterial oxy-genic photosynthesis. *Nature*, 400(6744), 554–557.
- Sun, S., & Li, Y.-L. (2016). Geneses and evolutions of iron-bearing minerals in banded iron formations of >3760 to ca. 2200 million-year-old: Constraints from electron microscopic, X-ray diffraction and Mössbauer spectroscopic investigations. *Precambrian Research*, 289, 1–17.
- Tackley, P. J. (1998). Self-consistent generation of tectonic plates in three-dimensional mantle convection. *Earth and Planetary Science Letters*, 157, 9–22.
- Tang, M., Chen, K., & Rudnick, R. L. (2016). Archean upper crust transition from mafic to felsic marks the onset of plate tectonics. *Science*, 351, 372–375.
- Taylor, S. R., & McLennan, S. M. (1985). *The continental crust: its composition and evolution; an examination of the geochemical record preserved in sedimentary rocks* (1st ed.). Oxford: Blackwell.
- Tepe, N., & Bau, M. (2016). Behavior of rare earth elements and yttrium during simulation of arctic estuarine mixing between glacial-fed river waters and seawater and the impact of inorganic (nano-)particles. *Chemical Geology*, 438, 134–145.
- Toyoda, K., & Tokonami, M. (1990). Diffusion of rare-earth elements in fish teeth from deep-sea sediments. *Nature*, 345(6276), 607–609.
- Trendall, A. F. (1968). Three Great Basins of Precambrian BIF. *Geological Society of America Bulletin*, 79(11), 1527–1544.

- Turner, S., Wilde, S., Wörner, G., Schaefer, B., & Lai, Y.-J. (2020). An andesitic source for Jack Hills zircon supports onset of plate tectonics in the Hadean. *Nature Communications*, 11, 1241.
- Valley, J. W., Peck, W. H., King, E. M., & Wilde, S. A. (2002). A cool early Earth. *Geology*, 30(4), 351–154.
- Van Hunen, J., & Moyn, J. F. (2012). Archean subduction: Fact or fiction? *Annual Review of Earth and Planetary Sciences*, 40, 195–219.
- Veizer, J. (1983). Geologic evolution of the Archean-Early Proterozoic Earth. In J. W. Schopf (Ed.), *Earth's Earliest Biosphere*, pp. 240–259. Princeton University Press.
- Viehmann, S., Bau, M., Bühn, B., Dantas, E. L., Andrade, F. R. D., & Walde, D. H. G. (2016). Geochemical characterisation of Neoproterozoic marine habitats: Evidence from trace elements and Nd isotopes in the Urucum iron and manganese formations, Brazil. *Precambrian Research*, 282, 74–96.
- Viehmann, S., Bau, M., Hoffmann, J. E., & Münker, C. (2015). Geochemistry of the Krivoy Rog Banded Iron Formation, Ukraine, and the impact of peak episodes of increased global magmatic activity on the trace element composition of Precambrian seawater. *Precambrian Research*, 270, 165–180.
- Viehmann, S., Bau, M., Smith, A. J. B., Beukes, N. J., Dantas, E. L., & Bühn, B. (2015). The reliability of ~2.9 Ga old Witwatersrand banded iron formations (South Africa) as archives for Mesoarchean seawater: Evidence from REE and Nd isotope systematics. *Journal of African Earth Sciences*, 111, 322–334.
- Waggoner, B. (1998). Interpreting the Earliest Metazoan Fossils: What Can We Learn? *American Zoologist*, 38(6), 975–982.
- Watson, E. B., & Harrison, T. M. (2005). Zircon thermometer reveals minimum melting conditions on earliest Earth. *Science*, 308(5723), 841–844.
- Webb, G. E., & Kamber, B. S. (2000). Rare earth elements in Holocene reefal microbialites; a shallow seawater proxy. *Geochimica et Cosmochimica Acta*, 64(9), 1557–1565.
- Widdel, F., Schnell, S., Heising, S., Ehrenreich, A., Assmus, B., & Schink, B. (1993). Ferrous iron oxidation by anoxygenic phototrophic bacteria. *Nature*, 362(6423), 834–836.
- Wilde, S. A., Valley, J. W., Peck, W. H., & Graham, C. M. (2001). Evidence from detrital zircons for the existence of continental crust and oceans on the Earth 4.4 Gyr ago. *Nature*, 409(6817), 175–178.
- Wright, J., Schrader, H., & Holser, W. T. (1987). Paleoredox variations in ancient oceans recorded by rare earth elements in fossil apatite. *Geochimica et Cosmochimica Acta*, 51(3), 631–644.
- Zhang, J., Amakawa, H., & Nozaki, Y. (1994). The comparative behaviors of yttrium and lanthanides in the seawater of the North Pacific. *Geophysical Research Letters*, 21(24), 2677–2680.
- Zhang, J., & Nozaki, Y. (1996). Rare earth elements and yttrium in seawater: ICP-MS determinations in the East Caroline, Coral Sea, and South Fiji basins of the western South Pacific Ocean. *Geochimica et Cosmochimica Acta*, 60(23), 4631–4644.
- Zolensky, M. E. (2005). Extraterrestrial water. *Elements*, 1, 39–43.

Appendix

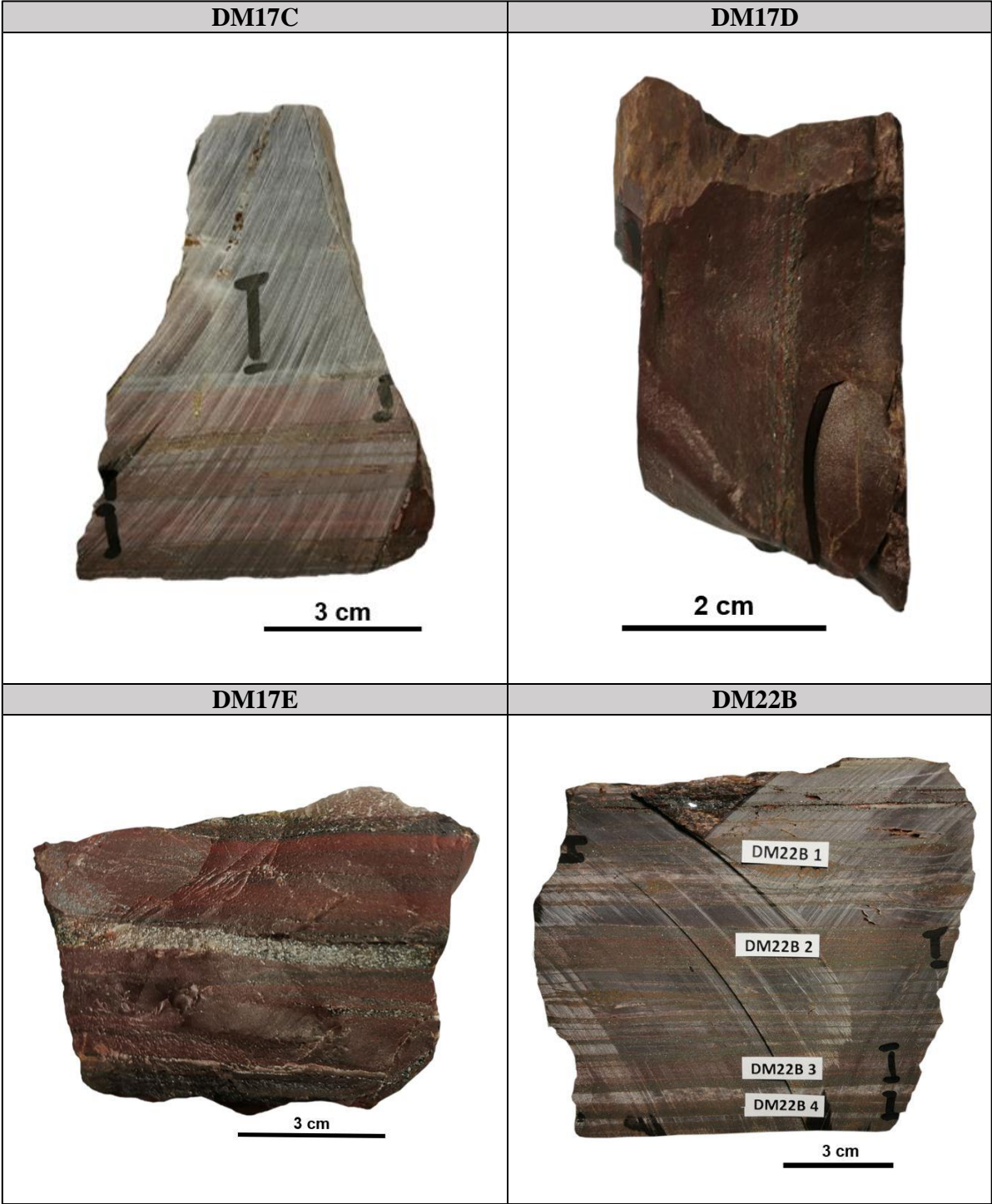


Figure A1: Samples of Tomka BIF (DM17C, DM17D, DM17E and DM22B). The samples show fine lamination (> 1 mm to 1 cm) with grey-metallic Fe-bands and red chert layers (Jasper).



Figure A2: Samples of Tomka BIF (DM22C, DM22D, DM76A and DM90). The samples show fine lamination (> 1 mm to 1 cm) with grey-metallic Fe-bands and white-greyish or red (Jasper) chert layers.

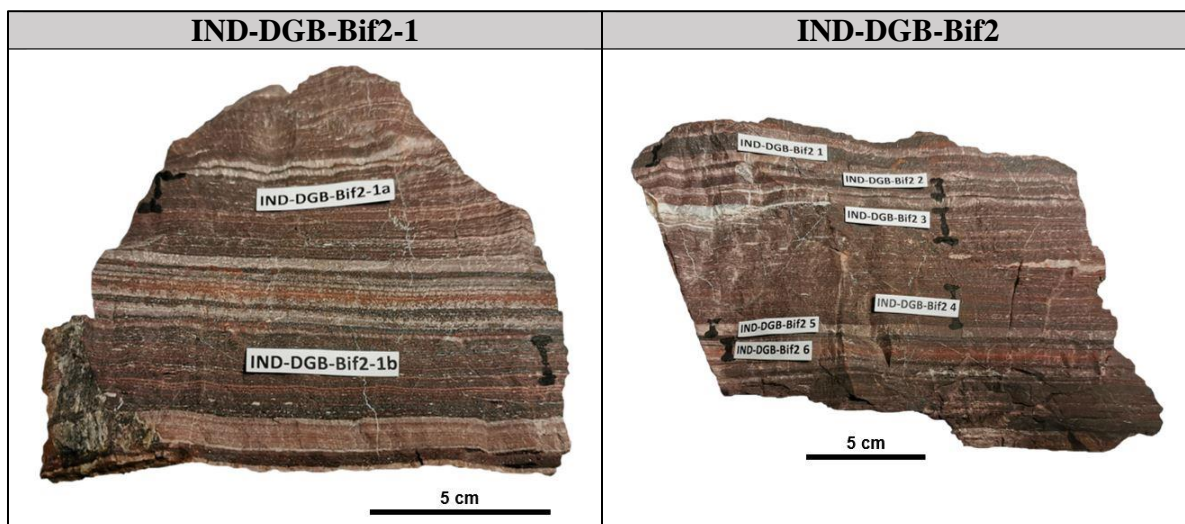


Figure A3: Samples of Tomka BIF (IND-DGB-Bif2-1 and IND-DGB-Bif2). The samples show fine lamination (> 1 mm to 1 mm) with grey-metallic Fe-bands and white-greyish or reddish chert layers.

Table A1: Trace element concentrations (in ppm) of Tomka BIF samples, shale sample DM71, and BIF reference material.

Sample-ID	DM17E1	DM17E2	DM17E3	DM76A 1	DM76A 2	DM17C 1	DM17C 2	DM17C 3	DM17C 4	DM17D 1
Type	Chert	Chert	Chert	Chert	Chert	Chert	Chert	Fe-band	Mixed bands	Chert
Li	0.11	0.17	0.18	0.19	0.10	0.32	0.63	0.28	0.73	0.57
Be	0.068	0.027	0.092	0.095	0.042	0.077	0.142	1.07	0.237	0.113
B	2.23	2.37	2.37	2.17	1.76	2.02	2.32	2.89	2.89	2.14
Na	13.2	16.2	18.1	14.9	13.1	32.6	24.1	18.6	23.4	36.9
Mg	9.39	24.4	89.6	700	213	227	4413	343	1453	1715
Al	<LOQ	<LOQ	<LOQ	613	251	334	120	316	<LOQ	119
P	55.4	43.7	57.1	95.3	51.1	51.8	52.1	108	56.2	57.5
K	59.6	66.7	62.6	64.6	54.0	161	93.1	80.7	72.8	68.2
Sc	0.21	0.41	0.29	4.55	0.99	0.28	0.39	0.51	0.19	0.59
Ti	2.62	1.93	3.53	16.0	6.59	5.35	1.95	5.63	1.30	1.60
V	0.70	0.47	0.85	7.65	3.58	0.38	0.43	2.34	0.31	0.64
Cr	65.8	39.3	32.1	92.8	42.7	66.9	28.3	140	27.0	40.6
Mn	8.38	15.2	27.0	702	245	22.6	360	407	135	450
Co	1.51	2.21	0.698	104	42.4	9.20	2.60	7.45	0.952	2.26
Ni	45.5	36.8	22.7	184	101	46.8	29.5	127	21.8	36.1
Zn	<LOQ	11.1	<LOQ	<LOQ	<LOQ	<LOQ	<LOQ	6.98	<LOQ	<LOQ
Ga	0.052	0.041	0.067	0.847	0.245	0.180	0.099	0.320	0.098	0.093
Ge	0.63	0.42	1.02	3.44	1.24	0.148	1.10	5.79	0.82	1.17
As	<LOQ	<LOQ	0.21	66.0	21.4	0.43	0.54	2.34	0.68	0.72
Se	4.63	4.88	5.11	5.78	4.64	5.06	5.58	5.77	6.85	4.98
Rb	0.018	0.035	0.026	0.085	0.022	0.246	0.110	0.094	0.071	0.037
Sr	0.21	0.10	0.33	1.64	0.63	0.17	0.60	1.28	0.32	1.03
Y	0.29	0.29	0.47	50.8	19.1	2.89	0.59	1.73	0.59	0.30
Zr	0.21	0.36	0.22	1.40	0.36	0.55	0.24	0.21	0.81	0.17
Nb	0.03	0.01	0.03	0.10	0.05	0.03	0.01	0.04	<LOQ	0.01
Mo	7.08	4.16	3.30	9.06	4.39	6.84	3.05	15.7	2.82	4.25
Ru	<LOQ	<LOQ	<LOQ	<LOQ	<LOQ	<LOQ	<LOQ	<LOQ	<LOQ	<LOQ
Ag	<LOQ	<LOQ	<LOQ	0.018	<LOQ	<LOQ	<LOQ	<LOQ	<LOQ	<LOQ
Cd	0.017	0.013	0.012	0.024	0.015	0.019	0.012	0.031	<LOQ	0.014
In	0.001	0.011	0.004	0.028	0.006	<LOQ	0.005	0.016	0.002	0.008
Sn	0.966	2.56	0.531	0.514	0.606	0.382	0.680	0.093	0.235	0.234
Sb	0.09	<LOQ	0.10	0.82	0.47	0.06	0.17	0.71	0.21	0.16
Te	<LOQ	<LOQ	<LOQ	0.009	0.005	0.007	<LOQ	<LOQ	<LOQ	<LOQ
Cs	0.001	0.002	0.002	0.006	0.004	0.009	0.010	0.010	0.012	0.007
Ba	<LOQ	<LOQ	<LOQ	<LOQ	<LOQ	3.81	4.09	3.63	2.26	8.49
La	0.146	0.068	0.175	11.6	1.88	0.458	0.085	0.422	0.075	0.059
Ce	0.33	0.15	0.38	25.4	4.25	0.67	0.13	0.64	0.13	0.10
Pr	0.047	0.022	0.060	3.20	0.546	0.069	0.015	0.072	0.015	0.013
Nd	0.225	0.107	0.307	13.6	2.32	0.286	0.067	0.330	0.065	0.062
Sm	0.056	0.033	0.082	3.96	0.919	0.075	0.019	0.083	0.019	0.018
Eu	0.017	0.009	0.023	0.858	0.251	0.044	0.014	0.048	0.013	0.010
Gd	0.050	0.037	0.065	5.66	1.95	0.188	0.039	0.133	0.037	0.025
Tb	0.006	0.005	0.008	0.997	0.374	0.036	0.006	0.022	0.006	0.004
Dy	0.032	0.032	0.051	6.30	2.47	0.268	0.049	0.166	0.047	0.027
Ho	0.007	0.007	0.011	1.33	0.523	0.062	0.012	0.042	0.012	0.007
Er	0.019	0.021	0.033	4.08	1.53	0.192	0.041	0.131	0.043	0.024
Tm	0.003	0.004	0.005	0.582	0.223	0.026	0.006	0.020	0.007	0.004
Yb	0.020	0.026	0.035	3.81	1.43	0.154	0.045	0.142	0.047	0.031
Lu	0.003	0.004	0.006	0.536	0.199	0.023	0.008	0.023	0.008	0.005
Hf	<LOQ	<LOQ	<LOQ	0.06	<LOQ	<LOQ	<LOQ	<LOQ	<LOQ	<LOQ
Ta	<LOQ	<LOQ	<LOQ	<LOQ	<LOQ	<LOQ	<LOQ	<LOQ	<LOQ	<LOQ
W	0.512	0.151	0.563	1.16	0.668	0.248	0.237	2.202	0.249	0.632
Re	<LOQ	<LOQ	<LOQ	0.006	0.002	<LOQ	<LOQ	0.002	<LOQ	<LOQ
Pt	<LOQ	<LOQ	<LOQ	<LOQ	<LOQ	<LOQ	<LOQ	<LOQ	<LOQ	<LOQ
Au	<LOQ	<LOQ	<LOQ	<LOQ	<LOQ	<LOQ	<LOQ	<LOQ	<LOQ	<LOQ
Tl	<LOQ	<LOQ	<LOQ	<LOQ	<LOQ	0.010	0.008	<LOQ	0.008	<LOQ
Pb	<LOQ	<LOQ	<LOQ	0.39	0.33	<LOQ	<LOQ	0.57	0.31	<LOQ
Th	<LOQ	0.017	0.006	0.042	0.006	0.022	<LOQ	0.008	0.007	<LOQ
U	0.005	0.005	0.008	0.108	0.037	0.008	<LOQ	0.010	0.005	<LOQ

Table A1: (continued)

Sample-ID	DMI7D 2	DM22D 1	DM22D 2	DM22B 1	DM22B 2	DM22B 3	DM22B 4	DM22C 1	DM22C 2	DM90 1
Type	Chert	Fe-band	Fe-band	Mixed bands	Fe/Chert	Fe-band				
Li	0.58	0.32	0.59	0.11	0.05	0.05	0.10	0.20	0.16	0.06
Be	0.107	1.75	2.60	0.621	1.69	0.959	1.80	1.06	0.978	3.24
B	2.30	5.56	3.69	15.5	5.00	7.59	12.2	2.54	3.14	2.46
Na	30.0	14.3	17.0	28.7	26.7	37.3	40.1	12.6	16.1	17.0
Mg	33.6	29.4	43.6	30.3	32.9	32.3	57.3	26.0	21.9	64.6
Al	171	1058	1642	634	1094	934	1219	315	298	836
P	46.7	74.5	131	55.0	64.0	60.9	87.0	82.6	75.1	103
K	82.6	102	100	192	243	303	340	75.8	103	60.1
Sc	0.35	0.75	1.06	0.61	0.79	0.59	0.90	0.35	0.31	0.37
Ti	1.69	19.8	48.6	14.4	19.3	16.5	61.9	8.36	4.05	27.5
V	0.54	3.60	6.22	2.19	2.90	2.39	6.04	2.54	1.41	5.17
Cr	47.1	47.3	88.1	71.7	47.4	45.0	85.0	53.5	80.1	93.1
Mn	14.8	71.8	103	21.5	56.1	35.0	76.7	217	152	82.8
Co	0.741	3.95	5.27	2.43	3.58	2.42	5.00	5.00	3.80	5.34
Ni	31.0	51.3	76.9	61.3	59.1	44.0	76.5	74.6	74.2	141
Zn	<LOQ	19.2	24.5	7.30	19.9	11.3	25.1	28.2	18.5	21.3
Ga	0.084	0.544	0.750	0.397	0.488	0.370	0.653	0.459	0.297	0.980
Ge	0.93	14.5	18.8	5.85	11.5	8.42	15.0	13.2	7.65	26.0
As	0.80	1.97	2.78	1.06	1.24	1.29	2.02	1.42	1.05	6.21
Se	5.41	4.88	4.50	4.98	5.05	5.01	4.35	4.92	5.54	4.03
Rb	0.089	0.205	0.209	0.626	0.859	1.12	1.41	0.073	0.191	0.182
Sr	0.34	0.87	1.82	0.49	0.52	0.40	0.86	0.29	0.29	2.59
Y	0.48	7.55	8.79	2.02	8.06	6.73	16.7	1.30	6.24	7.47
Zr	0.23	0.81	1.53	0.42	0.95	0.89	2.01	0.27	0.20	1.11
Nb	0.01	0.10	0.15	0.07	0.09	0.11	0.17	0.04	0.06	0.07
Mo	4.97	3.69	6.59	7.24	4.70	4.34	5.88	5.57	8.88	9.24
Ru	<LOQ	<LOQ	<LOQ	<LOQ	<LOQ	<LOQ	<LOQ	<LOQ	<LOQ	0.007
Ag	<LOQ	0.010	0.013	<LOQ	<LOQ	<LOQ	0.009	<LOQ	<LOQ	<LOQ
Cd	0.019	0.024	0.033	0.021	0.017	0.015	0.021	0.019	0.020	0.034
In	<LOQ	0.005	0.007	0.003	0.007	0.005	0.005	0.010	0.005	0.021
Sn	0.432	0.068	0.012	0.368	0.020	0.036	0.054	0.024	0.074	0.014
Sb	0.18	3.33	4.95	1.11	1.46	1.76	2.82	1.08	1.38	6.20
Te	<LOQ	0.045	0.086	<LOQ	0.014	0.012	0.028	0.020	0.013	0.041
Cs	0.009	0.007	0.009	0.014	0.012	0.018	0.022	0.005	0.008	0.038
Ba	3.62	4.50	8.12	3.59	5.56	7.04	9.00	<LOQ	2.59	5.00
La	0.066	4.48	13.5	0.782	1.34	0.958	3.56	2.26	1.32	5.07
Ce	0.09	2.47	5.81	0.75	1.66	1.20	4.71	2.60	1.41	6.29
Pr	0.009	0.412	0.860	0.094	0.239	0.182	0.567	0.269	0.152	0.786
Nd	0.043	1.60	2.98	0.417	1.05	0.821	2.51	1.13	0.644	3.36
Sm	0.012	0.275	0.422	0.089	0.269	0.229	0.622	0.203	0.130	0.667
Eu	0.012	0.146	0.220	0.066	0.179	0.142	0.419	0.074	0.082	0.316
Gd	0.029	0.474	0.723	0.142	0.444	0.379	1.11	0.171	0.283	0.748
Tb	0.006	0.069	0.094	0.020	0.068	0.066	0.178	0.016	0.046	0.086
Dy	0.042	0.494	0.612	0.134	0.492	0.464	1.27	0.091	0.354	0.539
Ho	0.009	0.127	0.150	0.032	0.128	0.119	0.318	0.023	0.094	0.130
Er	0.030	0.399	0.479	0.103	0.413	0.375	1.00	0.075	0.286	0.412
Tm	0.004	0.055	0.067	0.014	0.057	0.054	0.139	0.010	0.037	0.057
Yb	0.028	0.352	0.429	0.087	0.365	0.344	0.858	0.073	0.227	0.359
Lu	0.004	0.056	0.068	0.015	0.061	0.056	0.141	0.013	0.038	0.062
Hf	<LOQ	<LOQ	0.04	<LOQ	<LOQ	<LOQ	0.05	<LOQ	<LOQ	<LOQ
Ta	<LOQ	<LOQ	<LOQ	<LOQ	<LOQ	<LOQ	<LOQ	<LOQ	<LOQ	<LOQ
W	0.731	1.03	1.49	0.757	0.864	1.30	0.683	0.760	3.26	4.01
Re	<LOQ	0.002	0.002	0.002	0.002	0.002	0.003	<LOQ	0.002	0.003
Pt	<LOQ	<LOQ	<LOQ	<LOQ	<LOQ	<LOQ	<LOQ	<LOQ	<LOQ	0.002
Au	<LOQ	<LOQ	<LOQ	<LOQ	<LOQ	<LOQ	<LOQ	<LOQ	<LOQ	<LOQ
Tl	0.015	<LOQ	<LOQ	0.008	0.032	0.009	0.010	0.040	<LOQ	<LOQ
Pb	0.26	0.67	1.06	0.32	0.45	0.53	0.59	0.29	0.46	3.33
Th	<LOQ	0.033	0.076	0.010	0.024	0.025	0.089	0.011	0.006	0.036
U	<LOQ	0.012	0.020	0.008	0.015	0.011	0.024	0.008	0.007	0.039

Table A1: (continued)

Sample-ID	DM90 2	IND-DGB-Bif2-1a	IND-DGB-Bif2-1b	IND-DGB-Bif2 1	IND-DGB-Bif2 2	IND-DGB-Bif2 3	IND-DGB-Bif2 4
Type	Mixed bands	Mixed bands	Mixed bands	Mixed bands	Mixed bands	Mixed bands	Mixed bands
Li	0.05	0.30	0.37	0.13	0.18	0.31	0.24
Be	0.350	0.704	2.56	1.06	0.895	0.414	0.423
B	2.44	2.54	2.44	2.89	2.63	2.51	2.56
Na	10.6	52.4	24.4	17.4	27.5	75.3	62.7
Mg	21.1	20.8	50.2	26.8	18.1	28.3	28.2
Al	147	456	678	472	321	595	575
P	51.0	217	834	271	247	122	154
K	54.6	75.3	53.9	45.8	58.1	99.7	93.2
Sc	0.15	0.46	0.89	0.39	0.31	0.58	0.49
Ti	4.01	23.1	62.3	14.3	7.73	46.8	35.4
V	1.17	5.97	9.10	4.72	3.02	6.41	6.04
Cr	46.9	53.2	80.3	53.4	92.8	55.0	69.0
Mn	20.4	34.7	126	58.7	36.5	74.9	69.7
Co	1.43	4.02	13.2	13.6	6.68	6.07	8.20
Ni	46.0	51.9	94.4	96.8	86.9	60.3	76.4
Zn	<LOQ	7.86	21.8	27.9	14.3	21.1	18.9
Ga	0.192	0.526	1.02	0.846	0.458	0.600	0.625
Ge	4.35	8.84	15.7	18.0	8.43	6.79	7.69
As	1.45	6.08	6.21	4.56	5.43	4.26	4.44
Se	5.20	5.89	5.05	4.51	5.41	5.33	4.89
Rb	0.029	0.140	0.057	0.035	0.077	0.328	0.328
Sr	0.17	0.51	0.60	0.23	0.32	1.28	1.31
Y	10.1	5.05	31.9	20.3	8.43	21.5	27.3
Zr	0.27	1.30	2.84	0.49	0.49	2.08	1.69
Nb	0.04	0.11	0.23	0.07	0.06	0.19	0.13
Mo	5.17	4.83	6.21	5.26	9.99	4.51	6.39
Ru	<LOQ	<LOQ	<LOQ	<LOQ	<LOQ	<LOQ	<LOQ
Ag	<LOQ	0.010	0.015	0.020	0.018	0.011	0.012
Cd	0.011	0.019	0.028	0.018	0.021	0.013	0.019
In	0.004	0.004	0.009	0.004	0.003	0.008	0.007
Sn	0.425	0.064	0.073	2.73	0.461	0.132	0.043
Sb	1.39	1.85	1.98	1.51	1.40	1.15	1.14
Te	<LOQ	0.023	0.023	0.011	0.012	0.016	0.007
Cs	0.008	0.136	0.114	0.064	0.118	0.137	0.137
Ba	<LOQ	2.78	1.84	<LOQ	<LOQ	8.21	4.55
La	0.753	0.410	1.84	1.70	0.593	1.71	2.44
Ce	0.87	0.56	2.27	2.22	0.76	2.22	3.11
Pr	0.104	0.069	0.281	0.291	0.103	0.260	0.385
Nd	0.431	0.324	1.33	1.45	0.507	1.26	1.76
Sm	0.112	0.113	0.510	0.489	0.170	0.413	0.529
Eu	0.106	0.088	0.435	0.385	0.136	0.317	0.383
Gd	0.427	0.297	1.49	1.13	0.413	1.10	1.41
Tb	0.076	0.056	0.283	0.188	0.069	0.205	0.268
Dy	0.576	0.415	2.31	1.38	0.548	1.65	2.05
Ho	0.155	0.102	0.620	0.359	0.147	0.422	0.526
Er	0.492	0.334	1.96	1.15	0.479	1.40	1.63
Tm	0.067	0.051	0.286	0.153	0.068	0.194	0.212
Yb	0.427	0.346	1.83	1.00	0.439	1.26	1.27
Lu	0.071	0.059	0.300	0.168	0.076	0.203	0.204
Hf	<LOQ	<LOQ	0.07	<LOQ	<LOQ	0.05	<LOQ
Ta	<LOQ	<LOQ	<LOQ	<LOQ	<LOQ	<LOQ	<LOQ
W	0.948	2.51	3.34	3.47	3.29	1.95	1.65
Re	0.001	0.002	0.005	0.002	0.002	0.003	0.003
Pt	<LOQ	<LOQ	<LOQ	<LOQ	<LOQ	<LOQ	<LOQ
Au	<LOQ	<LOQ	<LOQ	<LOQ	<LOQ	<LOQ	<LOQ
Tl	<LOQ	<LOQ	<LOQ	<LOQ	<LOQ	0.008	0.012
Pb	0.73	1.24	1.68	1.38	1.22	1.32	1.25
Th	0.009	0.034	0.103	0.020	0.012	0.067	0.061
U	0.013	0.020	0.040	0.025	0.018	0.020	0.021

Table A1: (continued)

Sample-ID	IND-DGB-Bif2 5	IND-DGB-Bif2 6	DM71A	IF-G_1	IF-G_2
Type	Mixed bands	Mixed bands	Shale	BIF standard	BIF standard
Li	0.30	0.22	4.29	0.23	0.22
Be	0.150	0.038	-	6.14	5.74
B	2.52	2.34	-	2.62	2.44
Na	59.8	17.5	-	184	192
Mg	7.00	5.30	-	14039	14365
Al	353	<LOQ	62581	949	927
P	56.3	47.5	-	363	367
K	92.6	50.9	-	89.4	100
Sc	0.10	0.07	8.22	0.42	0.42
Ti	7.48	1.24	-	39.3	38.1
V	2.47	0.44	-	3.24	3.39
Cr	38.9	32.7	-	5.36	5.58
Mn	7.22	4.94	-	353	357
Co	1.15	1.16	3.52	3.98	4.12
Ni	28.2	24.8	47.8	28.3	28.7
Zn	<LOQ	<LOQ	-	25.7	26.5
Ga	0.238	0.106	14.8	0.825	0.828
Ge	2.40	1.01	-	14.3	14.4
As	1.66	0.77	-	4.59	3.39
Se	6.23	5.67	-	4.55	4.80
Rb	0.276	0.044	85.4	0.312	0.314
Sr	0.62	0.20	28.1	3.75	3.76
Y	3.02	0.99	11.0	10.1	9.96
Zr	0.59	0.13	116	0.98	0.97
Nb	0.07	0.01	8.17	0.08	0.08
Mo	4.09	3.53	<LOQ	0.39	0.34
Ru	<LOQ	<LOQ	-	0.004	0.004
Ag	<LOQ	<LOQ	-	0.013	0.014
Cd	0.011	0.007	-	0.038	0.039
In	0.001	<LOQ	<LOQ	0.004	0.004
Sn	0.116	3.61	-	0.014	0.017
Sb	0.50	0.20	0.09	0.65	0.64
Te	<LOQ	<LOQ	-	0.020	0.021
Cs	0.133	0.105	<LOQ	0.060	0.060
Ba	2.97	<LOQ	421	2.80	2.37
La	0.521	0.204	16.5	3.16	3.48
Ce	0.44	0.14	32.8	4.65	5.14
Pr	0.057	0.019	3.70	0.485	0.536
Nd	0.246	0.081	13.3	1.94	2.12
Sm	0.077	0.024	2.75	0.420	0.435
Eu	0.051	0.017	0.783	0.375	0.387
Gd	0.160	0.048	2.58	0.711	0.740
Tb	0.028	0.008	0.365	0.116	0.118
Dy	0.220	0.063	2.05	0.839	0.855
Ho	0.057	0.017	0.419	0.210	0.209
Er	0.193	0.057	1.33	0.661	0.661
Tm	0.029	0.007	0.200	0.092	0.091
Yb	0.187	0.056	1.41	0.600	0.604
Lu	0.030	0.009	0.212	0.095	0.094
Hf	<LOQ	<LOQ	3.18	0.03	0.03
Ta	<LOQ	<LOQ	0.54	0.01	0.01
W	1.01	0.283	-	0.601	0.591
Re	<LOQ	<LOQ	-	0.002	0.002
Pt	<LOQ	<LOQ	-	0.002	0.002
Au	<LOQ	<LOQ	-	0.014	0.009
Tl	0.010	0.009	-	0.013	0.015
Pb	0.73	0.48	4.74	6.00	7.14
Th	0.012	<LOQ	5.87	0.035	0.041
U	0.006	<LOQ	1.37	0.012	0.011